A NOVEL PWM SCHEME WITH TWO SWITCHING FREQUENCIES AND WIDER CARRIER TO IMPROVE THE THD IN VOLTAGE SOURCE CONVERTERS

by

Hussain Mohammad Bassi

B.S. in Electrical Engineering, King Abdulaziz University, 2004

M.S. in Electrical Engineering, Florida Institute of Technology, 2008

Submitted to the Graduate Faculty of

the Swanson School of Engineering in partial fulfillment

of the requirements for the degree of

Doctor of Philosophy

University of Pittsburgh

2013

UNIVERSITY OF PITTSBURGH

SWANSON SCHOOL OF ENGINEERING

This dissertation was presented

by

Hussain Mohammad Bassi

It was defended on

March 27, 2013

and approved by

Gregory Reed, PhD, Associate Professor,

Department of Electrical and Computer Engineering

George Kusic, PhD, Associate Professor,

Department of Electrical and Computer Engineering

William Stanchina, PhD, Professor,

Department of Electrical and Computer Engineering

Zhi-Hong Mao, PhD, Associate Professor,

Department of Electrical and Computer Engineering and Department of Bioengineering

Dr. Rajat Majumder, PhD,

Power Transmission at SIEMENS Energy Inc

Dissertation Director: Gregory Reed, PhD, Associate Professor,

Department of Electrical and Computer Engineering

A NOVEL PWM SCHEME WITH TWO SWITCHING FREQUENCIES AND WIDER CARRIER TO IMPROVE THE THD IN VOLTAGE SOURCE CONVERTERS

Hussain Mohammad Bassi, PhD

University of Pittsburgh, 2013

The integration of renewable energy resources presents a significant set of technical and infrastructure challenges to power grid operation and control. Besides, it has been proven that it is less harmful to the environment. Power electronics technology has the capability to mitigate the effects of the issues imposed on the power system by the rapid expansion of renewable energy development and increased penetration level at the utility scale. Although power electronics technology is considered a promising potential solution, power conversion efficiency in the rectifiers and inverters must be improved to optimize system performance.

A novel pulse width modulation technique is presented to improve the conversion efficiency. This method has two major concepts. First, widening the on-state of the converter's operation will increase the output fundamental component. Inverse sinusoidal pulse width modulation is one of the methods that can achieve this concept. Second, the rate of change in the information at the peak of the sinusoidal reference is relatively small. The modulation of this period has less significance in comparison to the rest of the reference cycle. Hence, a frequency modulation technique is applied to fulfill this task.

The novel development and utilization of these two techniques in combination will prove that; in comparison to the sinusoidal pulse width modulation, the fundamental output will increase substantially. Also, this new technique extensively suppresses the harmonic distortion of the converter operation. Furthermore, these results are attained by using lower switching frequency to produce lower switching losses and improves converter operation efficiency.

TABLE OF CONTENTS

LIST OF TABLES

LIST OF FIGURES

PREFACE

I would like to thank God for all his blessing. Also, I want to thank my parents for their prays for me everyday. My wife, Ghadeer, has been a great supporter for me and my children, Joanna and Mohammad, have been patient waiting for me while I was away working on my dissertation.

I would like to thank Dr. Gregory Reed for being my advisor. This dissertation would not be accomplished without his supervision. I am grateful to my PhD committee members, Dr. Kusic, Dr. Stanchina, Dr. Mao and Dr. Majumder, for their proactive feedback and suggestions. Special thanks go to Dr. Tom McDermott for his technical assistance. Their support helped me in learning the skills and approaches necessary for performing the scientific research.

I want to thank King Abdulaziz University for granting me a scholarship that allowed me to finish my PhD degree.

1.0 INTRODUCTION

1.1 MOTIVATION

Electric power infrastructure is being expanded and modernized on a global scale. As such, efficiency of power network operations must be taken into our consideration for future grid modernization effort. Improvements in energy efficiency overall, from the primary energy to the end-user, could save up to 20 % in the primary energy alone [2]. Power electronics, as applied in current and future power system infrastructure, needs to be more efficient. For example, conventional pulse-width modulation (PWM) voltage-source converters lack good power conversion efficiency when their instantaneous AC output is lower than the DC input. In addition, the converter output contains significant levels of high-frequency distortion [3].

Therefore, researchers have realized the importance of power electronics efficiency and have expended more effort in improving the converter technology. Designing new topologies [4–8] is one approach to increasing power electronics systems, especially the converters. In [4] a proposed new topology that contains two more switches and diodes as compared to a single-phase full-bridge converter, can raise the efficiency up to as much as 97.9%. This topology is suitable for transformerless grid-connected photovoltaic (PV) systems. In [5] the authors used a current source converter that utilizes voltage-clamping and soft-switching techniques on a proton exchange membrane (PEM) fuel cell to increase the efficiency to 95%, and reduced the total harmonic distortion (THD) to 1.41% for an RL load. The proposed current source converter in [6] consists of a clamped circuit, coupled circuit, and full-bridge resonant converter. This topology applied both soft-switching and low-switching stress techniques to increase the efficiency up to 97%, and depressed the THD below 2%. The efficiency of the new topology proposed in [7] increased to 96.5%. This increase was realized by using quasi time-sharing sinewave boost choppers with bypass diodes and a full-bridge inverter. The delta converter in [8] is connected in parallel with a conventional converter to compensate and improve the quality of the main converter output. This method reduced the output low-order harmonics and kept the THD below 20%.

Although these topologies improved the efficiency of the converters, they may not be practically applicable. In other words, it may be a challenge to upgrade or change the existing converters that are currently in operation using these techniques. Therefore, other researchers believe that the change in the PWM technique will improve converter efficiency in a more practical way. Increasing the fundamental component and reducing the THD are the focal points of several PWM techniques [9]. Researchers have created different PWM techniques [9–24] to accomplish these goals. In [10], the new PWM controls the switching in accordance with the line-to-line output instead of the phase output in three-phase systems. This technique improved the output by 15.47%, and reduced the switching operations to two-thirds of the conventional PWM method. The new modulation technique in [11] uses frequency modulation along with soft-switched PWM converter control. It includes the load current in the calculation of frequency, which results in efficiency improvement by 20%. Another frequency modulation technique [15, 16] improves the converter efficiency by utilizing a sinusoidal carrier. This carrier has a switching frequency that is a function of the slope of a trapezoidal reference wave. This technique reduced the switching to two-thirds of the conventional PWM and improved the THD of the single-phase inverter to 29%, if the switching frequency is 660 Hz. The radiated noise profile for this technique is preferred over the sinusoidal pulse width modulation (SPWM) technique [17]. The same previous frequency modulation technique is evaluated in [9, 12] except that the carrier wave is a triangular modulated with harmonic injected reference wave. The THD improvement in this technique is 47.3%. The heating losses on AC motor stators produced by using this technique is lower than the SPWM technique [13]. Also, the radiated acoustic noise spectrum is better than that of the SPWM [14]. Researchers [18] extended the improvement in the power conversion efficiency and suppressed the modulation during the reference wave peaks in the later frequency modulation technique. This results in noticeable advancement in THD, fundamental component, and the radiated noise. Another PWM technique [19–21] proposes a solution to the overmodulation issue. It utilizes the DC input by replacing the triangular wave with an inverted-sinusoidal carrier. This technique improved the fundamental output, and THD. Researchers improved the modulation schemes in multi-level converter as well. For example, the modulation techniques in [22–24] applied variable frequency on a five-level cascaded converter with harmonic injected reference wave to increase the fundamental output and decrease the THD.

Power conversion efficiency has captured the attention of many researchers. This efficiency is affected by several elements such as fundamental component, THD, switching losses, complexity of the implementation, and more. The focus of this dissertation is to provide a new solution to improve the conversion efficiency while taking all of these elements into consideration.

1.2 OBJECTIVES

The mechanism of force-commutated PWM technique is that the switches in the converters turn on and off based on comparing a modulation signal v_c, which is the desired AC output, with a triangular carrier wave v_Δ, which has the desired switching frequency. If the magnitude of v_c is greater than v_Δ, the upper switch in one leg of a voltage source converter will be in the on-state (ON) and the lower is in the off-state (OFF). Conversely, when the magnitude of v_c is less than the v_Δ, the upper switch in one leg is OFF and the lower is ON. When the modulation signal is sinusoidal the PWM technique will be referred to as sinusoidal PWM (SPWM). SPWM is the common modulation technique used in the industry today. Hence, it is the benchmark in all the comparisons being presented. The SPWM scheme reduces the filter's size by pushing the energy at the lower order harmonics to the higher harmonics. However, this improvement in the filtration is associated with a reduction in the fundamental component and increases the switching losses considerably.

A new modulation technique is presented herein - a Variable Frequency Inverse Sinusoidal Pulse Width Modulation (VFSPWM) scheme - which improves the fundamental component, lowers the total harmonics distortion, and reduces the switching losses.

The VFSPWM technique replaces the triangle carrier v_Δ in the SPWM technique with an inverse sinusoidal variable frequency carrier. The new carrier wave v_Δ switches at higher frequency when the slope of the modulation signal v_c is steep, i.e. $\left(\frac{dv_c}{dt}\right)$ is high. At the peak of v_c, the switching frequency of v_Δ is the lowest. The VFSPWM method is shown in Figure 1.1.

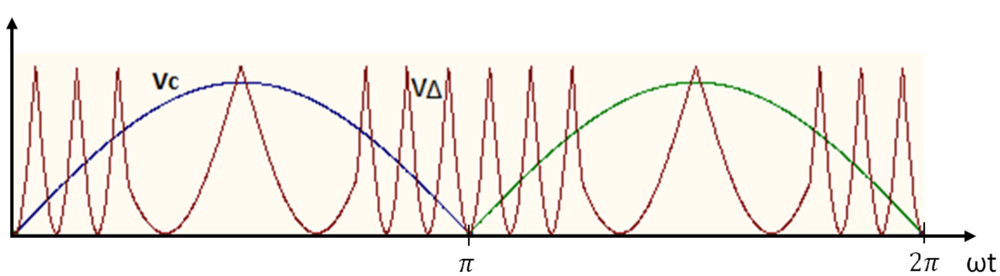

Figure 1.1: Variable Frequency Inverse Sinusoidal Pulse Width Modulation

VFSPWM increases the efficiency of the power conversions due to the better utilization of the DC source. Furthermore, the reduction in the total harmonics distortion results in providing smaller and more economical filter options. Since the switching at the peak of v_c is low, switching losses are reduced in the VFSPWM scheme, resulting in a significant reduction in the power conversion cost.

1.3 SIGNIFICANCE

The controversy of the use of DC versus AC for electric power transmission systems started in the 19th century, when Thomas Edison supported a DC approach, and Nikola Tesla and George Westinghouse advocated for the AC system. The electric utility industry settled on AC systems at that time. Since then, power demand and power infrastructure have grown dramatically. According to the 2011 World Energy Outlook (WEO) by the International Energy Agency (IEA) [25], global energy demand will increase by 40% by 2035, while global installed power generation will be doubled. Therefore, the integration of other energy resources, i.e. renewable energy, has become inevitable [2]. Renewable energy resources such as wind, solar, hydro, biomass, ocean and geothermal are environmentally preferable and are becoming more competitive in the marketplace. However, the interconnection of renewable energy resources into the grid introduces technological and infrastructure challenges. To name a few, voltage instability, voltage regulation, reactive power consumption, and sub-synchronous resonance are common issues related to renewable energy integration. In addition, this increase in generation will require new transmission and distribution system expansion and designs of more efficient technologies to improve the utilization of the existing infrastructure [26]. Power electronics technology is a practical solution for many of these issues.

Power electronics applications are widely applied in power systems, from generators to end-user. Power electronics are used in different areas in the the power system, i.e. distributed generation, power electronic loads, power quality solutions, and for transmission and distribution system applications [27]. For example, a change in wind speed causes the output voltage, magnitude, phase, and frequency of the variable-speed of wind generators to fluctuate [28]. Therefore, variable-speed drives using power electronics technology is applied to connect the wind farm to the grid [29]. In the transmission system, AC transmission lines have to deal with the generated or absorbed reactive power, increasing the line power transfer capability, and avoiding overvoltage issues, for example. This can be achieved by applying compensation systems such as Flexible AC Transmission System (FACTS), i.e., SVC, STATCOM using VSC, or even switched shunt capacitors and inductors [30].

Cycloconverters are another power electronics solution that controls the frequency. These controllers are an AC/AC frequency converter with the ability to control voltage [31]. High Voltage DC (HVDC) is one of the preferred power electronics transmission technologies applied to transmit power in DC form. HVDC systems show good standing in different applications such as long distance transmission and offshore wind farm interconnections. Force-commutated converter type HVDC, which is conventionally noted by VSC-HVDC, has several features that meet the grid code requirements (steady-state and dynamic) for wind farms. One of these requirements, for example, is that the wind farms must support the grid during faults instead of shutting down. This code is known as low voltage ride through (LVRT), which is achievable through the application of VSC-HVDC. Another requirement is the reactive power capability that is also a feature of the VSC-HVDC technology. The black-start capability in the VSC-HVDC to start the wind turbines is another reason to apply it for the wind farms interconnections [30, 32]. Battery storage systems with power electronics interfaces are a promising trend used for load leveling and mitigating fluctuations of unstable power outputs [28]. At the microgrid level, Electric Double Layer Capacitor (EDLC), a type of power electronics storage unit, has the ability to compensate voltage sags in uninterruptible power supply (UPS) systems for 20-60 seconds [28]. It is worth mentioning that power electronics technology is not limited to power system applications. For instance, electric and hybrid vehicles, which have low environmental pollution, are advancing rapidly in the past decade. This growth is partly due to continuous improvements in power electronics [33].

Overall, power electronics devices require advanced modulation techniques to ensure the proper operating states in power conversion. In order to be competitive in the power electronics industry, manufacturers have improved the converters performance, size, and cost, by using high-frequency modulation techniques [34]. This quest is advanced in this dissertation work, by providing a new high-frequency modulation technique, i.e., the VFSPWM.

2.0 LITERATURE REVIEW

Converters are called rectifiers when they convert the power from AC to DC, and called inverters given for DC to AC. There are two basic types of converter topologies: Current Source Converters (CSC) and Voltage Source Converters (VSC). The Current Source Converter (CSC) is the traditional converter that requires a large AC filter for harmonics elimination, in addition to the DC filters. It also needs reactive power supply to substitute for the consumed reactive power in the conversion in order to perform power factor correction. Converters usually consist of two three-phase converter bridges connected in series to form a 12-pulse unit, where each converter is a 6-pulse bridge. The switching valves are either transistors or thyristors. The switching between valves is known as commutation, and is the part of the power loss in the conversion. The switching loss results from inductive elements in the converter, e.g., the leakage inductance of the converter transformer makes the commutation not instantaneous. Or, put differently, it takes valve current a while to go to zero; hence, the product of the voltage and the current is not zero during the switching. In the traditional Current Source Converter (CSC) each valve is commutated only once per cycle. The meaning of this is that the commutation per valve occurs at the line frequency. Therefore, the converters that use this technology are called line-commutated converters (LCC). Although Current Source Converter (CSC) is the traditional converter, it is still extensively used because of its large power and voltage capabilities. [35–37]

Currents source converters have severely attracted the attention of the researchers in the last decades. For example, [37] proposed a new topology using GTO and PWM technique to improve the output voltage and current, mitigate the voltage spike caused by the change in the output current polarity. Furthermore, this topology provided excellent efficiency when the converter is connected to a motor as the only load. In addition, it enforce a noticeable reduction in the noise level. [38] provided a form of Hybrid-HVDC that combines the advantages of VSC and CSC in one transmission system. In the structure of the Hybrid-HVDC, the sending side is a CSC due to its high reliability and reasonable cost. Since VSC-HVDC has the ability to supply power into passive systems (no synchronous machines or with very small short circuit capacity), it has been used on the receiving side to supply remote isolated loads, for example. Additionally, it avoids increasing the short circuit capacity, because the AC fault current is controllable. While A VSC technology is utilized on the receiving side, where the converter is composed of an IGBT-based bridge, converter reactor (to link the VSC to the AC system), DC capacitor (to boost the DC voltage up and to reduce the effect of the impulse current when the bridge is off), and AC filters.

Voltage Source Converter (VSC) technology has some remarkable features such as its requirement for more economic AC filter for high order harmonics elimination. Furthermore, energy storage capacitors on the DC side control the power flow besides acting as DC harmonic filters. The switching occurs at high frequency, few kHz, using one of the pulse width modulation (PWM) techniques in order to get a smoother signal and eliminate low-order frequency harmonics. This switching technique is called self-commutated or forced-commutated because the converter forces the converter switches to turn ON and OFF frequently in one cycle. This technology has resolved several issues. For example, both active and reactive power can be controlled independently using one of the PWM techniques. In other words, it does not require a reactive power source as it can operate in any quadrant-i.e. rectifier/inverter operation with lagging/leading power factor. [30,35,39]

The performance evaluaiton of the VFSPWM is conducted on Inverters only. Inverters, in general, are static power converters that mainly produce, from a DC source, a controllable AC waveform output. The output waveforms of the force-commutated inverters are discrete due to the forced switching feature. Hence, the transition in the inverters is extremely quick at the expense of the wave quality (smoothness). Although, it is desired to produce a sinusoidal waveform, the discrete output behaves like one [31]. The generated AC voltage is composed of discrete values, high dv/dt, that constrains the load to be inductive to smooth the output. If the load is capacitive, an inductive filter is required between the VSI AC side and the load to suppress any generated current spikes. The switching frequency in the VSI configuration can be high compared to the line frequency, for instance, 1 kHz or below. For high-voltage applications, each switch group consists of two or more switching devices (IGBT, GCT, or GCT) connected in series to withstand the high power and voltage rating [40]. Single-phase VSI can be configured as a half-bridge or full-bridge VSI. The former consists of two non-simultaneous switch groups (to avoid short circuiting the DC link voltage source and the undefined switch states), and two large capacitors to set a neutral point N and the low-order current harmonics injected by the operation of the inverter. On the other hand, a full-bridge VSI has a similar structure to the half-bridge except that it has an additional leg to set the neutral point to the load, Figure 2.1. Also, the output AC voltage could only reach up to the DC link voltage value, unlike the half-bridge where it could reach up to one half the DC link voltage value. The three-phase VSI, discussed in section 7, is the inverter suitable for medium- to high-power applications. There are three legs in this inverter with eight valid switching states (each leg cannot operate simultaneously, the top and the bottom switches of any leg cannot both be on or off simultaneously). In order to ensure the selection of the valid states only, a controller that uses different modulation techniques is implemented to send the gating signal to the the switching devices. The most commonly used ones are carrier-based pulse width modulation. [31, 37, 40]

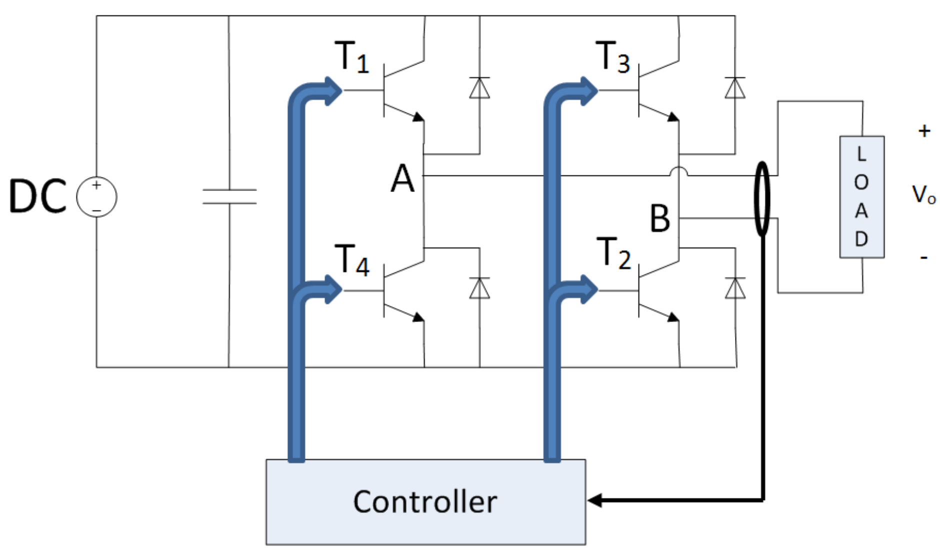

Figure 2.1: Full-Bridge Voltage Source Inverter

There are several types of PWM techniques. We found it convenient to follow this categorization: carrier-based PWM and programmed PWM. Although the programmed PWM technique shows better voltage output quality with lower switching losses, they require complicated control circuits and very advanced computers. Therefor, carrier-based PWM techniques are more viable [41]. The mechanism of the carrier-based PWM is that the switches turn on and off based on comparing a modulation signal v_c, which is the desired AC output, with a triangular carrier wave v_Δ, which has the desired switching frequency. If the magnitude of v_c is greater than v_Δ, the upper switch in one leg will be on and the lower is off. Conversely, when the magnitude of v_c is less than the v_Δ, the upper switch in one leg is off and the lower is on. When the modulation signal is sinusoidal the PWM technique will be referred to as sinusoidal PWM (SPWM). This modulation technique is used in the single-phase full-bridge VSI can be bipolar, where the output voltage is positive or negative due to the utilization of only one modulation wave just like the half-bridge VSI as shown in Figure 2.2. Unipolar SPWM utilizes two 180° out of phase modulation waves and one triangular carrier wave, as shown in Figure 2.3,to eliminate the odd multiples of the switching frequency and produces output voltage that has positive, negative, or zero value. The switching on each leg is controlled by one modulation wave to produce the AC output shown in Figure 2.3 [42, 43]. Unipolar SPWM can be applied by using an easier format that is composed of one modulation wave and unidirectional triangular carrier wave as shown in Figure 2.4 [44].

The case for the three-phase VSI is shown in Figure 2.5. This modulation technique is similar to the single-phase full-bridge VSI, except that it uses three 120° out of phase modulation waves (v_a, v_b, and v_c) instead of just one like the single-phase half-bridge/full-bridge bipolar. The SPWM technique has two main factors to control the fundamental-frequency component in the inverter output voltage: 1) amplitude-modulation ratio, and 2) frequency-modulation ratio. Amplitude-modulation ratio, also known as modulation index (m_a), is the ratio of the peak value of v_c to the peak value of v_Δ that controls the amplitude of the fundamental component of the AC output voltage. Usually this ratio is less than one; however, if m_a is greater than one, overmodulation will occur with higher fundamental AC output voltage (around 22% increase) but with more low-order harmonic components. If this ratio is too high, i.e., $m_a > 3.24$, it could lead to a square-wave modulation where the

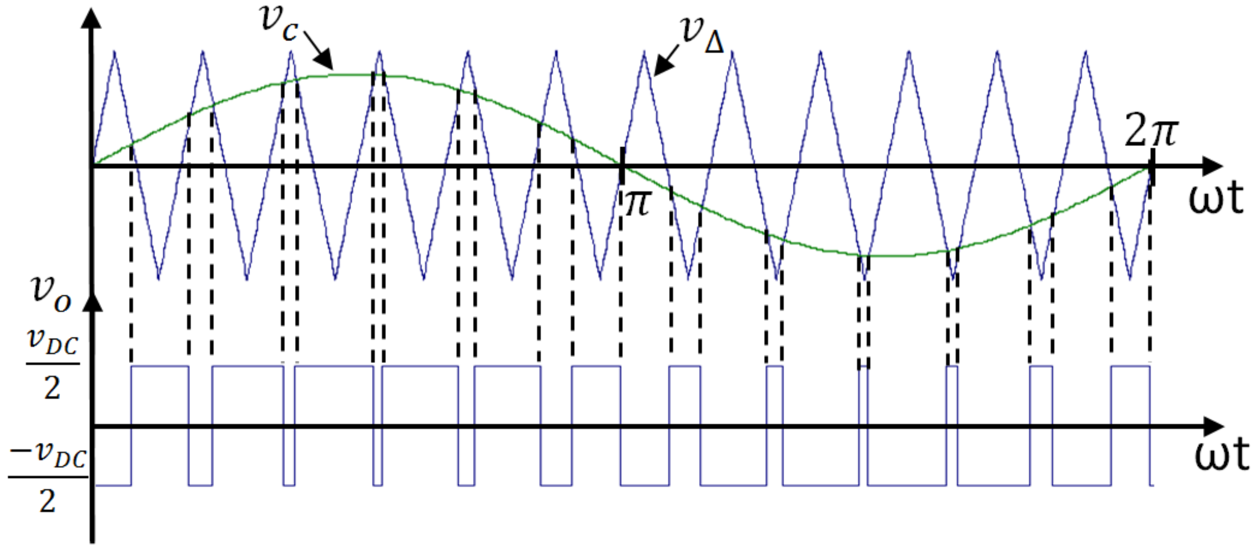

Figure 2.2: Bipolar SPWM VSI Carrie, Modulating signal and Output

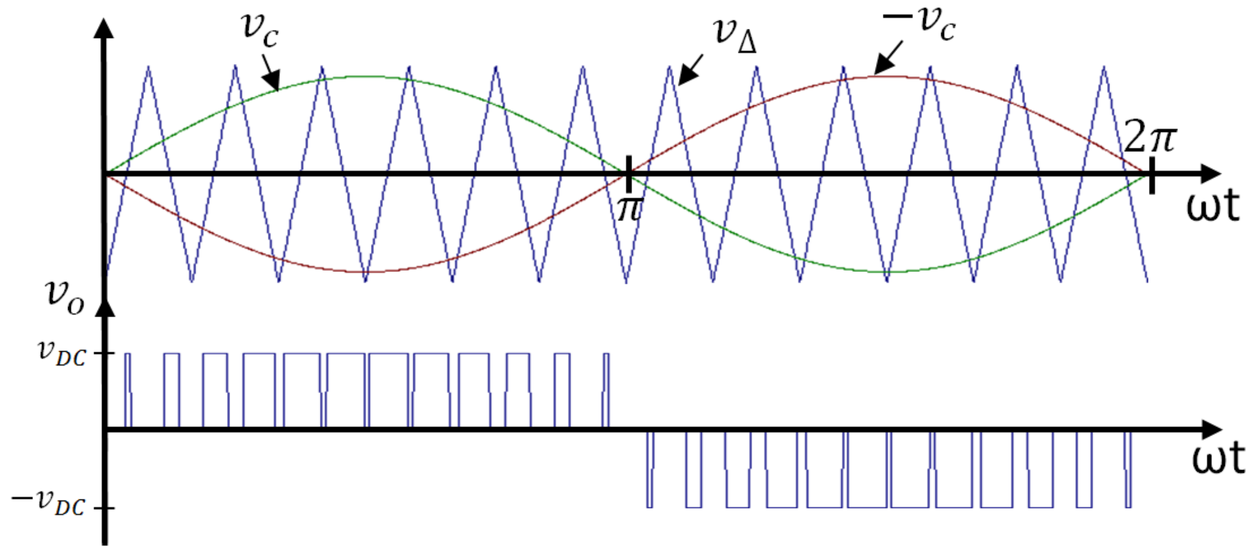

Figure 2.3: Unipolar SPWM VSI Carrie, Modulating signal and Output

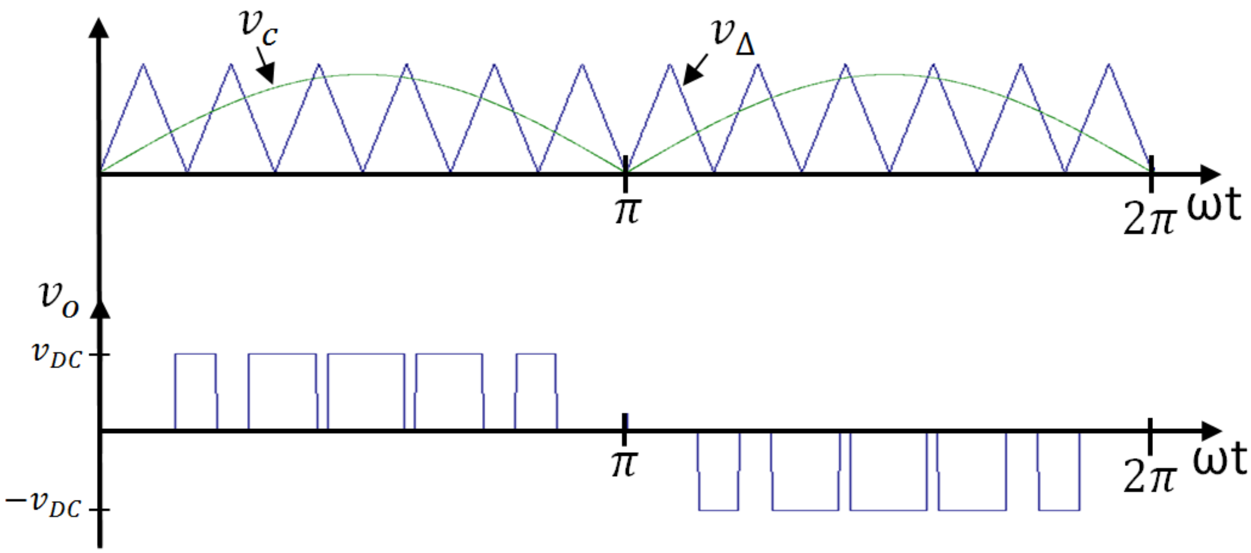

Figure 2.4: Unidirectional carrier SPWM

each leg in the inverter is ON for one-half cycle of the AC output period. The frequency-modulation ratio (m_f) is the ratio of the frequency of v_Δ to the frequency of v_c. The highest harmonics are having the orders equal to this ratio and its multiples. If m_f is an integer, which means the carrier wave is synchronized with the modulation wave, this scheme will be called synchronous PWM. Obviously, asynchronous PMW is another case where m$_f$ is not an integer. Hence, subharmonics or noncharacteristic harmonics (not a multiple of the fundamental frequency) will be presented in the output AC voltage. To use one carrier wave only and keep the SPWM features in the three-phase VSI, m_f should be an odd multiple of 3. [31,40]

A modified SPWM technique is presented in [45]. It has been observed that the data change rate at the peaks is low leading to the conclusion that the modulation in this period can be ignored. Therefore, the carrier wave has been modified to stop the switching for 60° centered at the peaks, Figure 2.6. This modulation technique improved the harmonics profile and lowered the switching losses. Besides, it increased the fundamental component [44].

Instead of using overmodulaiton technique to boost up the inverter output voltage, [46] proposed a technique known today as third harmonics injection that can be utilized and

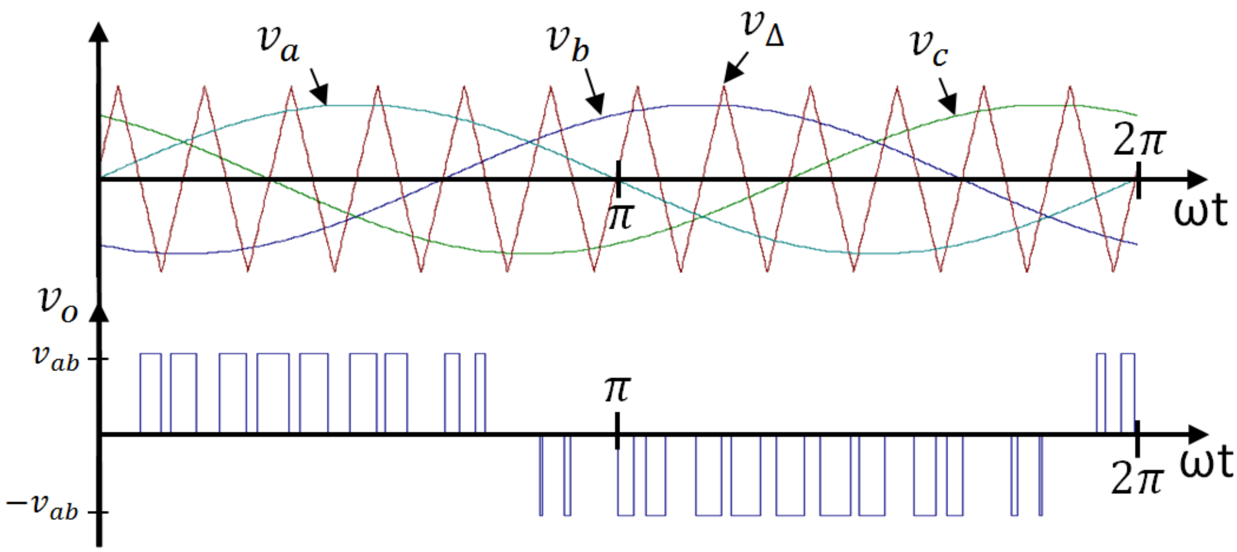

Figure 2.5: Three-phase SPWM VSI Carrie, Modulating signal and Output

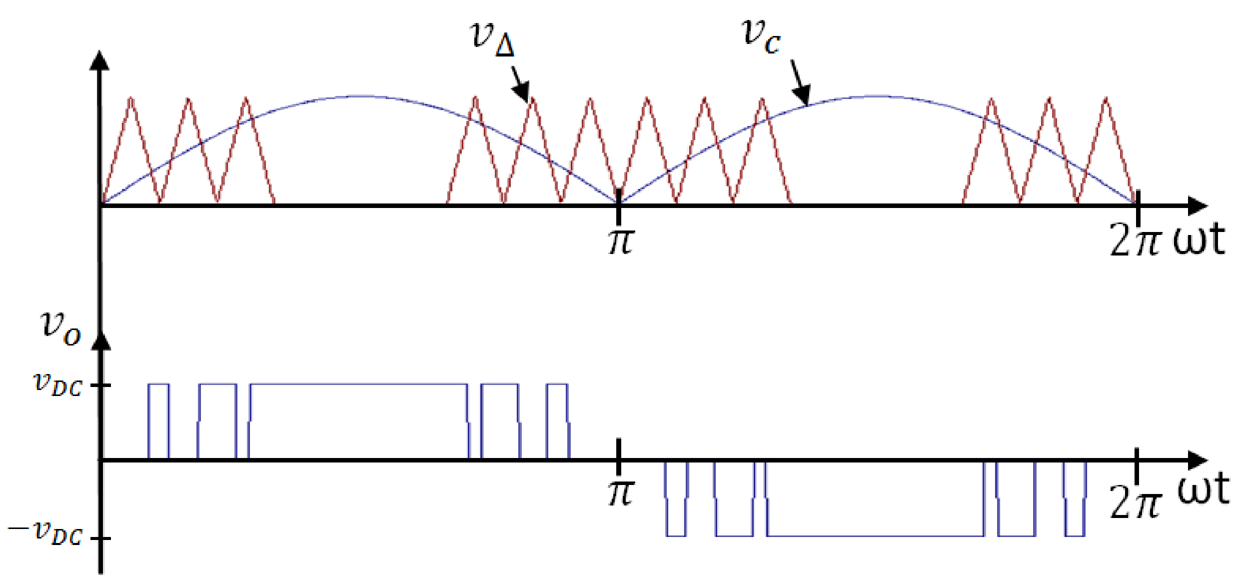

Figure 2.6: Modified Sinusoidal Pulse-Width Modulation

increase the output voltage up to $\frac{2}{\sqrt{3}}$ ($\approx$ 15.5%) while maintaining the harmonics profile similar to that of the SPWM technique. As the name is self-explanatory, this technique adds a third harmonic component , $\frac{1}{6}$ the fundamental component, to the sinusoidal modulation wave to result in a modulation wave that is flattened on the top (the peak value of v_c does not exceed the peak value of v_Δ). The third harmonic in the inverter output voltage (line-to-line) is canceled out by subtracting the line-neutral phases from each other [31, 40]. The single-phase harmonic injection pulse width modulation technique is shown in Figure 2.7.

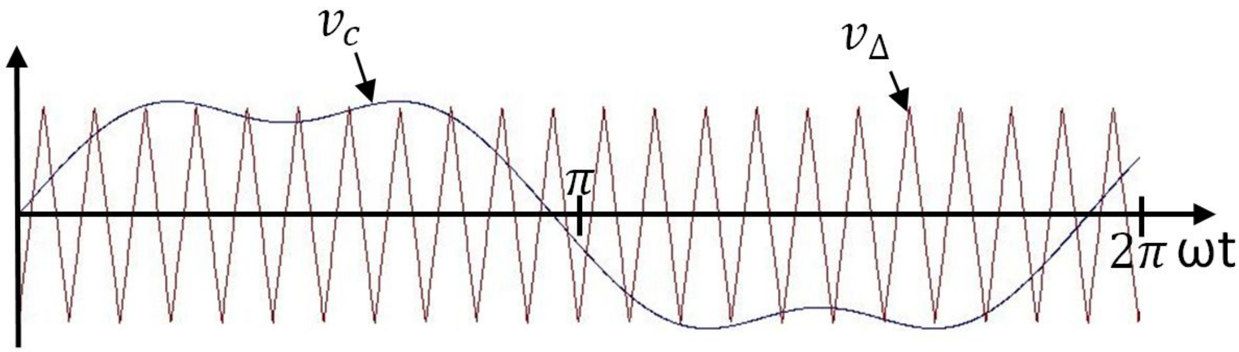

Figure 2.7: Harmonics Injection Pulse-Width Modulation

3.0 RESEARCH PLAN

The research plan is to compare the presented VFSPWM technique to the other commonly used methods ,e.g. , SPWM, Sawtooth PWM, and Modified PWM. The evaluation this novel PWM performance and its improvement in the power conversion efficiency is conducted in several steps. In this chapter we cover the analytic procedure used to develop this new PWM technique. Then we will present a model to simulate the modulation technique. A brief introductory of the the comparison measurements are then presented. A validation procedure for the model is used to ensure the reliability of this model used for the evaluation. Finally, a description of the model for the other PWM techniques is presented.

3.1 MODULATION SCHEMES

As mentioned before, the goal of the modulation techniques is to enforce the inverter to generate a waveform that has a fundamental component equal to a desired sinusoidal wave. The first attempt to achieve this objective was a simple form known as square-wave modulation. The switching frequency in this modulation technique is equal to the line frequency, i.e., 60Hz or 50Hz. In other words, the inverter output has a positive value for one half-cycle and negative for the other half-cycle. This method produces excellent fundamental component but has uncontrollable magnitude. Therefore, a single-pulse-width modulation is used to control the inverter fundamental output. This modulation technique has one pulse per cycle as well. The width of this pulse can be increased or decreased, thus controlling the magnitude of inverter output. Unfortunately, these two techniques contains high distortion.

One method to generate an output with reduced distortion is known as multiple-pulse-width modulation. This technique substituted the single pulse output by several pulses that has a total area equal to the area of the single pulse. The width of these pulses is constant. This process is achieved by comparing a DC wave (reference) with a triangular wave (carrier). When the reference wave is greater than the carrier wave, the gating pulse in on the ON state, closing the inverter switch. The inverter output is a function of the ration between the amplitude of the reference wave to the carrier wave, known as *modulation index* (m_a). The output, however, still has distortion that mandates the use of expensive filters.

Another modulation technique that uses the same principle of the high-frequency switching as in the multiple-pulses-width modulation is the Sinusoidal PWM (SPWM). The width of the gating signal is modulated according to the instantaneous amplitude of a sinusoidal wave (reference). This method reduces the inverter output distortion significantly and the relationship between the reference frequency and the carrier frequency is known as *frequency modulation* (m_f). When m_f is high, the harmonics distortion will be having the frequency of this m_f, thus reducing the filter size. However, the increase in the switching frequency leads to significant increase in the switching losses which affect the conversion efficiency. Besides, This technique may not reach the switching devices capacity and limit the inverter output to the $m_a = 1$.

The presented modulation technique utilizes the same concept of the pulse width of the square-wave technique. By way of explanation, it increases the width of the pulses while maintaining the same number of pulses per cycle to improve the utilization of the DC input. Hence, the fundamental component increases proportionally to the increase of the width of the pulse. In addition, this new modulation technique takes advantage of the high-frequency feature in the SPWM technique. The switching frequency is divided into high and low frequencies. The low-frequency period is 60° and starts when the data change in the reference wave is small. Therefore, the low-frequency should be centered at the peak of the reference wave. That is due to the fact that the use of high-frequency modulation in this period may cause more switching losses with unnoticeable increase in the inverter output accuracy. The high-frequency is placed in the beginning and ending for each cycle of a sine wave. This new modulation technique is shown in Figure 3.1.

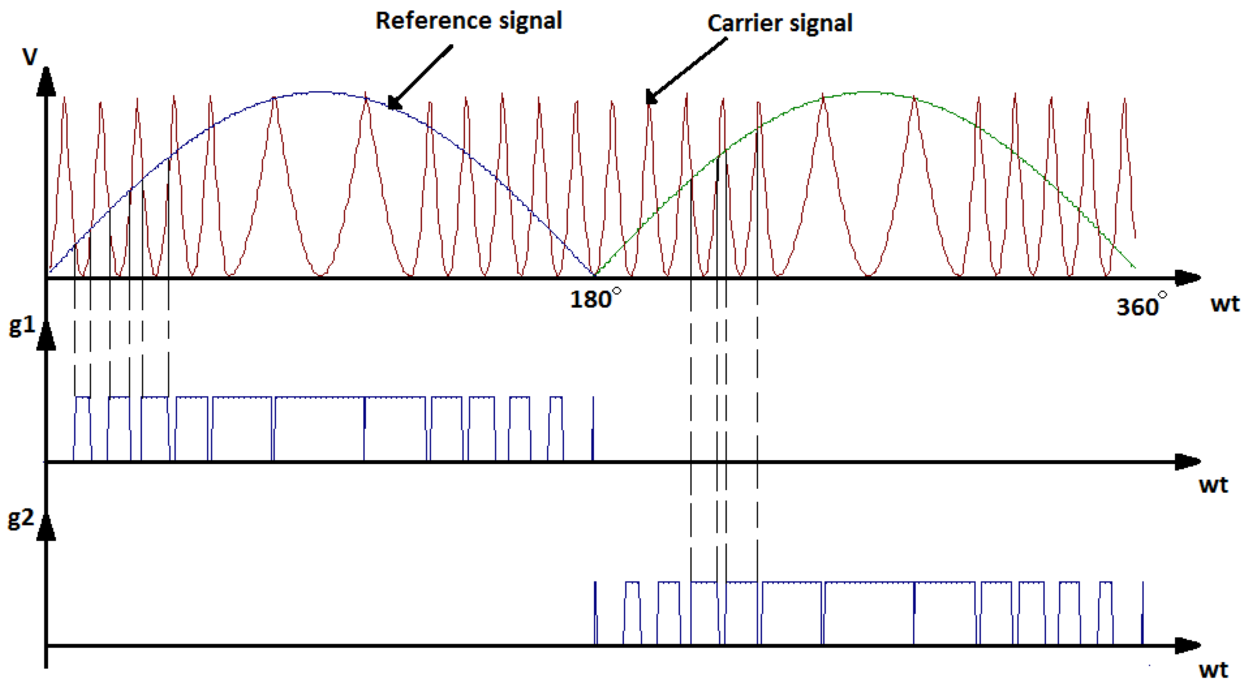

Figure 3.1: Variable-Frequency Inverse Sinusoidal Pulse Width Modulation

3.2 PSCAD MODEL

The model is divided into three primary components: Voltage-source inverter model, carrier generators, and gate pulse generators. The inverter model represents a single-phase full-bridge voltage-source inverter circuit, shown in Figure 3.2. It includes a DC source that represent a DC bus or link and 2 shunt capacitors on the DC side to set a neutral point N. Each capacitor has the same theoretical voltage $V_{DC}/2$.

1. **The inverter model** has two legs, leg A and leg B, where leg A produces the positive half of the inverter and leg B produces the negative half to synthesize an output that has $+V_{DC}$, 0, and $-V_{DC}$ values. There are two switches per leg, upper and lower, where each switch consists of a Insulated-Gate Bipolar Transistors (IGBT) and a *feedback diode*. This diode is required to keep the inductive load current flowing and prevent the voltage spikes during the switching commutations. The load has been chosen arbitrary to be

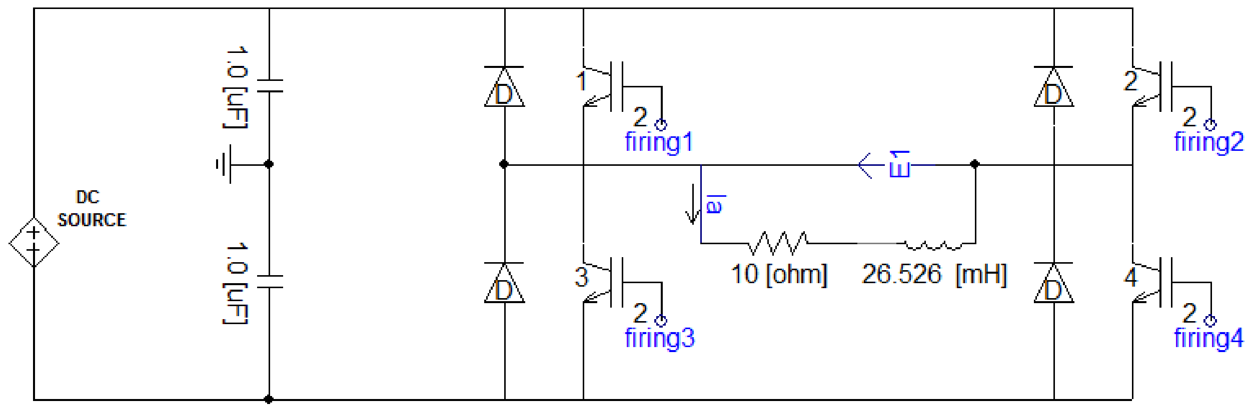

Figure 3.2: Full-Bridge Inverter

inductive for two reasons: first, the model has to reflect real industrial projects where the load in the power grid is primarily inductive. Second, If the the load is resistive, the change in the power factor will be unnoticeable. Besides, if the load is capacitive, extensive current spikes may be generated and inductive filters are likely to be required. The value of the inductance is equal to 26 mH.

2. **The carrier generator** is a model that creates a unidirectional variable-frequency inverse sinusoidal wave. This carrier produces the two switching frequencies, low and high. In Figure 3.3, $m_{f_{low}}$ is equal to 6 and $m_{f_{high}}$ is equal to 15. A frequency selector is connected to these two frequency sources to alternate between these two frequencies. The fundamental frequency is 60 Hz, which can be changed to any other frequency such as 50 Hz. In order to maintain the inverter output symmetry, the sinusoidal wave, that alternates between 6-15 times 60Hz, has been chosen to be a cosine function. This cosine signal is then run through an absolute function to change it into unidirectional wave. Then it flips vertically by multiplying the signal by -1. Finally, the unidirectional wave is shifted to the positive side by offsetting it by 1 to form the carrier shown in Figure 3.1.

3. **The gate pulse generator** provides a control signal to the inverter. It consists of two comparators and two logical inverters. The comparators in Figure 3.4 generate a pulse

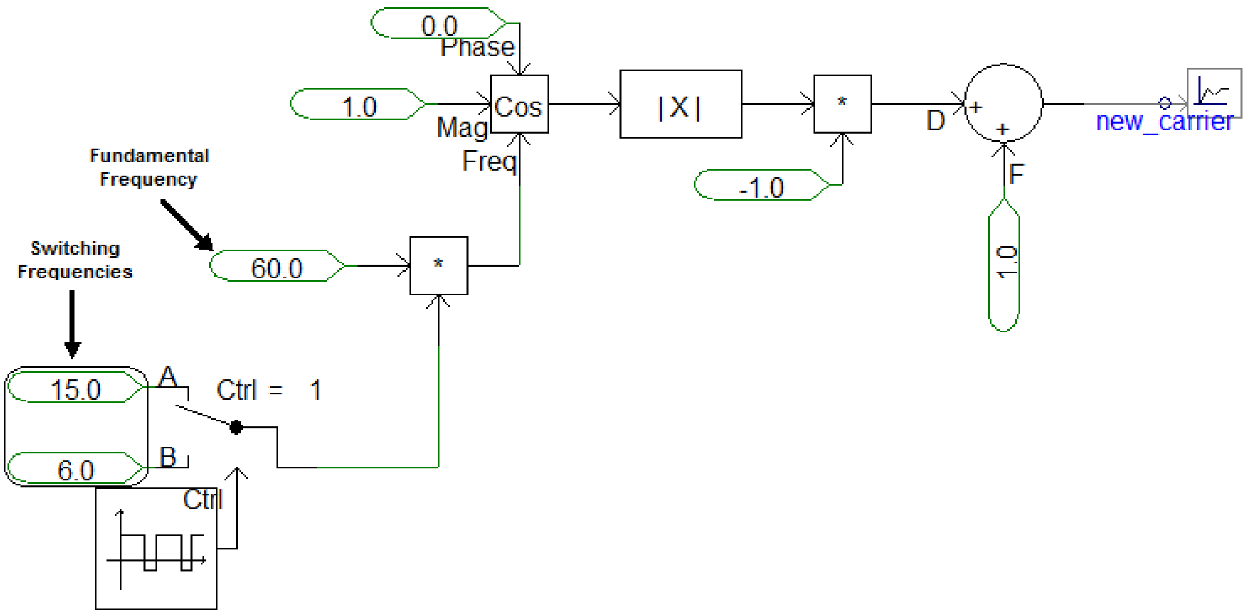

Figure 3.3: Carrier Generator

when the modulated carrier is less than a generated sinusoidal wave (reference). And generate a zero when the carrier is over the reference wave. Each carrier generator is designated to one leg in the full-bridge inverter and one sinusoidal reference wave. The two sinusoidal reference are 180° out of phase. Since the upper and lower switches per leg should be in the opposite states, the output of the comparator gets the opposite value by using the logical inverter. The generated pulses then control the switches in the full-bridge inverter to produce an output that has an RMS value close to the reference wave. The gating signal is shown in Figure 3.1.

3.3 PERFORMANCE PARAMETERS

To evaluate and validate the new PWM technique and the model, a set of quality measurements needs to be defined. *Weighted Total Harmonic Distortion* (WTHD) and the

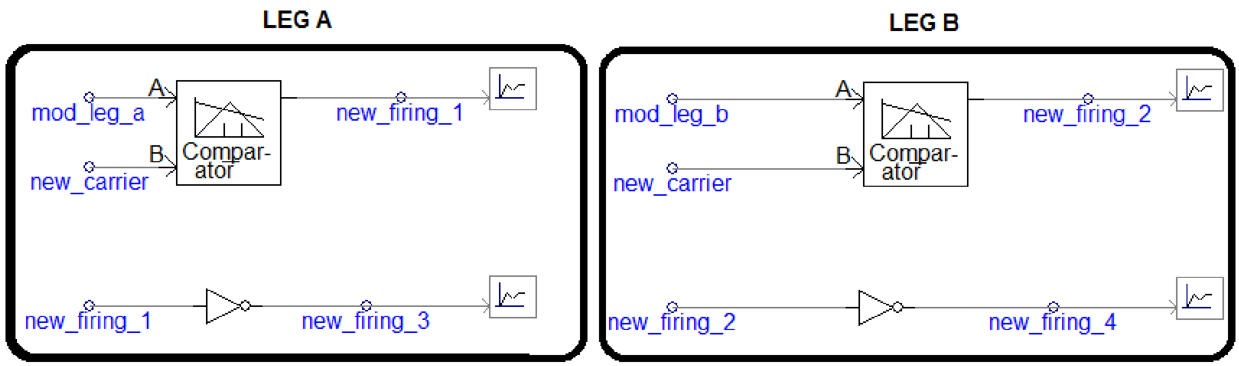

Figure 3.4: Gate Pulse Generator

fundamental component (V_1 or I_1) are the two widely used parameters for comparisons. In order to understand the concepts of the WTHD and the fundamental components, we need to explain briefly the Fourier series analysis.

3.3.1 Fourier series analysis

Jean-Baptiste Joseph Fourier invented a method to describe periodic waves with trigonometric functions that have multiple frequency of the fundamental period T. This method is known as *Fourier Series*. The periodic function is represented as

$$f(t) = a_v + \sum_{n=1}^{\infty} a_n cos\ n\omega_\circ t + b_n sin\ n\omega_\circ t \tag{3.1}$$

where $a_v,\ a_n,\ and\ b_n$ are known as *Fourier coefficients*. And $\omega_\circ$ is the *fundamental frequency* and its multiples are the *harmonic frequencies*. The Fourier coefficients can be calculated as follows:

$$a_v = \frac{1}{T}\int_{t_\circ}^{t_\circ+T} f(t)\, dt \tag{3.2}$$

$$a_n = \frac{2}{T}\int_{t_\circ}^{t_\circ+T} f(t) cos\ (n\omega_\circ t)\, dt \tag{3.3}$$

$$b_n = \frac{2}{T}\int_{t_\circ}^{t_\circ+T} f(t) sin\ (n\omega_\circ t)\, dt \tag{3.4}$$

Forming the signal symmetrically is beneficial in a sense that the calculation of the harmonics is convenient. For example, even-function symmetry has this form

$$f(t) = f(-t) \tag{3.5}$$

This form reduces the tedious calculation of the coefficients and expresses them as follows

$$\begin{aligned} a_v &= \frac{2}{T}\int_0^{T/2} f(t)\,dt && (3.6)\\ a_n &= \frac{4}{T}\int_0^{T/2} f(t)\ cos\ (n\omega_\circ t)\,dt && (3.7)\\ b_n &= 0,\ \text{for all } n. && (3.8) \end{aligned}$$

The function is odd when it has this form

$$f(t) = -f(-t) \tag{3.9}$$

In this case, the coefficient calculation is simpler and is expressed as follows

$$\begin{aligned} a_v &= 0 && (3.10)\\ a_n &= 0,\ \text{for all } n. && (3.11)\\ b_n &= \frac{4}{T}\int_0^{T/2} f(t)\ sin\ (n\omega_\circ t)\,dt && (3.12) \end{aligned}$$

When the wave is repeated in an opposite sign after one-half cycle, it will be called half-wave symmetry. It gains more simplification and has the following mathematical expression

$$f(t) = -f(-t - T/2) \tag{3.13}$$

This form can be even, odd or neither. The coefficients will have to following forms

$$\begin{aligned} a_v &= 0 && (3.14)\\ a_n &= \frac{4}{T}\int_0^{T/2} f(t)\ cos\ (n\omega_\circ t)\,dt,\ \text{for } k \text{ odd.} && (3.15)\\ a_n &= 0,\ \text{for } k \text{ even.} && (3.16)\\ b_n &= \frac{4}{T}\int_0^{T/2} f(t)\ sin\ (n\omega_\circ t)\,dt \text{ for } k \text{ odd.} && (3.17)\\ b_n &= 0,\ \text{for } k \text{ even.} && (3.18) \end{aligned}$$

The calculation of the coefficient can have the simplest form if the function is quarter-wave symmetry. When a function is half-wave and has a symmetry at the positive or negative midpoint, this function will be know as quarter-wave symmetry. This symmetry can be even or odd. If the function is even, the coefficient will be calculated this way

$$a_v = 0 \tag{3.19}$$

$$a_n = \frac{8}{T}\int_0^{T/4} f(t)\; cos\;(n\omega_\circ t)\, dt,\;\text{ for } k \text{ odd.} \tag{3.20}$$

$$a_n = 0,\;\text{ for } k \text{ even.} \tag{3.21}$$

$$b_n = 0,\;\text{ for all } k. \tag{3.22}$$

When the function is odd, the coefficients is similar to the ones in Equations (3.19)-(3.22) except they have the following modifications

$$a_v = 0 \tag{3.23}$$

$$a_n = 0,\;\text{ for all } k. \tag{3.24}$$

$$b_n = \frac{8}{T}\int_0^{T/4} f(t)\; sin\;(n\omega_\circ t)\, dt,\;\text{ for } k \text{ odd.} \tag{3.25}$$

$$b_n = 0,\;\text{ for } k \text{ even.} \tag{3.26}$$

3.3.2 Fundamental component and WTHD

As mentioned previously in section (3.3.1), A periodic function can be expressed in this form

$$\begin{aligned} f(t) &= a_v + \sum_{n=1}^{\infty} a_n cos\; n\omega_\circ t + b_n sin\; n\omega_\circ t \\ &= a_v \\ &+ a_1 cos\; \omega_\circ t + a_2 cos\; 2\omega_\circ t + a_3 cos\; 3\omega_\circ t + ... \\ &+ b_1 sin\; \omega_\circ t + b_2 sin\; 2\omega_\circ t + b_3 sin\; 3\omega_\circ t + ... \end{aligned} \tag{3.27}$$

Since the inverter output has quarter-wave symmetry, the fundamental components (V_1 or I_1) can be simply expressed by calculating the first term in either equation (3.20) for the even function or equation (3.25) for the odd function.

The total harmonic distortion (THD) is the ratio between the fundamental component and the rest of the harmonics. In other word, this factor depicts how close the inverter output to desired reference wave. The THD for half-wave symmetric function can be calculated using the following expression

$$THD = \frac{1}{V_1}\sqrt{\sum_{n=3,5,7,\cdots}^{\infty} V_n^2} \tag{3.28}$$

Or

$$THD = \sqrt{\left(\frac{V_{rms}}{V_{1,rms}}\right)^2 - 1} \tag{3.29}$$

The weighted total harmonic distortion (WTHD) is similar to the THD except that it assigns weights to the harmonics. The low-order harmonics get more weight than the high-order harmonics. This is beneficial in a sense that this parameters indicates who much the curve depends on the low-order harmonics. WTHD can be expressed as following

$$WTHD = \frac{1}{V_1}\sqrt{\sum_{n=3,5,7,\cdots}^{\infty} \left(\frac{V_n}{n}\right)^2} \tag{3.30}$$

These measurements can be calculated using the build-in functions in PSCAD. For example, the on-line Frequency Scanner (FFT) determines the harmonics coefficient, including the fundamental component, of the input signal. After specifying the base frequency, the number of phases and the number of harmonics needed, it calculates the harmonic magnitude, phase and the DC offset as well. Harmonic Distortion Calculator is another built-in function that can finds the WTHD. This can be seen in Figure 3.5. On the other hands, PSPICE using OrCAD calculates the WTHD of a signal by toggling the FFT function in the PSPICE Schematics.

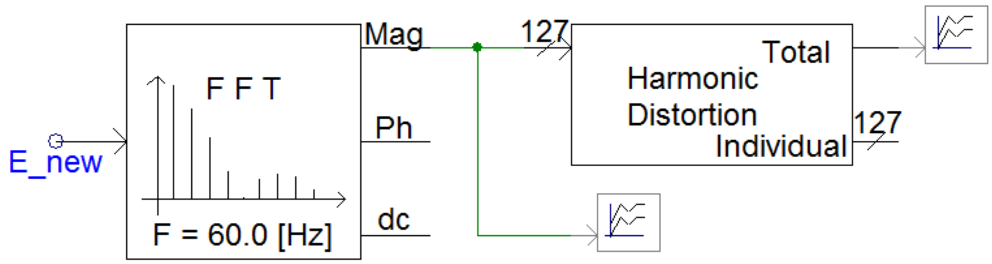

Figure 3.5: PSCAD FFT and THD components

3.4 MODEL VALIDATION

To ensure the validity of the PSCAD model, a mathematical representation has been conducted. Besides, PSPICE using OrCAD has been utilized to support the PSCAD model by matching the inverter output fundamental component and the WTHD. This validation examines two modulation methods, SPWM and VFSPWM. We added the SPWM to the validation process because this modulation technique has been studied extensively by several researchers. Therefore, it supported the validation of the VFSPWM. Besides, SPWM is the benchmark method.

3.4.1 Mathematical Model

In this section we examine the VFSPWM technique mathematically. As we mentioned in section 3.3, the fundamental components and the WTHD are calculated using the Fourier coefficients. The quarter-wave symmetry property in the inverter output makes equation (3.25) the focal point. Since the output of the inverter has several pulses with different width as shown previously in Figure 3.1, it is required to calculate the Fourier coefficients for each pulse. These coefficients are then added together to provide the harmonics coefficient of the inverter output. This coefficient can be expressed as follows

$$
\begin{aligned}
b_n &= \frac{2}{T}V_{dc}\left[\int_0^{\alpha_1} sin\ n\omega t\, d(\omega t) + \int_{\alpha_1}^{\alpha_2} sin\ n\omega t\, d(\omega t) + \cdots \right. && (3.31)\\
&+ \left. \int_{\alpha_m}^{\pi/2} sin\ n\omega t\, d(\omega t)\right] \\
&= \frac{2V_{dc}}{T}\left(\frac{1 - cos\ n\alpha_1 + cos\ n\alpha_2 + \cdots + cos\ n\alpha_m}{n}\right) && (3.32)\\
&= \frac{2V_{dc}}{nT}\left[1 + \sum_{k=1}^{m} cos(n\alpha_k)\right] && (3.33)
\end{aligned}
$$

Since $T = \dfrac{\pi}{2}$,then

$$
b_n = \frac{4V_{dc}}{n\pi}\left[1 + \sum_{k=1}^{m}(-1)^k\ cos(n\alpha_k)\right] \text{ for n=1,3,5,...} \qquad (3.34)
$$

where $\alpha_1 < \alpha_2 < \alpha_3 < \cdots < \frac{\pi}{2}$. And to find the RMS value, simply divide b_n by $\sqrt{2}$. We used MATLAB to calculate the fundamental component and the WTHD for the SPWM and VFSPWM.

3.4.1.1 Sinusoidal Pulse Width Modulation The analysis of the SPWM has been done already by different researchers. Therefore, we are built a MATLAB code that represents the sinusoidal pulse-width modulation technique mathematically. This MATLAB code has several parts. First, the input parameters are the arbitrary chosen initial switching angles. Then we set the other initial parameters such as the modulation index (m_a) and the modulation ratio (m_f). If the input parameters are in seconds, they need to be converted into radian unit.

```
function s = spwm(x)

Ma=1;

Mf=24;

x=x*120*pi;
```

The next part is for finding the switching angles that form the chain of the gating pulses. Finding the angles is achieved by using a built-in MATLAB function called *fzeros*. This function finds the zeros of the the difference between two parts. The first part is the triangular carrier and the second part is the sinusoidal reference wave. The triangular wave can be expressed by taking the trigonometrical inverse of the a cosine function that has a frequency equal to m_f. This term is normalized by dividing it by π . These zeros are the angles when the reference wave and the triangular wave are equal. If the gating signal starts with the OFF state, then we need to add another *fzeros* equation with an initial value equals to 0. The number of angles here is 4.

```
s = [ fzero( @(x)(acos(cos(Mf*x))/pi)-Ma*sin(x),x(1),[0 pi/2]);
      fzero( @(x)(acos(cos(Mf*x))/pi)-Ma*sin(x),x(2),[0 pi/2]);
      fzero( @(x)(acos(cos(Mf*x))/pi)-Ma*sin(x),x(3),[0 pi/2]);
      fzero( @(x)(acos(cos(Mf*x))/pi)-Ma*sin(x),x(4),[0 pi/2])];
```

After we find the angles ($\alpha_1 \cdots \alpha_k$), we calculate $b_1, b_3, \cdots, b_n$ using equation (3.34). This example calculates the harmonics up to the 63^{rd} order. Then we use the these Fourier coefficient to calculate the WTHD using equation (3.28) or (3.29).

```
H=0;
for n=3:2:63
H(n)=abs((400/(n*pi))* (1-cos(n*s(1))+cos(n*s(2))-cos(n*s(3))+cos(n*s(4))));
end
V1=(400/(pi))* (1-cos(s(1))+cos(s(2))-cos(s(3))+cos(s(4)))
THD=100*sqrt(sum(H.^2))/V1
```

3.4.1.2 VFSPWM

- Output Voltage Calculation

  To calculate the inverter RMS output voltage of the mth pulse, let us assuming each pulse width is δ, Figure 3.6:

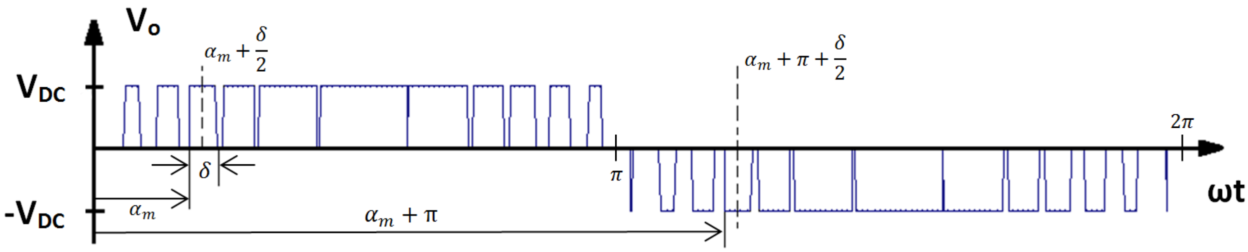

Figure 3.6: Inverter Output using VFSPWM Technique

$$\begin{aligned} V_{LL,m} &= \left[\frac{2}{2\pi} \int_{\alpha_m}^{\alpha_m+\delta_m} V_{DC}^2 \; d(\omega t) \right]^{\frac{1}{2}} \\ &= \left[\frac{V_{DC}^2}{\pi} \left(\alpha_m + \delta_m - \alpha_m \right) \right]^{\frac{1}{2}} \\ &= \left[\frac{V_{DC}^2}{\pi} \; \delta_m \right]^{\frac{1}{2}} \end{aligned} \tag{3.35}$$

And for all the pulses, the inverter RMS output voltage will be:

$$\begin{aligned} V_{LL} &= \left[\frac{V_{DC}^2}{\pi} \sum_{m=1}^{2p} \delta_m \right]^{\frac{1}{2}} \; , p = mf - 1 \\ &= V_{DC} \left[\sum_{m=1}^{2p} \frac{\delta_m}{\pi} \right]^{\frac{1}{2}} \end{aligned} \tag{3.36}$$

The instantaneous output voltage should have the this form:

$$v_o = \sum_{n=1,3,5,\ldots}^{\infty} B_n sin \left(n\omega t \right) \tag{3.37}$$

As shown in Figure 3.6, there is a negative pulse that has a width, α_m, equal to a positive pulse that is displaced by π and start at δ_m. With this structure, this wave has the even-symmetry property. Therefore, the Fourier Coefficient A_n is equal to 0 and B_n is calculated for odd harmonics only. We are calculating the coefficient B_n for each pair of pulses and we denoted it b_n. Eventually we are adding these b_n coefficient to find the final B_n value. This coefficient can be derived as follows:

$$
\begin{aligned}
b_n &= \frac{2}{\pi}\Big[\int_{\alpha+\frac{\delta_m}{2}}^{\alpha+\delta_m} V_{DC}\, sin(n\omega t)\, d(\omega t) - \Big[\int_{\pi+\alpha}^{\pi+\alpha+\frac{\delta_m}{2}} V_{DC}\, sin(n\omega t)\, d(\omega t)\Big] \\
&= \frac{2\,V_{DC}}{\pi}\Big[\frac{-cos\,(n(\alpha_m+\delta_m))}{n} + \frac{cos\,(n(\alpha_m+\frac{\delta_m}{2}))}{n} \\
&+ \frac{cos\,(n(\pi+\alpha_m+\frac{\delta_m}{2}))}{n} - \frac{cos\,(n(\pi+\alpha_m))}{n}\Big] \qquad (3.38)
\end{aligned}
$$

Let us assume that:

$$
\begin{gathered}
X_1 = n(\alpha_m + \frac{\delta_m}{2}) \text{ and } Y_1 = n(\alpha_m+\delta_m) \\
X_2 = n(\pi+\alpha_m + \frac{\delta_m}{2}) \text{ and } Y_2 = n(\pi+\alpha_m)
\end{gathered}
$$

We can say that:

$$
\begin{aligned}
\frac{X_1+Y_1}{2} &= \frac{1}{2}\big[n(\alpha_m+\frac{\delta_m}{2}) + n(\alpha_m+\delta_m)\big] \\
&= \frac{1}{2}\big[n\big(2\alpha_m+\frac{3\delta_m}{2}\big)\big] = n\big(\alpha_m+\frac{3}{4}\,\delta_m\big) \qquad (3.39) \\
\frac{Y_1-X_1}{2} &= \frac{1}{2}\big[n(\alpha_m+\delta_m) - n\big(\alpha_m+\frac{\delta_m}{2}\big)\big] = n\frac{\delta_m}{4} \qquad (3.40) \\
\frac{X_2+Y_2}{2} &= \frac{1}{2}\big[n(\pi+\alpha_m+\frac{\delta_m}{2}) + n(\pi+\alpha_m)\big] \\
&= \frac{1}{2}\big[n\big(2\pi+2\alpha_m+\frac{\delta_m}{2}\big)\big] = n\big(\pi+\alpha_m+\frac{\delta_m}{4}\big) \qquad (3.41) \\
\frac{Y_2-X_2}{2} &= \frac{1}{2}\big[n(\pi+\alpha_m) - n\big(\pi+\alpha_m+\frac{\delta_m}{2}\big)\big] = -n\frac{\delta_m}{4} \qquad (3.42)
\end{aligned}
$$

Let us substitute equations (3.39)-(3.42) in this geometric function:

$$
cos(X) - cos(Y) = 2sin\Big(\frac{X+Y}{2}\Big)\; sin\Big(\frac{Y-X}{2}\Big)
$$

We are getting the following expressions:

$$
\begin{aligned}
cos(X_1) - cos(Y_1) &= 2sin\big(n\big(\alpha_m+\frac{3}{4}\,\delta_m\big)\big)\; sin\big(n\frac{\delta_m}{4}\big) \qquad (3.43) \\
cos(X_2) - cos(Y_2) &= 2sin\big(n\big(\pi+\alpha_m+\frac{\delta_m}{4}\big)\big)\; sin\big(-n\frac{\delta_m}{4}\big) \\
&= -2sin\big(n\big(\pi+\alpha_m+\frac{\delta_m}{4}\big)\big)\; sin\big(n\frac{\delta_m}{4}\big) \qquad (3.44)
\end{aligned}
$$

Because n is odd, n=1,3,5,...

Substituting equations (3.43) and (3.44) in (3.38) will result the following:

$$b_n = \frac{4V_{DC}}{n\pi}\ sin\big(n\frac{\delta_m}{4}\big)\left[sin\bigg(n\big(\alpha_m + \frac{3}{4}\ \delta_m\big)\bigg) - sin\bigg(n\big(\pi + \alpha_m + \frac{\delta_m}{4}\big)\bigg)\right] \tag{3.45}$$

The Fourier Coefficient B_n for all the pulses is:

$$B_n = \sum_{m=1}^{2p} \frac{4V_{DC}}{n\pi}\ sin\big(n\frac{\delta_m}{4}\big)\left[sin\bigg(n\big(\alpha_m + \frac{3}{4}\ \delta_m\big)\bigg) - sin\bigg(n\big(\pi + \alpha_m + \frac{\delta_m}{4}\big)\bigg)\right] \tag{3.46}$$

The final v_o expression can be found by substituting equation (3.46) in (3.37) to get:

$$v_o = \sum_{n=1,3,5,\ldots}^{\infty} \sum_{m=1}^{2p} \frac{4V_{DC}}{n\pi}\ sin\big(n\frac{\delta_m}{4}\big)\left[sin\bigg(n\big(\alpha_m + \frac{3}{4}\ \delta_m\big)\bigg) - sin\bigg(n\big(\pi + \alpha_m + \frac{\delta_m}{4}\big)\bigg)\right] sin(n\omega t) \tag{3.47}$$

- The Number of Angels

  To find the number of the intersections between the carrier and the reference waves, the number of α's, each half-cycle is divided into three areas as shown in Figure 3.7. Each area has a period of 60°. In each area the number of α's can be found using the following expression:

$$number\ of\ \alpha_{(Area\,i)} = \frac{2}{3}(m_f - 1) + X_{i-1} \tag{3.48}$$

Where m_f is the modulation ration. X is the residue of rounding the value of α from the previous area, X=0 in the first region. Let us take Figure 3.7 as an example where the modulation ratios are 8 and 2:

Number of α's in area 1:

$$\frac{2}{3}\,(8-1) = 4.666 \quad rounded\ to\ 5\ \alpha's \tag{3.49}$$

X_1 is equal to -0.333

Number of α's in area 2:

$$\frac{2}{3}\,(2-1) + (-0.333) = 0.333 \quad rounded\ to\ 0\ \alpha's \tag{3.50}$$

X_2 is equal to 0.3333

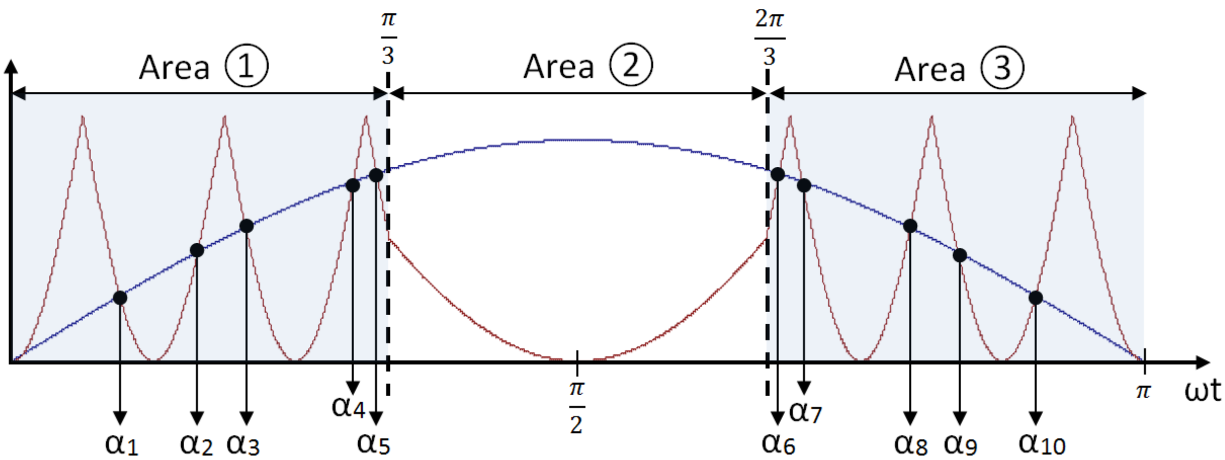

Figure 3.7: VFSPWM $_{8-2}$ Angels

Number of α's in area 3:

$$\frac{2}{3}(8-1) + (0.333) = 5\ \alpha's \tag{3.51}$$

The total number of α's is 10.

The calculation of α's should follow these rules:

1. When $m_{f_{high}}$ is not triplen, the last α in area 1 must shift to area 2.
2. When $m_{f_{high}}$ is not triplen, the first α in area 3 must shift to area 2.

- Finding the Angles

  It is better to analyze one pulse first and calculate the angles, α's, in it and then generalize this calculation for the rest of the pulses in a cycle. Each pulse is divided into two areas: even and odd. The even α's, α_2, α_4,α_6 and more, are in the even region in each pulse. Similarly, α_1, α_3,α_5 and more are in the odd region of each pulse. Figure 3.8a shows the carrier and the reference waves between α_7 and α_8 in Figure 3.7 that forms a single pulse. The calculation of the angles in the mth pulse follows this procedure:

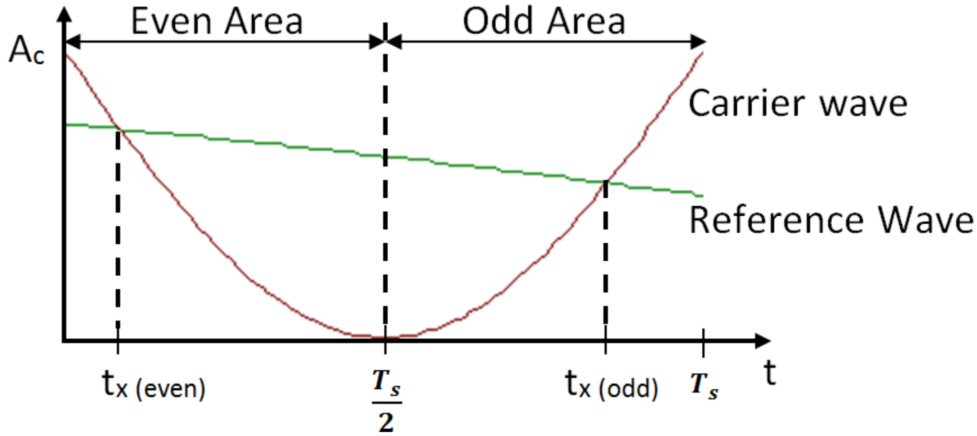

(a) VFSPWM of m $_{th}$ Pulse

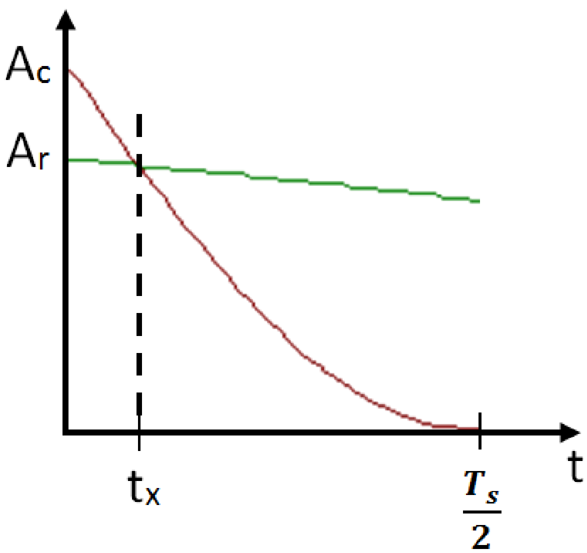

(b) VFSPWM Even α

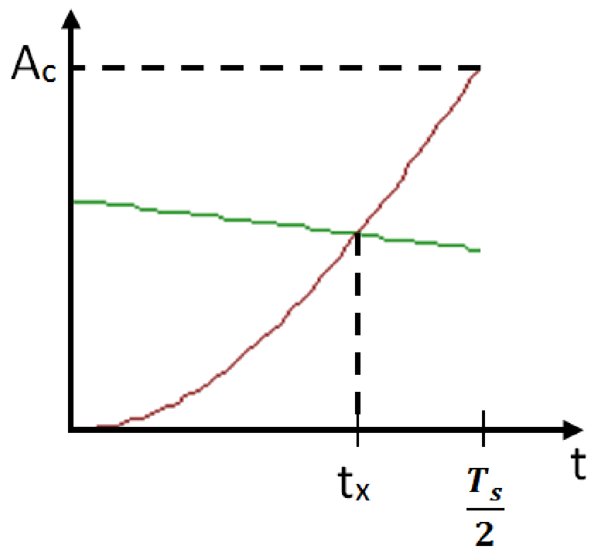

(c) VFSPWM Odd α

Figure 3.8: VFSPWM Alpha's Calculation

1. Even Area:

   As shown in Figure 3.8b, the carrier function is

$$A_c(1 - |cos(m_f\omega t)|) \tag{3.52}$$

   The function of reference wave is

$$A_r\ sin(\omega t_m) \tag{3.53}$$

   Equate equation (3.52) to equation (3.53) to get

$$A_c(1 - |cos(m_f\omega t)|) = A_r\ sin(\omega t_m) \tag{3.54}$$

   Where the time in the m$_t h$ pulse is equal to:

$$t_m = t_x + \frac{mT_s}{2} \tag{3.55}$$

   Equation (3.54) can be expressed as follows:

$$\begin{aligned} A_c(1 - |cos(m_f\omega t)|) &= A_r\ sin(\omega\big(t_x + \frac{mT_s}{2})) \\ 1 - |cos(m_f\omega t)| &= m_a\ sin(\omega\big(t_x + \frac{mT_s}{2})) \end{aligned} \tag{3.56}$$

   Where m$_a$ is the modulation index

2. Odd Area:

   As shown in Figure 3.8c, the carrier function is

$$A_c(1 - |cos(m_f \omega t)|) \tag{3.57}$$

   The function of reference wave is

$$A_r \; sin(\omega t_m) \tag{3.58}$$

   Equate equation (3.57) to equation (3.58) to get

$$A_c(1 - |cos(m_f \omega t)|) = A_r \; sin(\omega t_m) \tag{3.59}$$

   Where the time in the $\mathrm{m}_t h$ pulse is equal to:

$$t_m = t_x + \frac{m T_s}{2} \tag{3.60}$$

   Equation (3.59) can be expressed as follows:

$$\begin{aligned} A_c(1 - |cos(m_f \omega t)|) &= A_r \; sin(\omega\big(t_x + \frac{m T_s}{2})) \\ 1 - |cos(m_f \omega t)| &= m_a \; sin(\omega\big(t_x + \frac{m T_s}{2})) \end{aligned} \tag{3.61}$$

Since the equations (3.56) and (3.61) are the same, then solving for t_x is easier. After finding t_x, we substitute it in equation (3.60) to find the angles of the $\mathrm{m}_t h$ pulse in *seconds*. This unit of the angles can be changed into degrees by multiplying the founded t_m by $2\pi f$.

The VFSPWM MATLAB code has almost the same structure of the SPWM code. It has two modulation ratio, m_{f1} and m_{f2} that are equivalent to $m_{f_{high}}$ and $m_{f_{low}}$ respectively. In this code $m_{f_{high}}$ is equal to 15 and $m_{f_{low}}$ is equal to 6. The unit conversion for the initial angles was eliminated because the angles were already in radian.

```
function H = myfun(x)
Ma=0.1
Mf1=15; % High frequency
Mf2=6; % low frequency
```

The implementation of the function *fzero* has two parts as well, carrier and reference wave. Since teh carrier has high-frequency and low-frequency, the set of *fzero* equations need to be divided into two groups. The first group is to calculate the notches for the period $[0, \frac{\pi}{3}]$. On the other hand, the second group finds the zeros for the period $[\frac{\pi}{3}, \frac{\pi}{2}]$. In this example, we tried to find eight angles.

```
ang = [fzero( @(x)1-abs(cos(Mf1*(x)))-Ma*sin(x),x(1),[0 pi/3]);
     fzero( @(x)1-abs(cos(Mf1*(x)))-Ma*sin(x),x(2),[0 pi/3]);
     fzero( @(x)1-abs(cos(Mf1*(x)))-Ma*sin(x),x(3),[0 pi/3]);
     fzero( @(x)1-abs(cos(Mf1*(x)))-Ma*sin(x),x(4),[0 pi/3]);
     fzero( @(x)1-abs(cos(Mf1*(x)))-Ma*sin(x),x(5),[0 pi/3]);
     fzero( @(x)1-abs(cos(Mf1*(x)))-Ma*sin(x),x(6),[0 pi/3]);
     fzero( @(x)1-abs(cos(Mf1*(x)))-Ma*sin(x),x(7),[0 pi/3]);
     fzero( @(x)1-abs(cos(Mf1*(x)))-Ma*sin(x),x(8),[0 pi/3]);
     fzero( @(x)1-abs(cos(Mf1*(x)))-Ma*sin(x),x(9),[0 pi/3]);
     fzero( @(x)1-abs(cos(Mf1*(x)))-Ma*sin(x),x(10),[0 pi/3]);
     fzero( @(x)1-abs(cos(Mf2*(x)))-Ma*sin(x),x(11),[pi/3 pi/2]);
     fzero( @(x)1-abs(cos(Mf2*(x)))-Ma*sin(x),x(12),[pi/3 pi/2])]
```

Finally this part uses the calculated coefficient to find the WTHD which is based on 63 harmonics. The result of the validation is presented after we explain the PSPICE model. One needs to notice that the variables name are not similar to the SPWM code but they achieve the same purpose.

```
 H=0;
for n=3:2:63

H(n)=abs((400/(n*pi))* (1-cos(n*ang(1))+cos(n*ang(2))-cos(n*ang(3))+
cos(n*ang(4))-cos(n*ang(5))+cos(n*ang(6))-cos(n*ang(7))+
```

```
cos(n*ang(8))-cos(n*ang(9))+cos(n*ang(10))-cos(n*ang(11))+
cos(n*ang(12))));
end

V1=(400/(pi))* (1-cos(ang(1))+cos(ang(2))-cos(ang(3))+cos(ang(4))-
cos(ang(5))+cos(ang(6))-cos(ang(7))+cos(ang(8))-cos(ang(9))+
cos(ang(10))-cos(ang(11))+cos(ang(12)))

THD=100*sqrt(sum(H.^2))/V1
```

3.4.2 PSPICE Model

As we mentioned before this is a second validation step where at the end of this chapter we are presenting the results of the validation. Before we show the result of the validation, we are explaining a PSPICE model that is used for the validation. The process of the validation is following the same sequence as in the mathematical section. The first part explains the PSPICE model used to simulate the SPWM technique. The second part is the PSPICE model of the VFSPMW modulation technique.

3.4.2.1 Sinusiodal Pulse Width Modulation This model consists of two 180° out of phase AC sources that represent the two sinusoidal reference waves explained in the previous sections. Also, it includes the carrier source that generates a triangular wave. These sources are shown in Figure 3.9. These two reference waves are compared to the triangular carrier to generate the gating signal. The generator signal creates a train of pulses based on the instantaneous amplitude of the reference waves and the carrier. The output of these generates is one when the reference wave is greater than the carrier wave, and zero otherwise. To perform this comparison, several process should be taken: First, the gating generator subtracts the carrier wave from the reference to determine the crossing points. The generator then transforms this signal into a one-sided by using an absolute function. By adding these two signal, the negative side is eliminated. Then a limiter with a

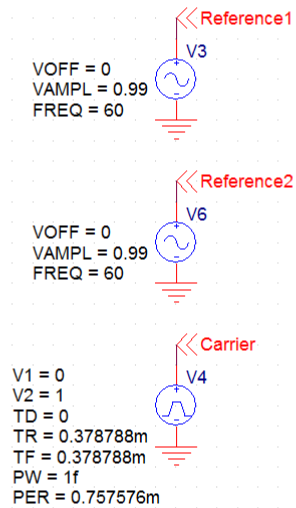

Figure 3.9: Sinusoidal PWM Reference and Carrier Generators

high gain is used to regulate the one-sided signal and ensure the transition between 1 or 0 is rapid. Figure 3.10 shows the two PSPICE gate generators where each one is assigned with a reference wave. This mechanism can be depicted in the following expression

$$gate_{1,2} = reference_{1,2} - carrier + |reference_{1,2} - carrier| \tag{3.62}$$

The signal denoted "gate_1" in Figure **??** goes to the inverter upper switch of leg A and lower switch of leg B. Where the signal "gate_2" controls the inverer lower switch of leg A and upper switch of leg A. Figure 3.11 shows the model of the full-bride single-phase inverter. The blocks denoted "Sbreak" in the figure is acting as ideal switches. The blocking resistance for these ideal switches is adjusted to 1 $M\Omega$ and the conduction resistance is set to 10 $m\Omega$. The modification to these resistances was mandatory to mimic the IGBT switches in the PSCAD model. Hence, the switching time (slope) of the two models,PSCAD and PSPICE, should be similar. This step ensures the accuracy in the validation. The gating signal and the inverter output are shown in Figure 3.12. The upper plot is the triangular carrier with the two sinusoidal reference waves. The two next plots are the gating signals for leg A and leg B. The last plot is the inverter output that represents the desired wave (reference wave).

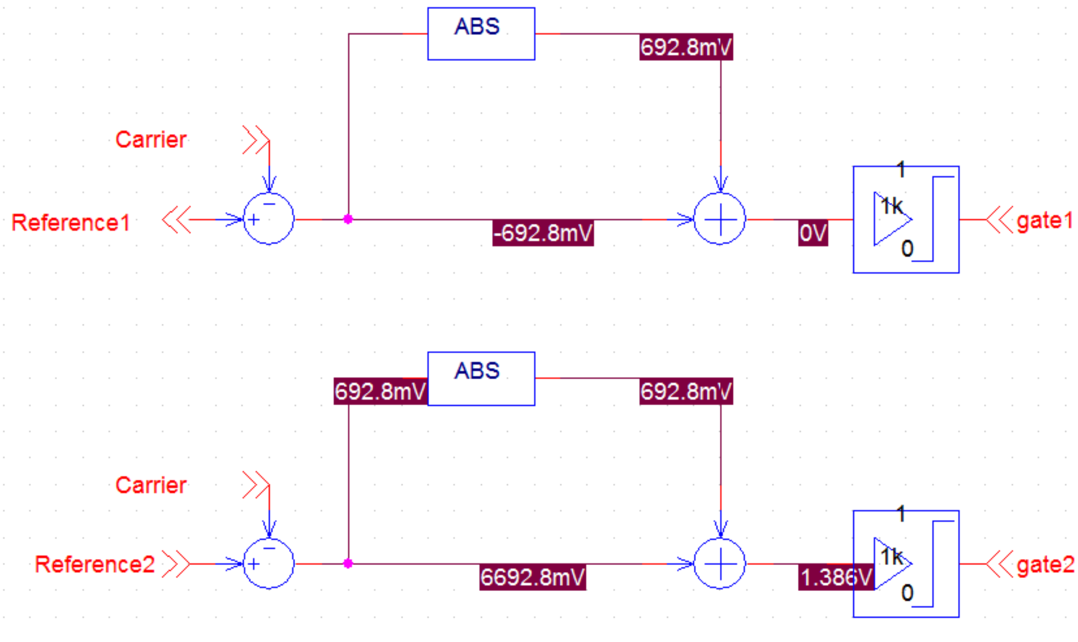

Figure 3.10: SPWM Gating Generator

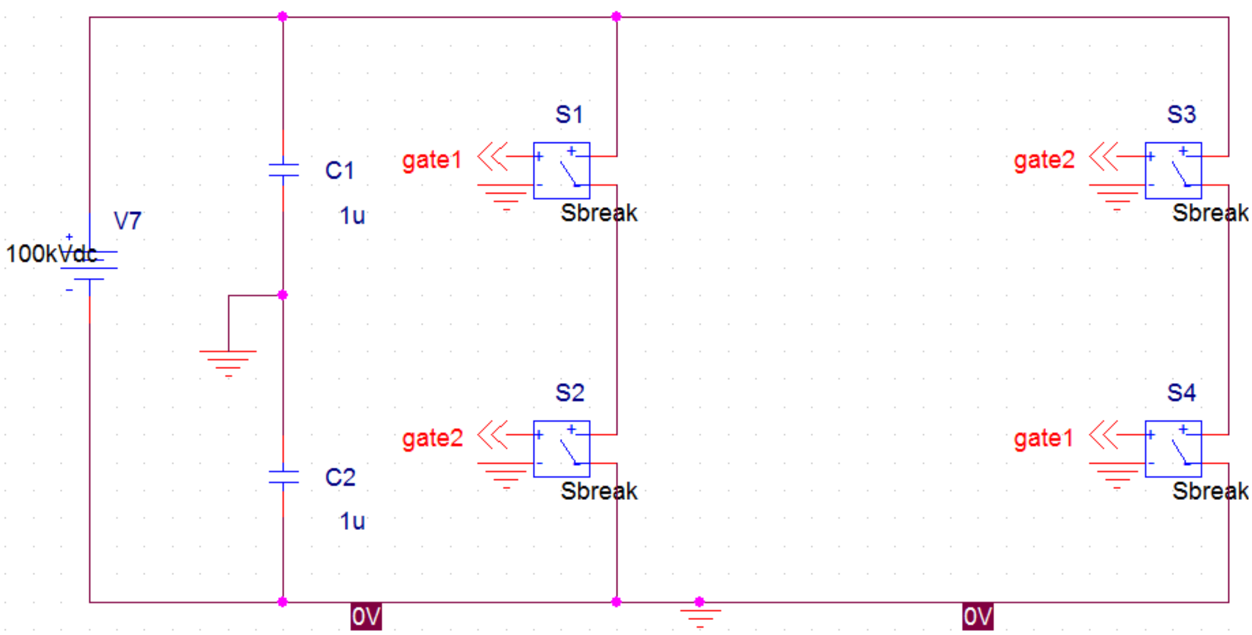

Figure 3.11: Full-Bridge VSI Model

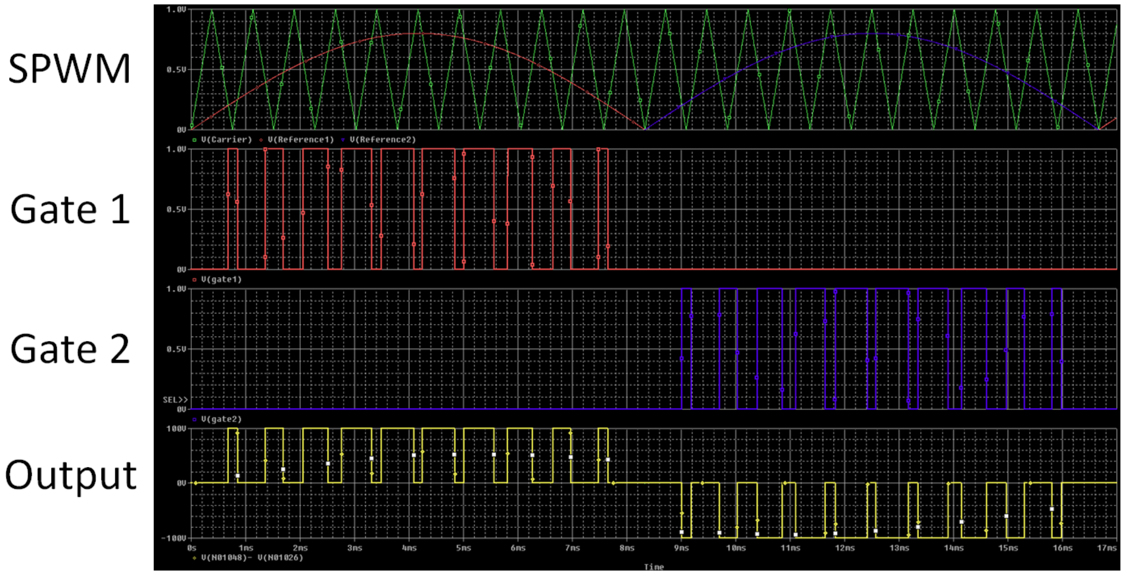

Figure 3.12: SPWM gaiting signal and output

3.4.2.2 VFSPWM This model has several common parts with the SPWM model such as the sinusoidal wave sources, the gating generator and the full-bridge voltage-source inverter. It is better to describe the carrier because it is the only part that is different from the SPWM PSPICE model. The carrier model shown in Figure 3.13 consists of a high-frequency carrier generator and a low-frequency carrier generator, $m_{f_{high}} = 5$ and $m_{f_{low}} = 3$ respectively. Each generator contains a sine wave source that is rectified to the positive side by using the absolute built-in function. This rectified wave is then flipped to the negative side by multiplying it by (-1). Then it is shifted to the positive side to form the inverse sinusoidal carrier. These two carrier signals are then multiplexed to create the one carrier that switches in high-frequency for the first and last 60° per half-cycle while switching at low-frequency for 60° in the middle of the half-cycle. This process is achieved by using two digital clocks. Each clock has a frequency of 120° and a duty cycle equals to 50%. They control two ideal switches, denoted "Sbreak" in the Figure 3.14, to alternate between the two carrier signals. The gating signal in Figure 3.10 is using this carrier to control the switches of the VSI in Figure 3.11. The new carrier, gating signal, and the inverter output are all shown in Figure

3.15. The upper plot is the variable-frequency inverse sinusoidal carrier with the two sinusoidal reference waves. The two other plots are the gating signals of leg A and leg B. The last plot is the inverter output that represents the desired wave (reference wave).

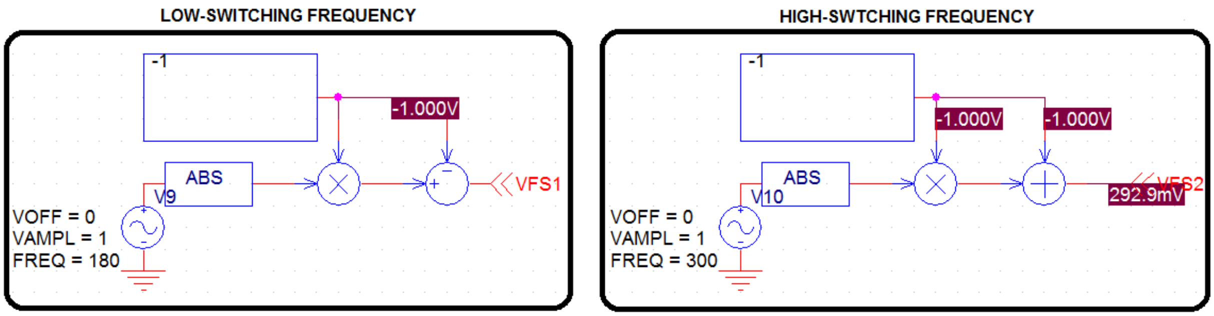

Figure 3.13: Two VFSPWM Carrier with Different Frequencies

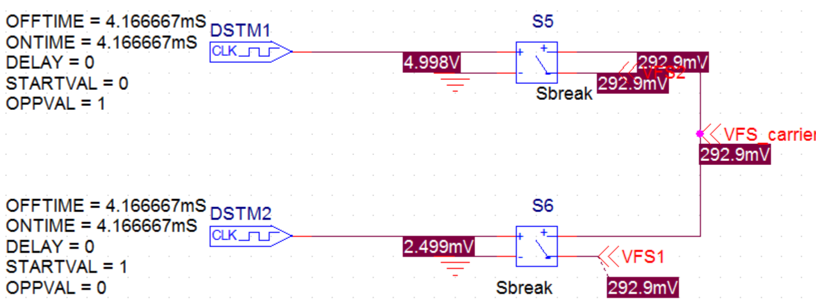

Figure 3.14: VFSPWM Carrier Generator

3.4.3 Validation Result

To ensure that the PSCAD model is accurate to assist in evaluating the VFSPWM algorithm, A validation stage must be conducted. In this section the validation is based on two measurements parameters: the spectrum and the WTHD of the inverter outputs. We are comparing the WTHD and the harmonic coefficients, up to 63 harmonics, for the PSCAD, PSPICE, and the mathematical model. The SPWM technique is validated first then we apply the same validation process to the VFSPWM technique.

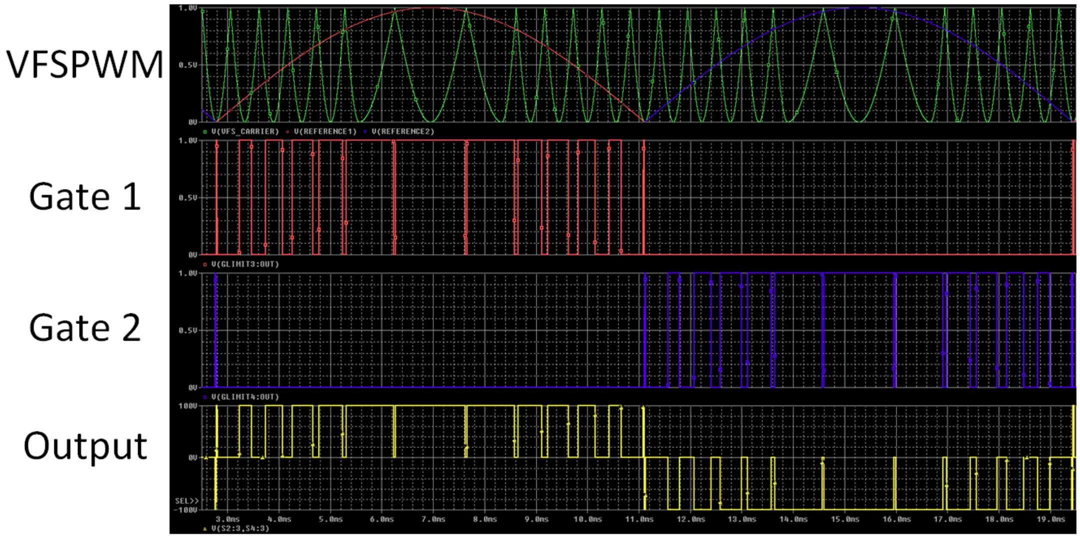

Figure 3.15: VFSPWM outputs

3.4.3.1 Sinusoidal Pulse-Width Modulation We start the comparison when $m_f = 12$. Figure 3.16 shows the Spectrum for the SPWM with $m_a = 0.9$ and $m_f = 12$. The spectrum for the three models is almost identical. Figure 3.17 shows the V_1 percent error of the PSPICE and the PSCAD models, besides, the V_1 percent error of the mathematical and PSCAD model to measure the differences among the three models versus m_a. The highest error percent occurred at $m_a = 1$ and its value is smaller than 1.2%. The spike at $m_a = 1$ is caused by the different behavior of the models when the peak of the reference wave is equal to the peak of the carrier wave. The WTHD percent error versus m_a is shown in Figure 3.19. The difference among the three models is really small. This difference is calculated in percent error, with PSCAD as reference, to expose the difference clearly, Figure 3.18. The percent error is low where the highest one is at m_a and is equal to 1% because the MATLAB code does not include the blocking and conduction resistances in the calculation. The rest of the percent error are smaller than 0.5%. This confirms the validity of the the PSCAD model.

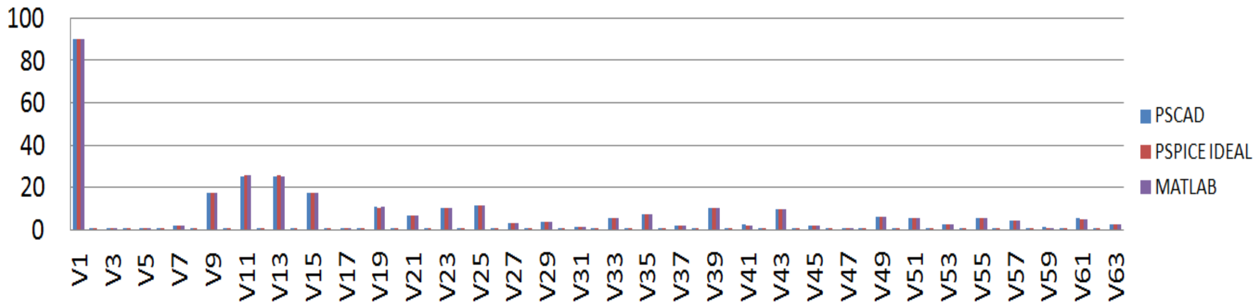

Figure 3.16: SPWM Spectrum - Ma=0.9 , Mf=12

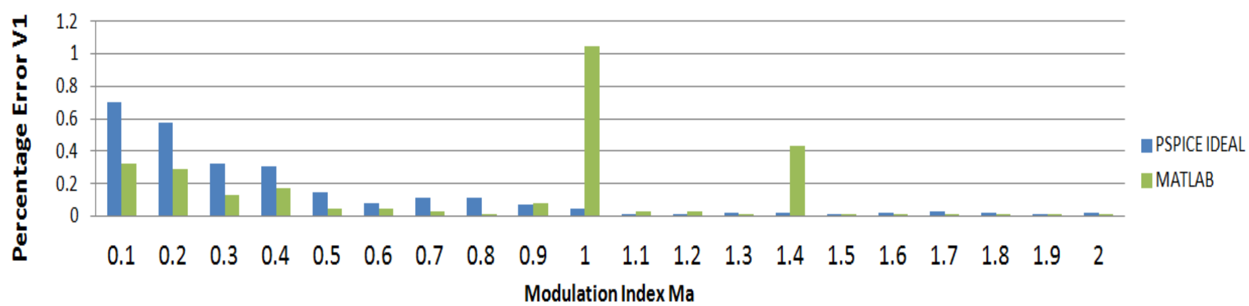

Figure 3.17: SPWM Error

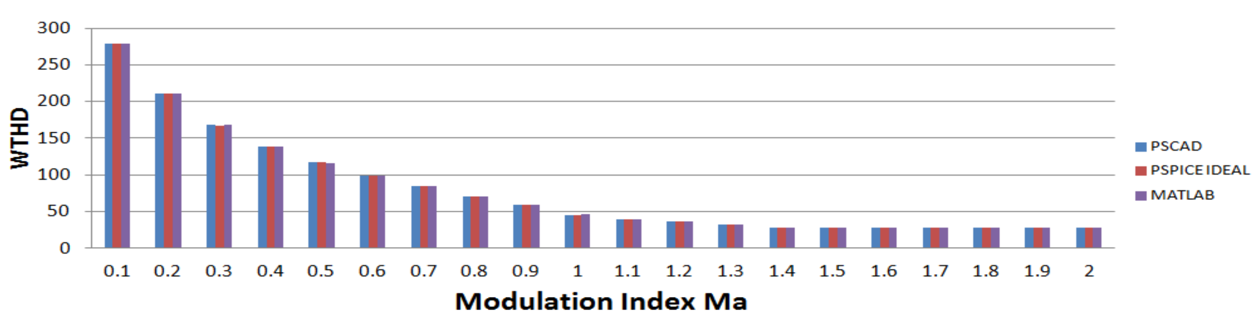

Figure 3.18: SPWM THD

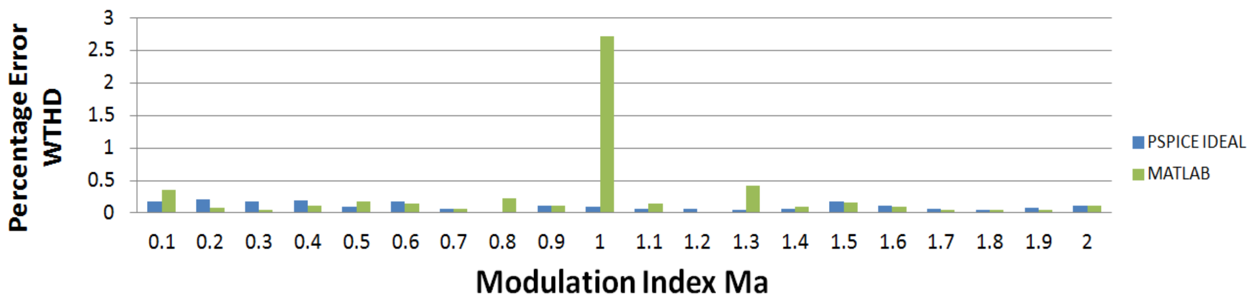

Figure 3.19: SPWM THD Percentage Error

3.4.3.2 VFSPWM We arbitrary chose $m_{f_{low}} = 3$ and $m_{f_{high}} = 9$ for this validation process. Figure 3.20 shows the Spectrum for the VFSPWM when $m_a = 1$, for 63 harmonics. The three models are almost identical and the difference is significantly small. Figure 3.21 shows the percent error of the PSPICE and the PSCAD models, besides, the percent error for the mathematical and PSCAD model with the change of m_a. The percent error is smaller that 0.3% which confirms the validity of the PSCAD model. The next step is to compare

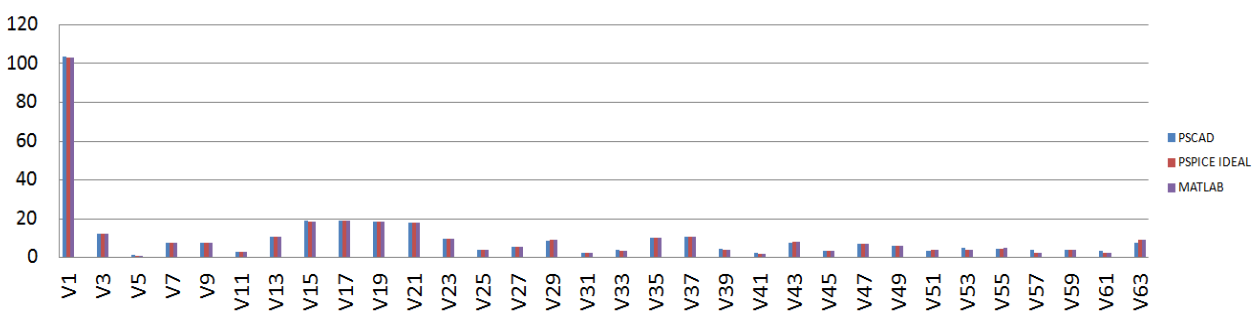

Figure 3.20: VFSPWM Spectrum - $m_a = 0.9$, $m_{f_{low}} = 3$ and $m_{f_{high}} = 9$

the WTHD. The percentage error of the WTHD versus m_a is shown in Figure 3.20. The the three models are closely matched. The percentage error of the WTHD is depicted in Figure 3.22. As can be seen, all the values of the percentage error reside below 1.2%. After these two validation steps we can assure the validity of the PSCAD models.

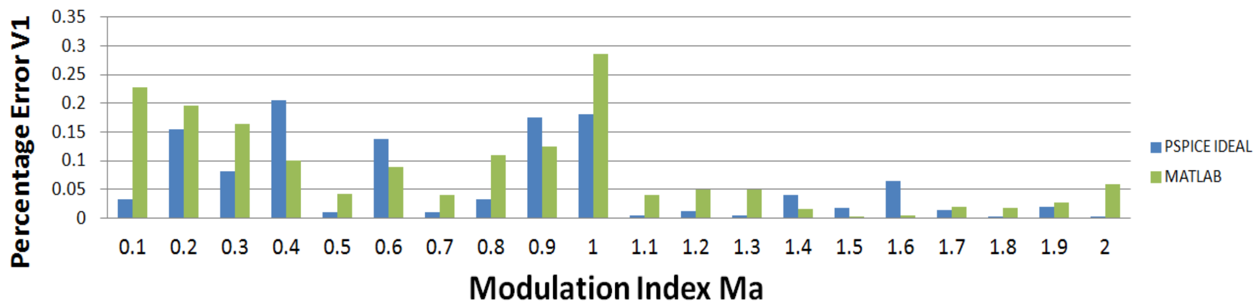

Figure 3.21: VFSPWM Percentage Error

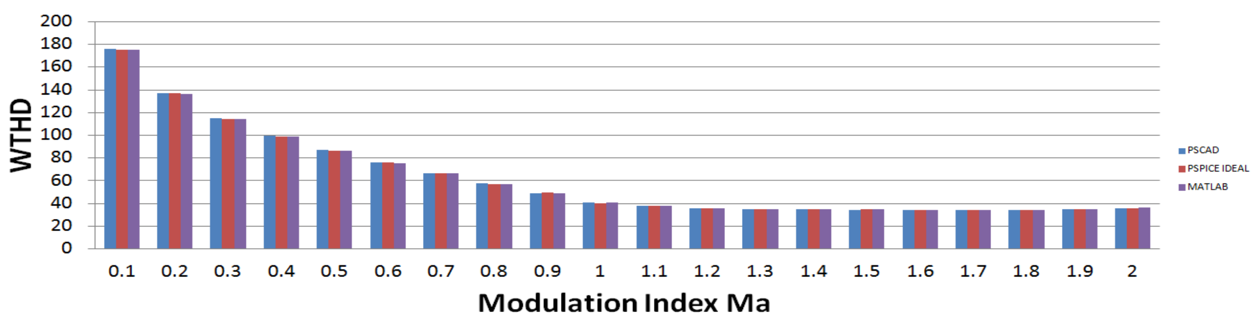

Figure 3.22: VFSPWM THD

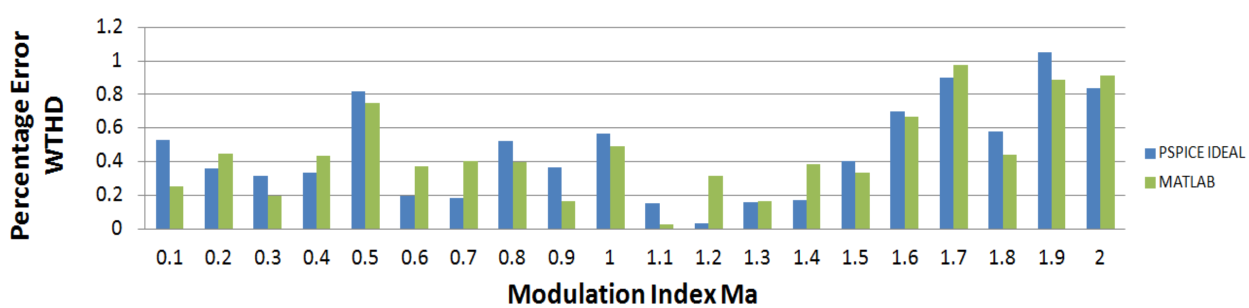

Figure 3.23: VFSPWM THD Percentage Error

3.5 OTHER MODULATION TECHNIQUES

I the previous sections we presented the analysis of the VFSPWM technique. Also we described the models we built to help in evaluate the performance of this new modulation algorithm. Furthermore, we emphasized these procedures by analyzing and building models of the SPWM because it is the benchmark of this evaluation. Before we show the results of the comparisons between the VFSPWM and SPWM technique, we prefer to add two more commonly used modulation technique to help in generalize the comment in the results to an acceptable extent. The two additional techniques are the sawtooth PWM and the modified PWM. In this section we built and described two PSCAD models that represent the sawtooth PWM and the modified SPWM. The difference between the SPWM model and these two is the carrier generator only. Therefore, we changed and explained the components of the carrier generator while used the other SPWM components.

3.5.1 Sawtooth Pulse-Width Modulation

The carrier generator in this model is similar to that of the SPWM model. In order to generate a sawtooth carrier, the carrier configurations, shown in Figure 3.24, need to be changed. If the duty cycle is 50% the carrier generator will create the SPWM triangular wave. This duty cycle needs to be changed into 100% to form the sawtooth carrier designated for the sawtooth PWM techinque. In this Figure, the m_f is equal to 12 (720 Hz) and the phase shift is zero. The carrier waveform along with the two reference waves are shown in Figure 3.25. This carrier is known as *trailing edge modulation* where the modulation is occurring during the sloppy curve. If the sloppy curve is left sided, then this technique is called *leading edge modulation*. In this section we are discussing the trailing edge due to the fact that the performance of the two modulation techniques is similar. The comparison between the this carrier and the reference wave is achieved by the same comparator used for the the SPWM. This comparator generates the gating signals that control the switches in the full-bridge voltage-source inverter. This technique performances exactly like the SPWM during the linear region, $0 \leq m_a \leq 1$.

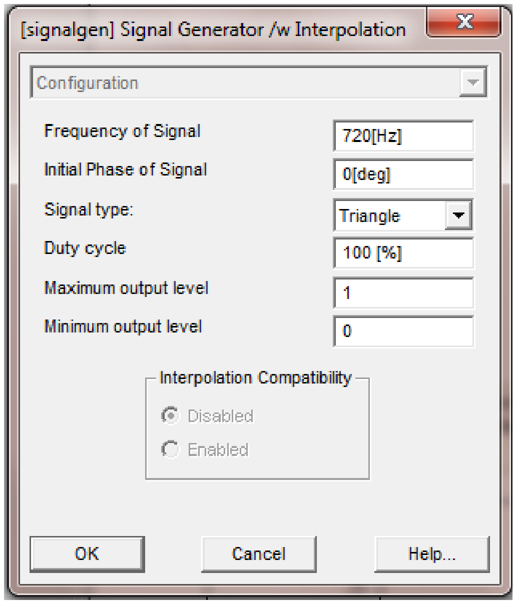

Figure 3.24: Sawtooth PWM Carrier Generator Configuration

3.5.2 Modified Pulse-Width Modulation

The carrier generator for the modified PWM is complicated in comparison to that of the SPWM and sawtooth PWM. This carrier, depicted in Figure 3.26, consists of two frequency sources, triangular wave generator and a zero source. A two input selector is used to alternate between these two sources. This selector switches to channel A (the triangular wave) when the value of the selector control input is 1. On the other hand, it switches to channel B (zero frequency) when the selector control input is 0. A pulse generator is connected to the two input selector control to control the selector by creating pulses varies between 0's and 1's. This pulse controller switches for 120Hz (twice the fundamental frequency) with duty cycle equals to 2/3 the cycle. To ensure that the carrier and the reference wave are in phase, the phase angle of the carrier is set to 120°. This structure guarantees that the switching is happening during the first and last 60° per half-cycle with no switching at all between these two period. The carrier and the two reference waves are shown in Figure 3.27.

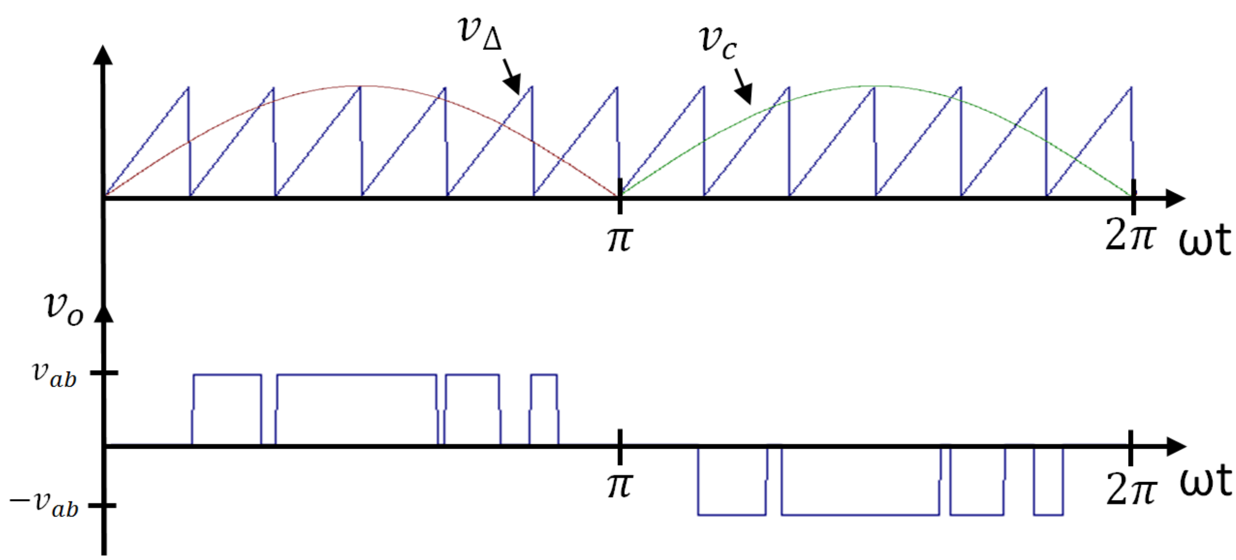

Figure 3.25: Sawtooth PWM

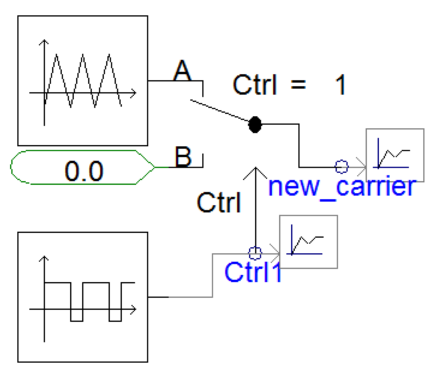

Figure 3.26: Modified PWM Carrier Generator

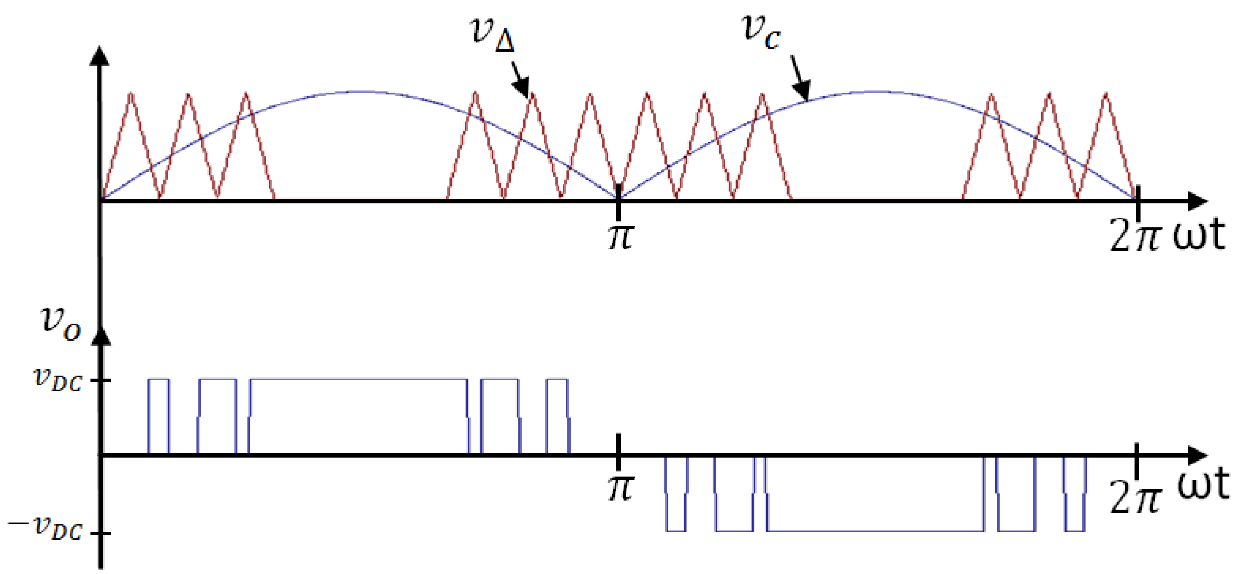

Figure 3.27: Modified PWM Carrier

4.0 SINGLE-PHASE VFSPWM

The comparison in this section shows the result of the fundamental component and the WTHD vs the modulation index. The SPWM technique is the reference (benchmark) algorithm due to the fact that this technology is the most commonly used in the industry. The modulation techniques are grouped into the same switching frequency and the same stress.

4.1 SIMILAR PULSES

To evaluate the new modulation technique, one way to do the comparison with the SPWM is by checking the fundamental component and the WTHD for the modulation techniques while the number of pulses in the inverter output voltage is the same; hence lower switching losses. In the VFSPWM there are two switching frequencies. The combination of these two frequencies must generate a carrier wave that has the same pulses per cycle for the SPWM. Figure 4.1 shows an example of the SPWM and the VFSPWM having the same number of pulses in half-cycle, 5 pulses. This can be achieved by equating the average of these two frequencies to the SPWM frequency. If we examine the VFSPWM carrier for one cycle, we will find that it can be divided into 6 areas. 4 areas switch at high frequency and 2 areas switch at low frequency. Therefore, equation (4.3) shows the calculation of the VFSPWM switching frequencies that would result in the same number of pulses per cycle as in the SPWM. An example of the VFSPWM switching frequencies that correspond to the SPWM technique with m_f equal to 10 and 12 is shown in Table 4.1.

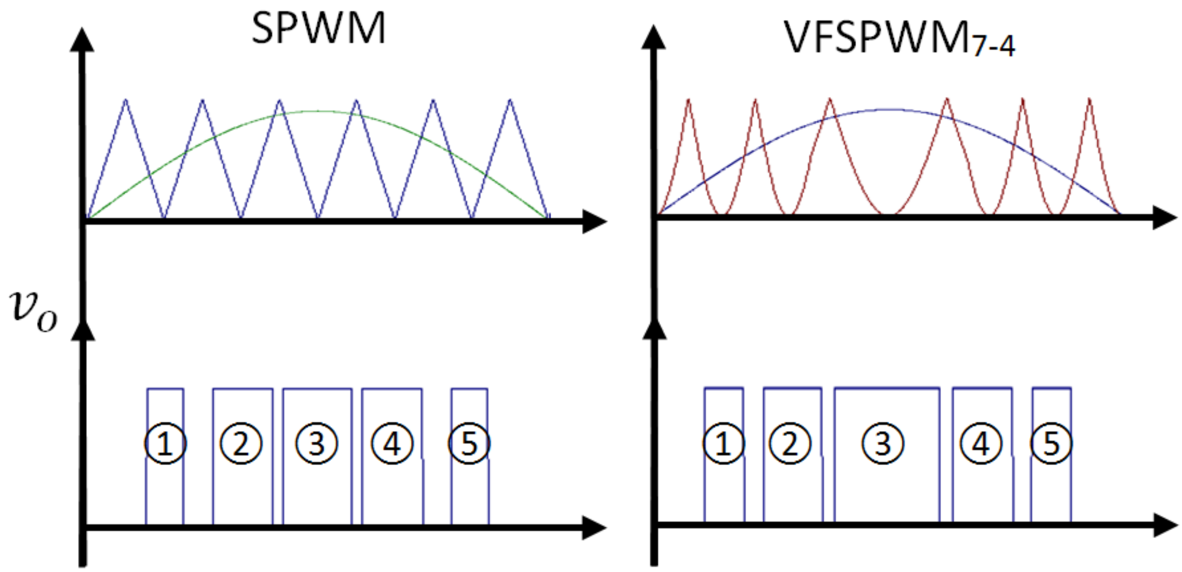

Figure 4.1: Same Pulses Test (SPWM$_{12}$ and VFSPWM$_{7-4}$)

$$f_{SPWM} = \frac{4f_{VFSPWM_H} + 2f_{VFSPWM_L}}{6} \tag{4.1}$$

Since the VFSPWM technique uses the unidirectional form, the new f_{SPWM} should be one half f_{SPWM} to yield the following

$$\frac{f_{SPWM}}{2} = \frac{4f_{VFSPWM_H} + 2f_{VFSPWM_L}}{6} \tag{4.2}$$

$$f_{SPWM} = \frac{4f_{VFSPWM_H} + 2f_{VFSPWM_L}}{3} \tag{4.3}$$

Where f_{SPWM} is the SPWM switching frequency,
f_{VFSPWM_H} is the VFSPWM high switching frequency and
f_{VFSPWM_L} is the VFSPWM low switching frequency.

Table 4.1: Switching frequencies corresponding to the SPWM switching frequency

f_{SPWM}	f_{VFSPWM_H}	f_{VFSPWM_L}
10	7	1
10	6	3
12	8	2
12	7	4
12	9	0

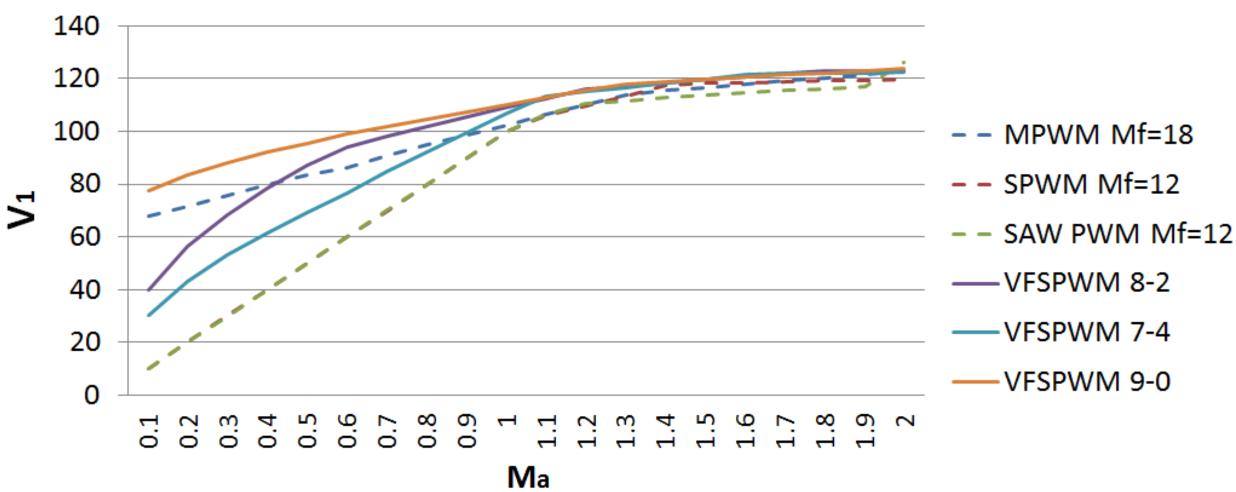

Figure 4.2: The Fundamental Component (V1) Comparison in the Similar Pulses Test

4.1.1 Voltage Fundamental Component

The comparison of the modulation techniques can be illustrated in Figure 4.2. In this comparison, m_f of the SPWM technique has been chosen arbitrary to be equal to 12. The switching frequency of the MSPWM can be calculated as follows

$$f_{MPWM} = \frac{3\ f_{SPWM}}{2} \tag{4.4}$$

As can be seen, the increase of V_1 is, generally, proportional to the increase in m_a. Starting at $m_a = 0.1$, $VFSPWM_{9-0}$ has the highest fundamental component all the way to $m_a = 1$. where $VFSPWM_{8-2}$ increases rapidly to be the second highest at $m_a = 0.4$ because the inverter switches are staying ON longer in the period of the low frequency. Unlike the $VFSPWM_{8-2}$, $VFSPWM_{7-4}$ has a smaller slope but higher than that of the MPWM at $m_a = 0.9$. The three VFSPWM curves gain the highest fundamental component for most of the m_a values. This result leads to the conclusion that all the VFSPWM techniques are showing better utilization of the DC source over the SPWM, Sawtooth PWM and MPWM methods. Yet, they all lack for the linearity associated with the SPWM, Sawtooth PWM and MPWM techniques. The suddent increase in the MPWM at $m_a = 1.9$ caused by the change of the multiple gating pulses per cycel into one single pulse, this signal is known as square wave. This square wave usually causes significant increase in the output distortion.

4.1.2 Harmonics Distortion

As we mentioned before, The harmonic reduction is of great importance. The WTHD equation (3.30) stated before shows that an increase in the harmonics would cause a proportional increase in the WTHD as well. However, any increase in the fundamental component that is greater than the increase in the harmonics would decrease the WTHD. Therefore, we found it beneficial to present the square values of the harmonics to examine any increase isolated from the fundamental component. This harmonic examination is shown in Figure 4.3. SPWM and Sawtooth PWM have the lowest harmonics. However, these harmonics increase with the increase of m_a. This increase is sharper than the other modulations because the lower-order harmonics are proportionally increasing. Hence, their harmonics are

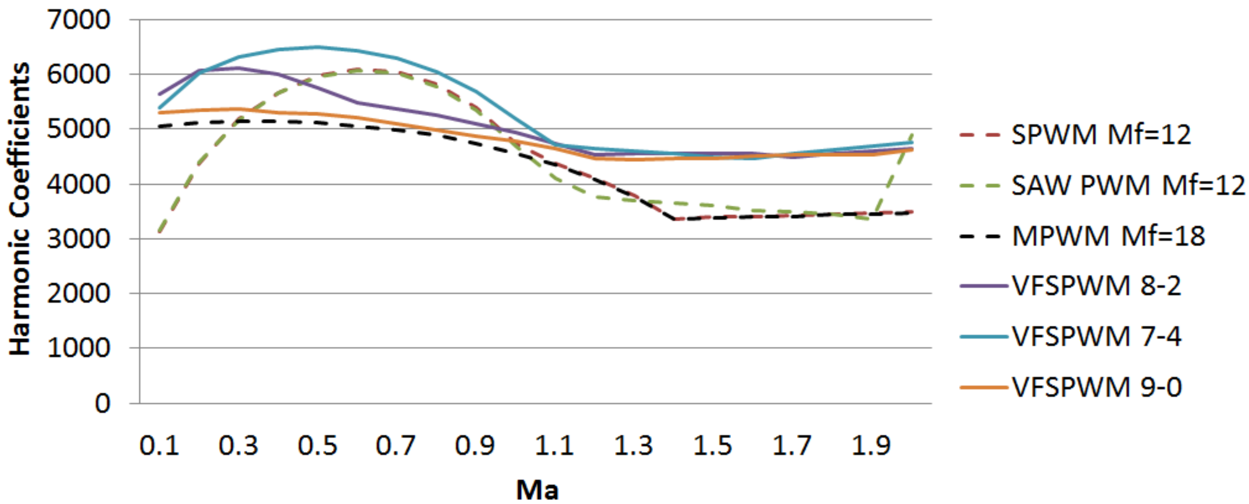

Figure 4.3: The Weighted Voltage Harmonics in the Same Pulses Test

worse than MPWM and $VFSPWM_{9-0}$ at $m_a = 0.3$. Between $m_a = 0.4$ and $m_a = 0.5$ the highest harmonic in the SPWM technique is the 11^{th} harmonic, $V_{11} = 36$ where the 13^{th} harmonic is the highest in $VFSPWM_{8-2}$, $V_{13} = 28.6$. Therefore, $VFSPWM_{8-2}$ does better at this point. Unfortunately , $VFSPWM_{7-4}$ carried the highest harmonics through out the comparison because the 11^{th} harmonic is the highest in addition to the $3^{th}, 5^{th}, 7^{th}$ and 9^{th}. In the overmodualtion region, all the VFSPWM techniques are about %33 higher that the other modulations. This is due to the fact that the 3^{rd} harmonic has the highest weight and it is increasing by the increase of m_a in the overmodulation region.

It is recommended to show the ratio between V_1 and the weighted harmonics. Therefore, we are using WTHD in equation (3.30). Figure 4.4 shows the WTHD of the modulation techniques. for low m_a, the WTHD for $VFSPWM_{9-0}$ and MPWM are indicating good performance because the V_1 is considerably high. Since V_1 and the harmonics for $VFSPWM_{8-2}$ are improving rapidly, the WTHD is decreasing sharply to make $VFSPWM_{8-2}$ the second best modulation technique among the others at $m_a = 0.6$. When $m_a \leq 1$ the three VFSPWM methods started with %45 to %80 better performance than the SPWM and Sawtooth SPWM. On the other hands, they tend to be closer to each other and when $m_a \geq 1$.

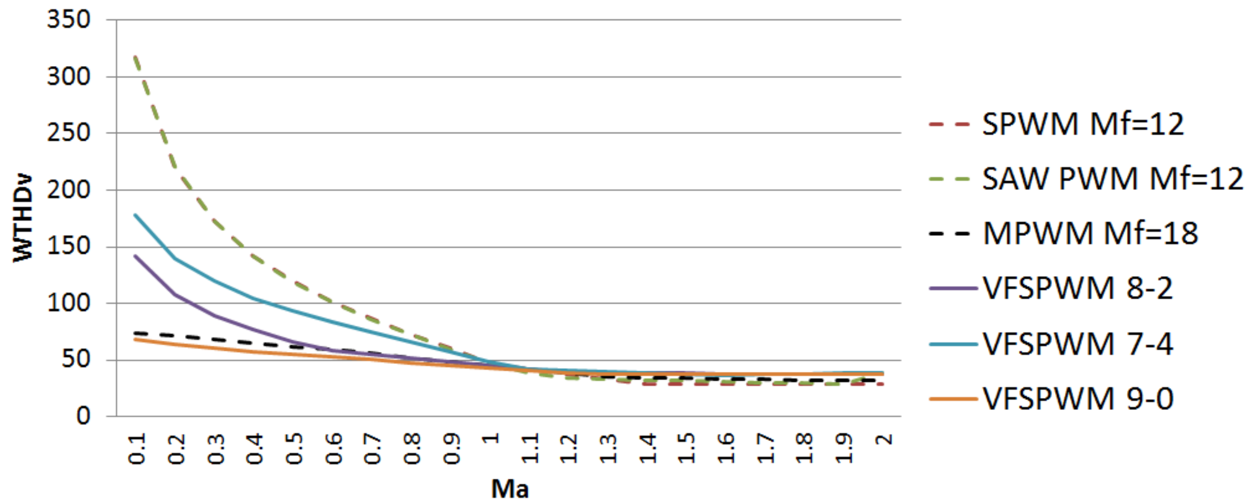

Figure 4.4: Voltage WTHD in the Same Pulses Test

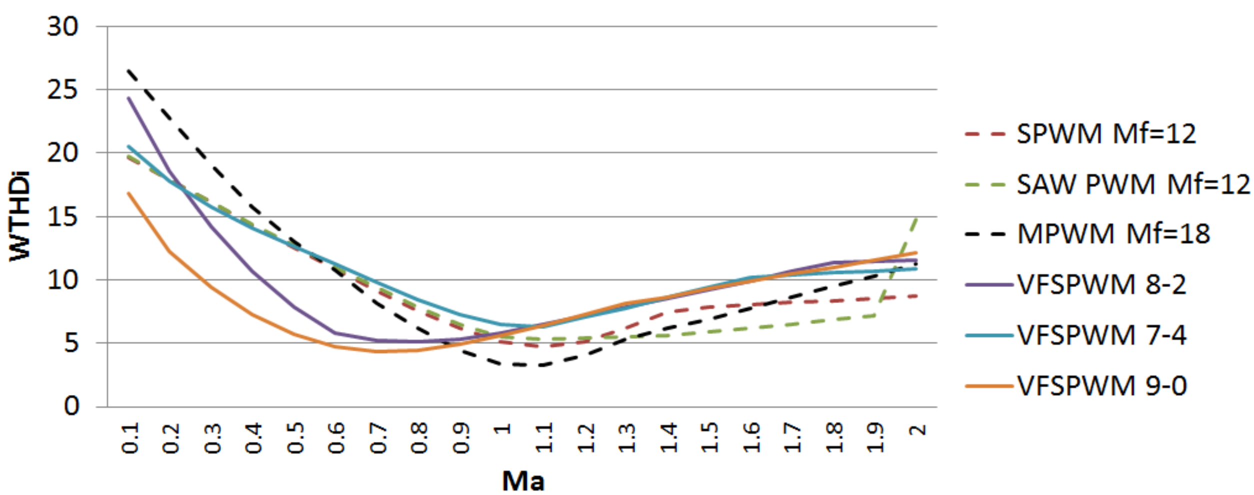

Figure 4.5: Current WTHD in the Same Pulses Test

The ratio between the current ripple goes through the load and the fundamental current I_1 is shown in Figure 4.5. $VFSPWM_{9-0}$ method stated as the best technique to achieve the minimum WTHD at $m_a = 0.75$. The WTHD for $VFSPWM_{8-2}$ has improved quickly to be the second best method up to $m_a = 0.85$. At $m_a = 1$, SPWM, Sawtooth PWM, $VFSPWM_{9-0}$ and $VFSPWM_{8-2}$ have almost the same WTHD value.

4.2 SIMILAR STRESS

Previously we compared the modulation technique with the same number of pulses per cycle. In this section we examine the modulation techniques with the same stress, $\frac{dv}{dt}$. In other words, we chose the VFSPWM techniques that satisfies this expression $f_{SPWM} = f_{VFSPWM_H}$. That means the number of pulses in the first and last 60° per half-cycle is the same of the modulation techniques we are evaluating. For example, If $f_{SPWM} = 12$, then the same stress test will assign the following switching frequencies to the VFSPWM technique : (6-3) and (6-0) along with $MPWM_{m_f=12}$. Figure 4.6 show an example of the same stress test.

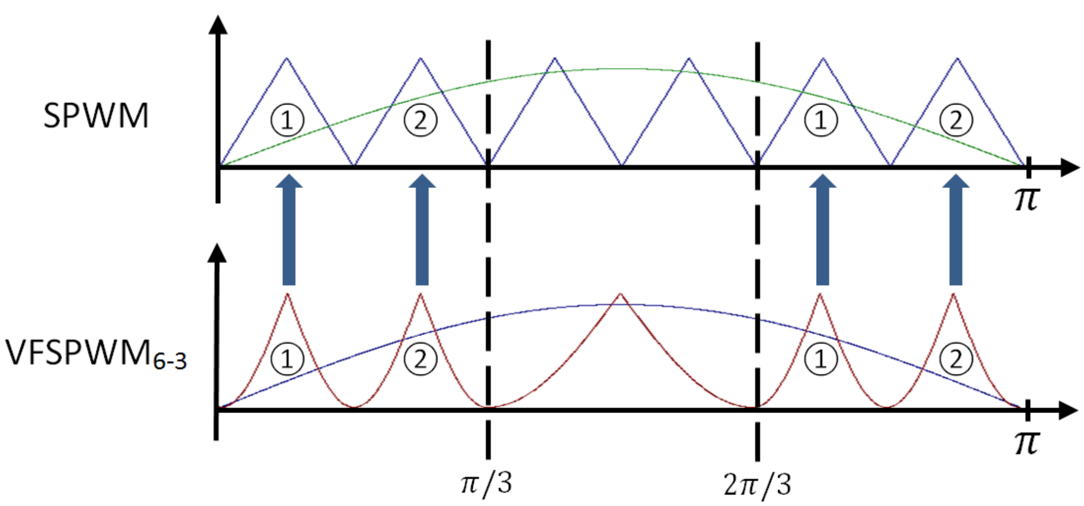

Figure 4.6: Same Stress Test(SPWM $_{12}$ and VFSPWM $_{6-3}$)

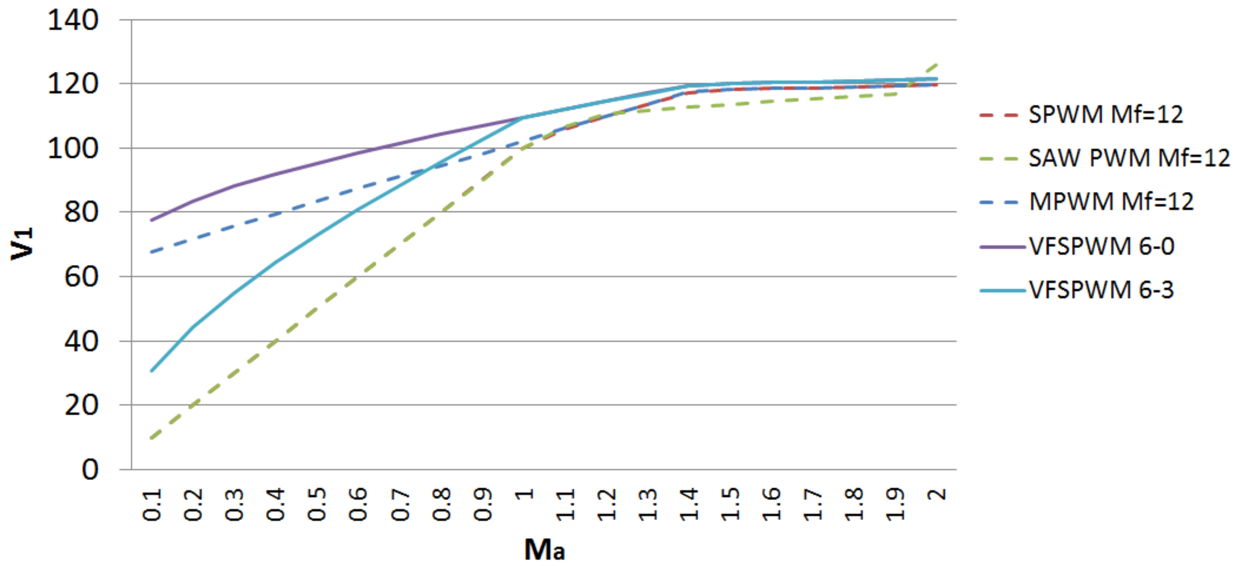

Figure 4.7: V1 vs Ma, Mf=12 with the same stress

4.2.1 Voltage Fundamental Component

In Figure 4.7, It can be observed that $VFSPWM_{6-0}$ has the highest fundamental component while the second highest is the MSPWM technique up to m_a is equal to 0.7 where the $VFSPWM_{6-3}$ is becoming the second highest fundamental component. At this point $VFSPWM_{6-0}$ and $VFSPWM_{6-3}$ are behaving identically when m_a is greater than 0.7. The average of the increase in the fundamental component in the $VFSPWM_{6-0}$ is about 80 % of the SPWM technique. On the other hand, the average of the improvement in the fundamental of the $VFSPWM_{6-3}$ is about 33.3 % of the SPWM. Both $VFSPWM_{6-0}$ and $VFSPWM_{6-3}$ does not lose the linearity feature in the linear region, however, the slope of the $VFSPWM_{6-0}$ technique is low which may be considered as a draw back as we will see in the STATCOM application in Chapter 8.

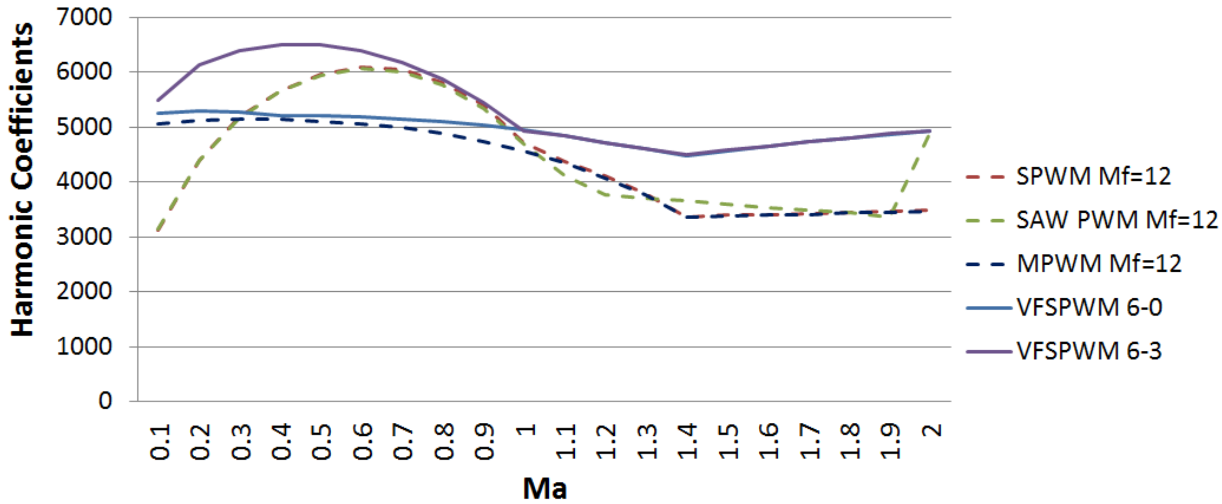

Figure 4.8: The Weight of the Voltage Harmonics vs The modulation Index with same Stress

4.2.2 Harmonics Distortion

As can be seen in Figure 4.8, $VFSPWM_{6-3}$ has the highest weighted harmonics in this examination. At $m_a = 0.3$ the sharp increase in harmonics for the SPWM and Sawtooth PWM techniques made $VFSPWM_{6-0}$ and MPWM the preferred modulation methods. The harmonics that form the $VFSPWM_{6-3}$, SPWM and Sawtooth PWM are almost the same starting from $m_a = 0.7$. Although, the VFSPWM technique is not as good as the SPWM, Sawtooth PWM and MPWM in the overmodulation region, $m_a \geq 1$, this region is rarely manipulated in the industry.

The trade off between V_1 and the weighted harmonics is shown in Figure 4.9. Although, VFSPWM technique has higher harmonics, the WTHD shows that they are better than the SPWM and Sawtooth PWM when $m_a \leq 1$. For example, the WTHD at low m_a for the VFSPWM techniques are lower by 25% to 50% of that for the SPWM and Sawtooth PWM techniques. At $m_a = 0.7$ most of the VFSPWM have the same weighted harmonics and improvement in the WTHD by %20 to %40. In the overmodulation region, the WTHD for all the modulation techniques are the close to each other.

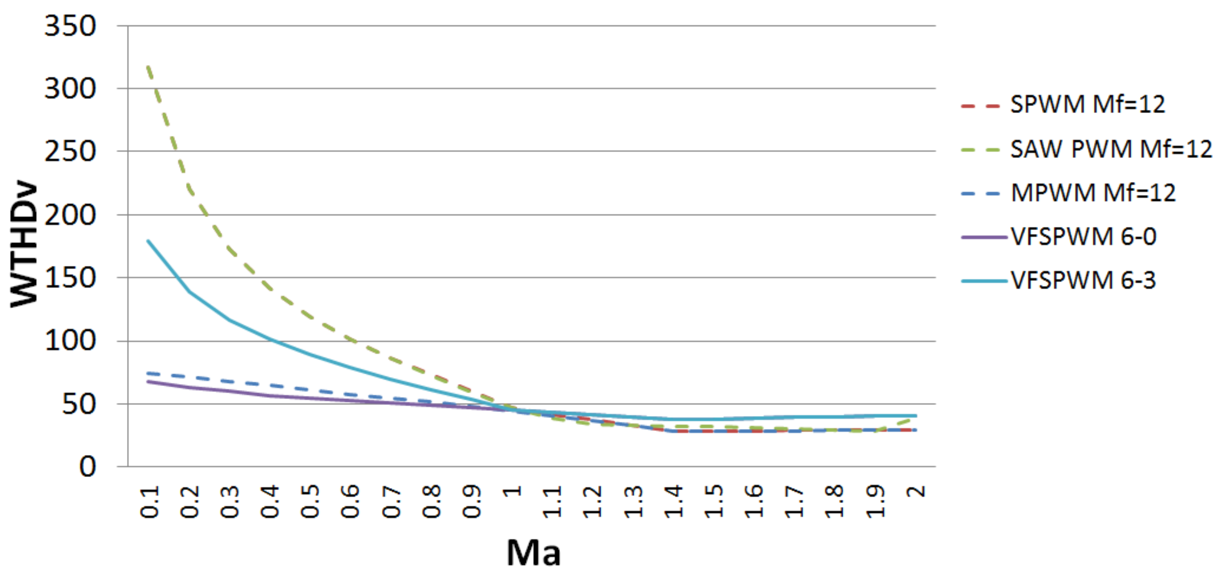

Figure 4.9: Voltage WTHD of the modulation techniques with the same stress

5.0 REAL MODEL

In section (3.4) we represented the model mathematically and built an ideal PSCPICE model for the validation. In this section we are examining the performance of the VFSPWM modulation techniques in the industry by simulate a PSPICE model using real components instead of ideal components. These real components of the PSPICE model are described first and then the performance of the model will be evaluated.

5.1 PSPICE MODEL

This model has the same two blocks of the ideal PSPICE model we explained before, VSI and controller, except that these blocks contain different parts in the real model.

5.1.1 Voltage-Source Inverter

The single phase voltage-source inverter consists of a DC source that feeds through two legs, leg A and leg B. Leg A is designed to generate the positive part of the inverter. On the other hand, the negative part is generated from the switching devices in leg B. Each leg has an upper and lower switching devices. The switching device is composed of one of more IGBT devices in parallel with one or more feedback diodes. Figure 5.1 shows the inverter containing the DC source and the two legs including the upper and lower switching devices. The "IXGH40N60" model is chosen to be the IGBT devices in the voltage-source inverter because it has a high switching capability, 300 ns to rise and 800 ns to fall. The datasheet of the "IXGH40N60" IGBT is presented in the appendix.

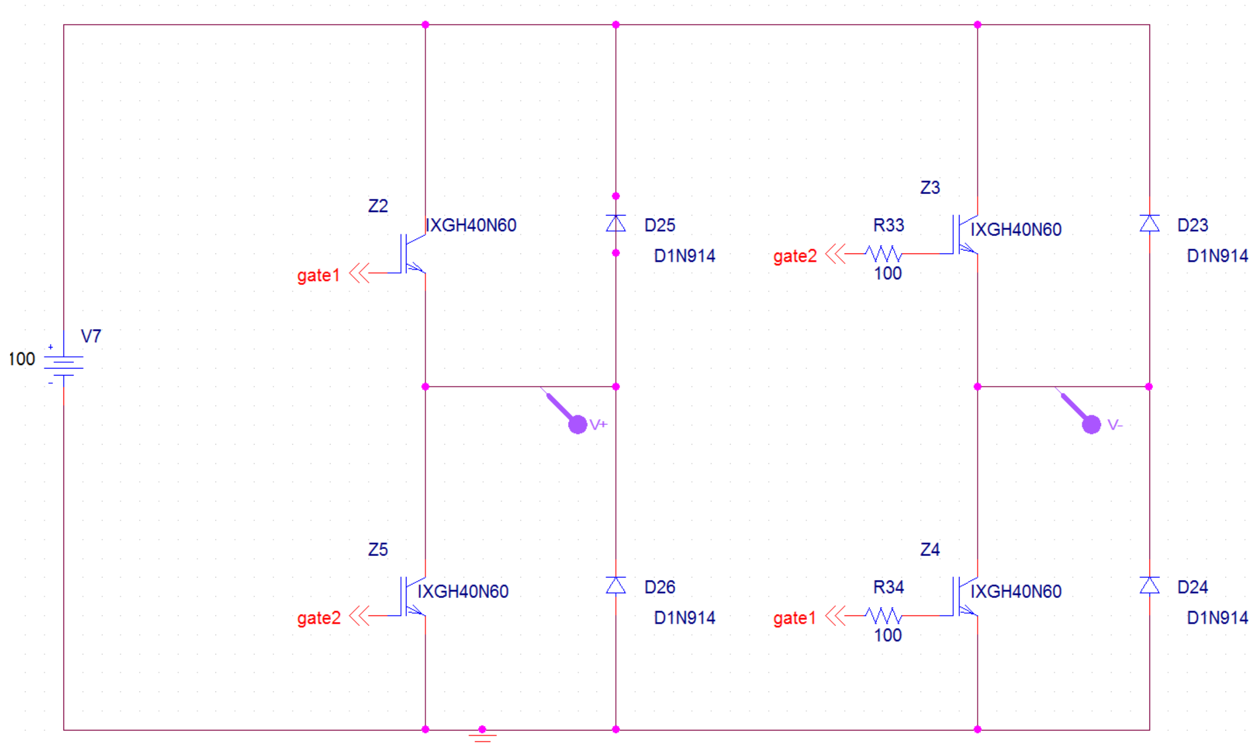

Figure 5.1: The Real Model Single-phase Voltage-Source Inverter

5.1.2 Inverter Controller

Each converter requires a controller that generates a set of pulses as a gating signal to turn the switching devices ON and OFF in a special pattern that forms a desired output.

5.1.2.1 Reference Generators This model contains reference generators to synthesize two sinusoidal waves. The two sinusoidal waves are 180° out of phase. The first one is dedicated for the positive side which is denoted as leg A. The second wave is for the negative pulses, leg B. Figure 5.2 shows the two reference generators where the first wave generator is labeled reference 1. This wave is shifted to $-60°$ to simplify the synchronization with the carrier wave that is described in the next section. The second wave generator is labeled reference 2 and shifted to 120°.

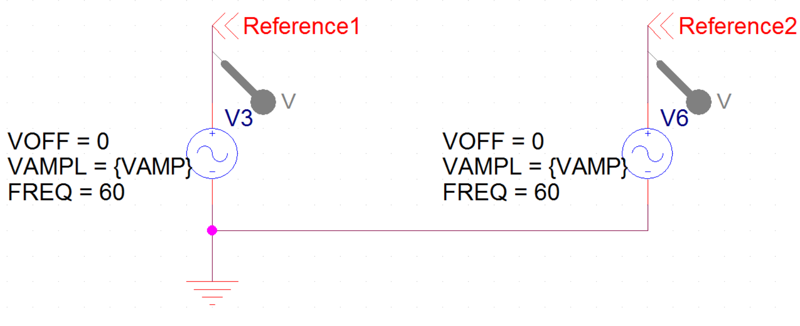

Figure 5.2: The Real Model Reference Waves Generator

5.1.2.2 Carrier Generator The carrier generator consists of two parts, carrier waves source and multiplexer. The carrier waves source provides a high frequency carrier and a low frequency carrier. Each carrier wave is generated from a sinusoidal source. Then it is rectified by using an absolute function. This rectified function is then flipped to the negative side by multiplying the wave by (-1). Finally, this wave is offset to the positive side by adding a constant value (1). This process can be seen in Figure 5.3. The two input multiplexer combine these two carriers to form the VFSPWM carrier where these two carriers are the input waves. This multiplexer consists of two switches. Each switch turns ON for 60° and

OFF for another 180°. Two digital clocks "DSTM" are controllers that generate switching pulses to operate the switches. The first controller is for high switching frequencies and the second one is for low switching frequencies. Figure 5.4 shows the multiplexer.

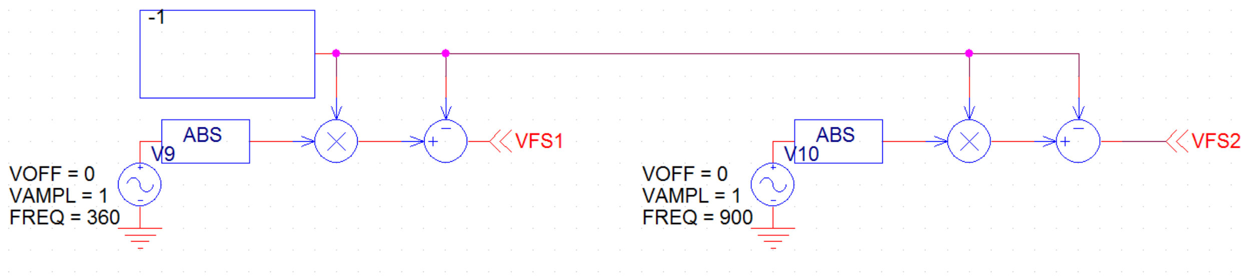

Figure 5.3: The Real Model Carriers Generator

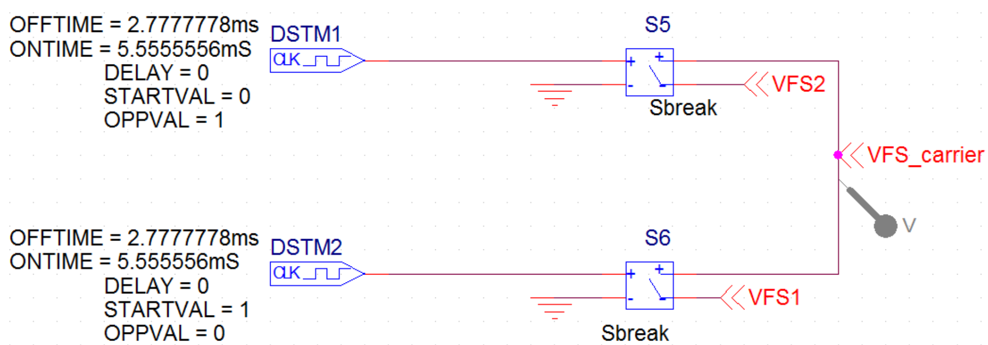

Figure 5.4: The Real Model Carriers Generator

5.1.2.3 Comparator The comparator's function is to generate a binary signal, ones and zeros, by comparing the value of the two inputs. The two inputs are the reference wave and the carrier. In Figure 5.5 the comparator is an operational amplifier "LM324" where it generates +15 volt DC when the positive input (reference) is greater than the negative input (carrier) and -15 Vdc otherwise. A limiter is connected to the OP Amp to set the boundaries between 0 and 1. The gain of the limiter is high enough (1K) to enforce the transition between 0 and 1 in a very short time. In this model there are two comparators, one for leg A and the other one for leg B. The datesheet is included in the appendix.

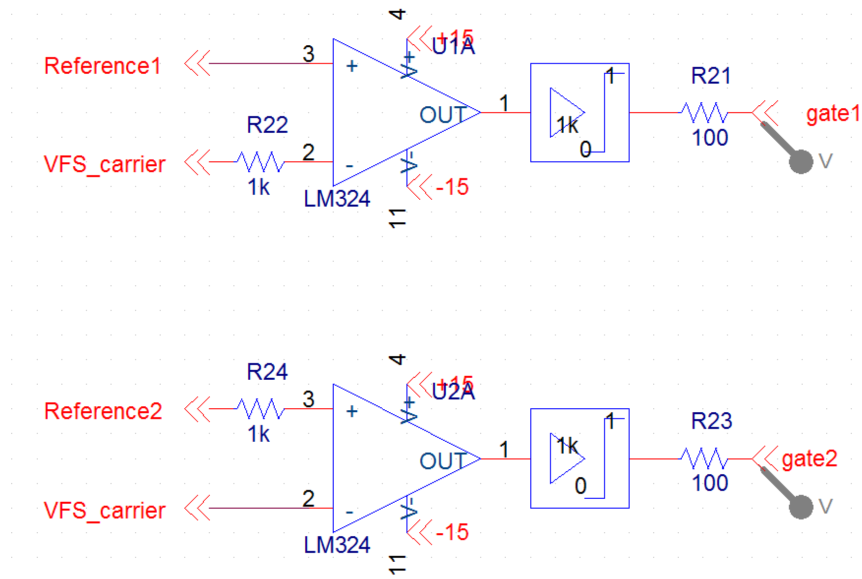

Figure 5.5: The Real Model Comparators

5.2 REAL MODEL COMPARISON RESULTS

One of the major difference between the ideal switching devices and the more realistic ones is that the device does not switches instantly. To turn the switch on the internal capacitance is required to be fully charged to a threshold voltage. The time it takes to reach this charge level is known as the *turn on delay* $t_{d(on)}$. Then it takes some time for the voltage level to keep rising up from the threshold voltage into a full-gate voltage where the switching device operate in a linear manner. In the turn off process, the stored charges need *turn off delay* $t_{d(off)}$ to reach the pinch-off region. Then, the internal capacitance starts discharging to reach the threshold level. This discharge time is known as *fall time* t_f. In this section we are comparing the ideal model fundamental component and WTHD with the real model. We are presenting two examples; the first one has the low switching frequency set at $m_{f_{low}} = 3$ and the high modulation ratio set at $m_{f_{high}} = 9$. For simplification, it is labeled like this $VFSPWM_{9-3}$. While the other example has a high switching frequency equal to $m_{f_{high}} = 15$ and the low frequency is $m_{f_{low}} = 6$, $VFSPWM_{15-6}$.

5.2.1 VFSPWM$_{9-3}$

5.2.1.1 Spectrum Figure 5.6 shows the comparison of the voltage spectrum between the ideal model and the real model when $m_a = 1$. It can be noticed that the real fundamental value is slightly less than the ideal because of the delay time it takes to rise. This difference is not significant. Besides, we can conclude that applying this modulation technique will mimic the simulation to a good extend. To generalize this conclusion, it would be required to present the fundamental component versus a range of modulation index m_a which can be seen in Figure 5.7 in error percentage instead of real values to notice the difference. When the modulation index m_a is small, the width of the pulses is small. Having such narrow pulses will be clearly affected by the delay in the switching. For instance, at $m_a = 0.1$, the difference between the real and ideal fundamental component is 17 %. Fortunately, this difference can be neglected when the modulation index m_a reaches 0.5 where the percentage error is less than 5 %.

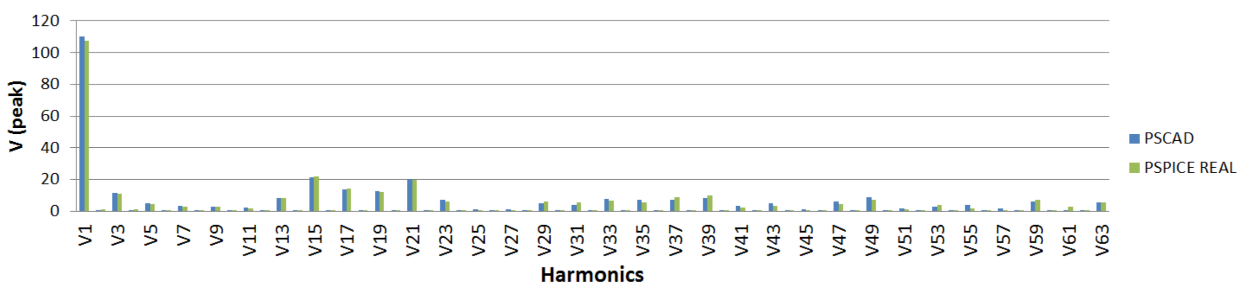

Figure 5.6: The Real Model Spectrum VFSPWM 9-3

5.2.1.2 WTHD We mentioned before that WTHD is one of the important measurement tools. Therefore, it is crucial to compare the WTHD between the real and ideal models. Figure 5.8 shows how the differences between the ideal and real WTHD is decreasing when the modulation index m_a is increasing. The calculated difference can be seen in Figure 5.9. It can be noticed how the percentage error is decreased to a decent level when the modulation index m_a is closing 0.5.

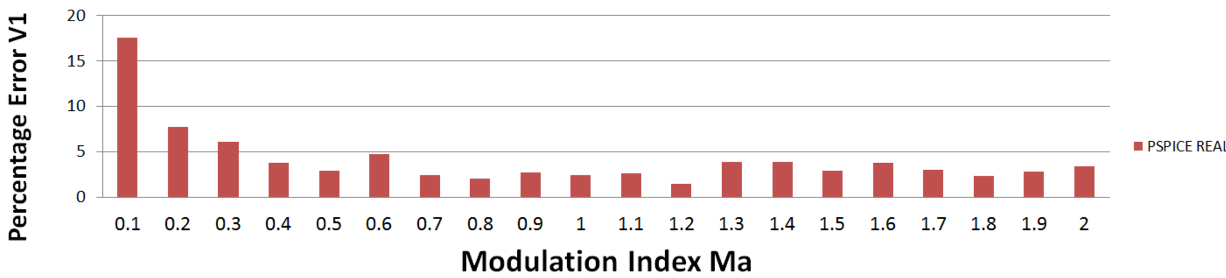

Figure 5.7: V1 Error Percentage of The Real Model VFSPWM (9-3)

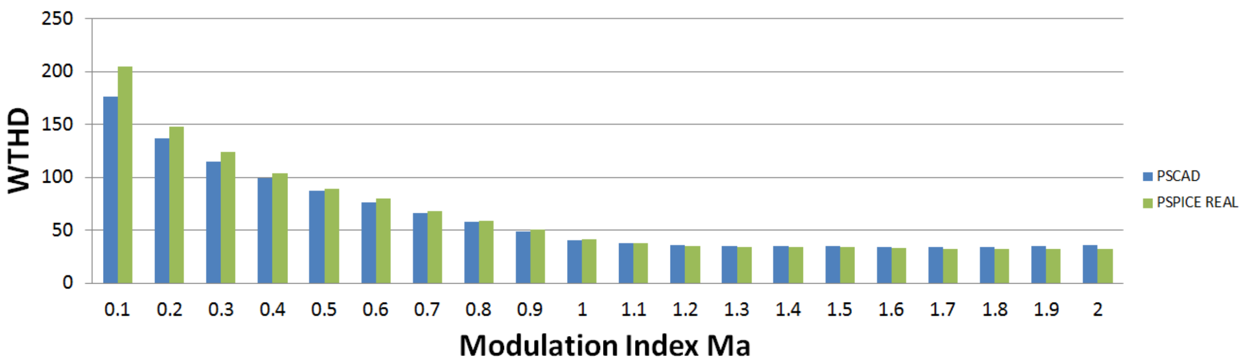

Figure 5.8: WTHD of The Real Model for VFSPWM (9-3)

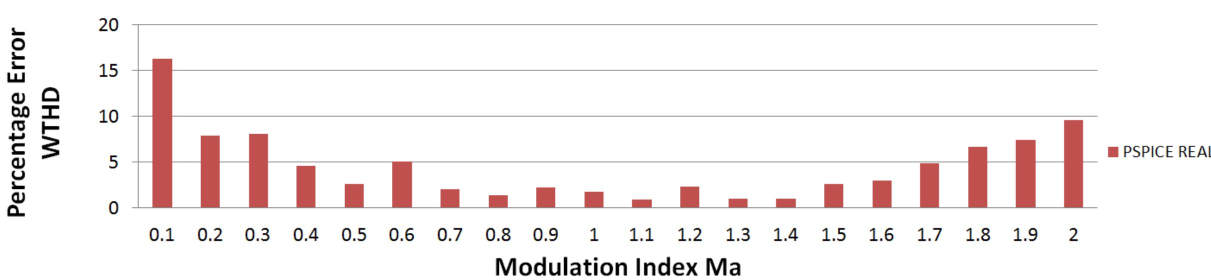

Figure 5.9: Percentage Error of The Real Model WTHD, VFSPWM (9-3)

5.2.2 VFSPWM$_{15-6}$

The second example is to present the comparison of the VFSPWM with two different frequencies, $m_{f_{high}} = 15$ and $m_{f_{low}} = 6$. The purpose of this example is to emphasize on the results of the previous example, $m_{f_{high}} = 15$ and $m_{f_{low}} = 6$.

5.2.2.1 Spectrum In Figure 5.10, the voltage spectrum up to the 63^{rd} harmonics shows that the PSCAD model is almost similar to the real PSPICE model. This result is expected because the pulse in the VFSPWM is wider than the other common modulation techniques making the delay in the switching small in comparison to the width of the pulses. Since the difference between the spectrum of the real and ideal model is small, Figure 5.11 shows the change in the real model by percentage. When $m_a = 0.1$ The error is higher than the previous example, $m_{f_{high}} = 9$ and $m_{f_{low}} = 3$. That is due to the fact that the switching frequency is higher, hence the pulses are narrower and the switching delay has more effects on the width of the pulses.

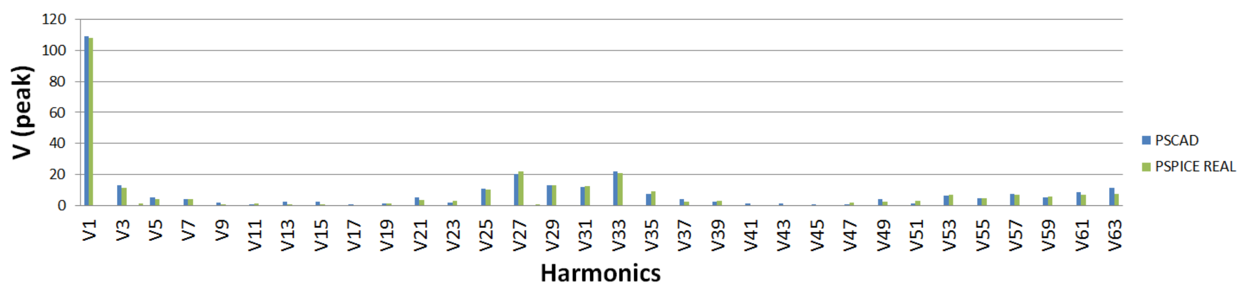

Figure 5.10: The Real Model Spectrum VFSPWM 15-6

5.2.2.2 WTHD The WTHD, when the modulation index m_a is low, has a noticeable difference between the real and ideal models. That can be shown in Figure 5.12. Fortunately, this difference is considered insignificant in the region that is frequently used which is defined between $m_a = 0.6$ and $m_a = 1$. Figure 5.13 depicts that in this range the percentage error is $\leq$ %2. We can conclude that the ideal model is acceptable to evaluate the VFSPWM technique.

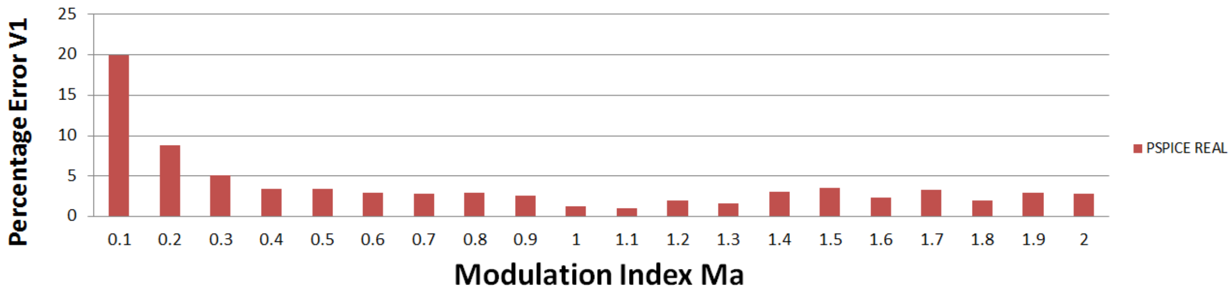

Figure 5.11: V1 Error Percentage of The Real Model VFSPWM (15-6)

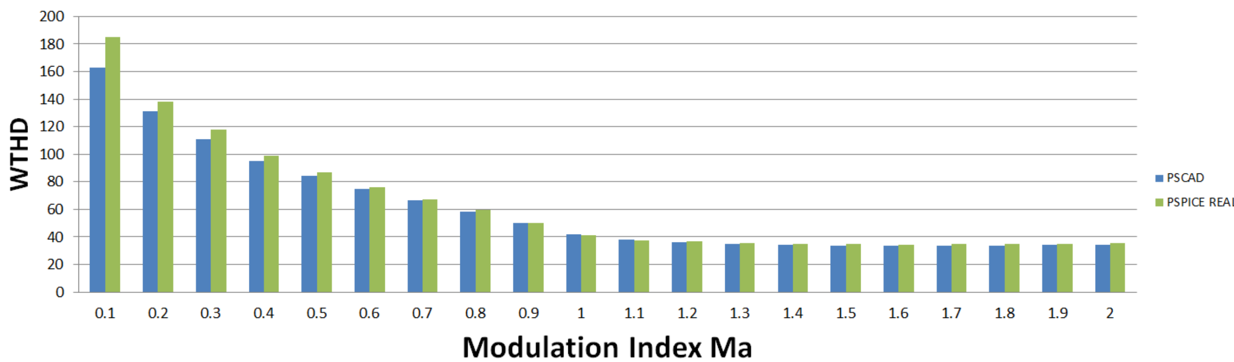

Figure 5.12: The Real Model WTHD for VFSPWM (15-6)

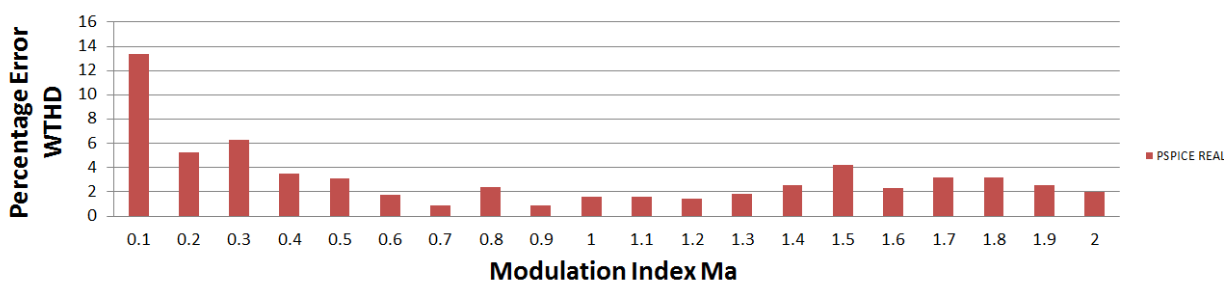

Figure 5.13: Percentage Error of The Real Model WTHD, VFSPWM (15-6)

6.0 HARMONICS ANALYSIS

Inverters are developed and deployed to fix several issues in the power system such as integrating renewable energy, increasing efficiently the capacity of the transmission system, and more. However, inverters and rectifiers are known as harmonic sources. They generate harmonics to a level that may threaten the quality of the power system and harm some of the main equipment like transformers. In this section mathematical equations are presented to calculate the harmonics for the SPWM and VFSPWM. Then, these harmonics are shown graphically to visualize the comparison between the modulation techniques. The comparison is divided into two sub-sections, similar pulses test and similar stress test. The difference between these two tests is explained in details in chapter 4.

6.1 HARMONICS CALCULATION

In this section we are presenting the mathematical equations that are derived previously in section 3.4.1. The harmonics that are analyzed in this section are $5^{th}, 7^{th}, 11^{th}, 13^{th}$ and 17^{th}. These harmonics are expressed mathematically as follows:
The fifth harmonic is calculated as follows:

$$V_{5^{th}} = b_5 \, sin\,(1885t) \tag{6.1}$$

where

$$b_5 = \frac{4V_{dc}}{5\pi}\left[1 + \sum_{k=1}^{m}(-1)^k \, cos(5\alpha_k)\right]$$

The seventh harmonic is calculated as follows:

$$
\begin{aligned}
V_{7^{th}} &= b_7 \, sin \; (2639t) \qquad (6.2) \\
\text{where} & \\
b_7 &= \frac{4V_{dc}}{7\pi}\left[1+\sum_{k=1}^{m}(-1)^k \; cos(7\alpha_k)\right]
\end{aligned}
$$

The eleventh harmonic is calculated as follows:

$$
\begin{aligned}
V_{11^{th}} &= b_{11} \, sin \; (4147t) \qquad (6.3) \\
\text{where} & \\
b_{11} &= \frac{4V_{dc}}{11\pi}\left[1+\sum_{k=1}^{m}(-1)^k \; cos(11\alpha_k)\right]
\end{aligned}
$$

The fifth harmonic is calculated as follows:

$$
\begin{aligned}
V_{13^{th}} &= b_{13} \, sin \; (4901t) \qquad (6.4) \\
\text{where} & \\
b_{13} &= \frac{4V_{dc}}{13\pi}\left[1+\sum_{k=1}^{m}(-1)^k \; cos(13\alpha_k)\right]
\end{aligned}
$$

The fifth harmonic is calculated as follows:

$$
\begin{aligned}
V_{17^{th}} &= b_{17} \, sin \; (6409t) \qquad (6.5) \\
\text{where} & \\
b_{17} &= \frac{4V_{dc}}{17\pi}\left[1+\sum_{k=1}^{m}(-1)^k \; cos(17\alpha_k)\right]
\end{aligned}
$$

where $\alpha_1 < \alpha_2 < \alpha_3 < \cdots < \frac{\pi}{2}$. These angels are calculated using the MATLAB code in section 3.4.1.1 for the SPWM technique and from section 3.4.1.2 for the VFSPWM technique.

6.2 COMPARISON

The comparison between the different modulation techniques should follow an acceptable methodology. The challenging this this comparison is that the SPWM, the benchmark technique, is operating at one switching frequency while the VFSPWM works on two combined switching frequencies. Therefore, the comparison is divided into two cases. The first one compares the techniques that have the same number of pulses per cycle, we call it *similar pulses* test. The second one compares the modulation techniques that have the share the same switching stress, noted *similar stress* test.

6.2.1 Similar Pulses

Since the SPWM technique is the reference, it is preferred to analyze it first and then analyze the other VFSPWM techniques. The modulation ratio m_f that has been chosen arbitrary is 12. The corresponding VFSPWM techniques to this ratio are: (7-4), (8-2) and (9-0).

6.2.1.1 SPWM Figure 6.1a shows the fundamental component and the harmonics of the SPWM. While Figure 6.1b shows the harmonics in percentage of the fundamental. The 11^{th} and the 13^{th} harmonics are conserving the highest energy among the other harmonics because they are the sideband of the modulation ratio, $m_f = 12$. These harmonics start as high as the fundamental components then increase slowly until the modulation index, m_a, is 0.6 where they reach the maximum value which is 75% of the fundamental component. When the modulation index m_a is greater that 0.6, both the $11^{th}$the 13^{th} harmonics are decreasing and the the 7^{th} starts substituting the losing energy in the the two harmonics. At $m_a = 0.9$, the 5^{th} harmonic is slightly increasing.

6.2.1.2 VFSPWM$_{7-4}$ In the VFSPWM techniques, the carrier is composed of two modulation ratio, $M_{f_{high}}$ and $M_{f_{low}}$. The harmonics usually gain high values when there order is close to the modulation ratio. When the modulation ratios are 7 and 4, it is expected to observe an increase in the 4^{th}, 7^{th} harmonics and there multiples and there sidebands. In

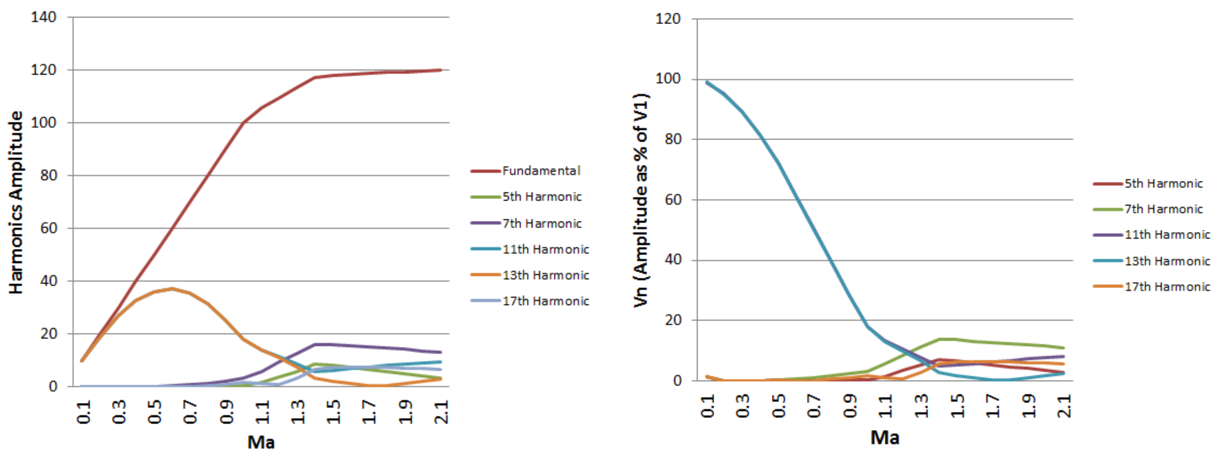

(a) SPWM Harmonics

(b) SPWM Harmonics (% of the fundamental)

Figure 6.1: SPWM Harmonics Analysis

Figure 6.2a, the energy of the harmonics is shared between several orders instead of one, the 13^{th}, as in the SPWM. For low modulation index m_a, all the harmonics are greater that 15%, Figure 6.2b. Fortunately, in the operating region, $m_a \geq 0.6$, the highest is the 11^{th} harmonic having %40 of the fundamental.

6.2.1.3 VFSPWM$_{8-2}$ This configuration of the modulation ratio m_f behaves in the same manner as in the previous technique in terms of the energy distribution. For instance, all the harmonics are sharing the energy generated from the inverter when the modulation index m_a is low. Figure 6.3a shows the amount of energy for each harmonic. In Figure 6.3b it is clear that the harmonics energy is distributed between the 13^{th} and the 17^{th} where both of them are less than 30% of the fundamental. This is considered as a good result because it indicates that the size of the filter should be smaller and more economic.

6.2.1.4 VFSPWM$_{9-0}$ This technique has an advantage over the other VFSPWM technique that it operates at one modulation ratio m_f only, which is 9 in this case. That means

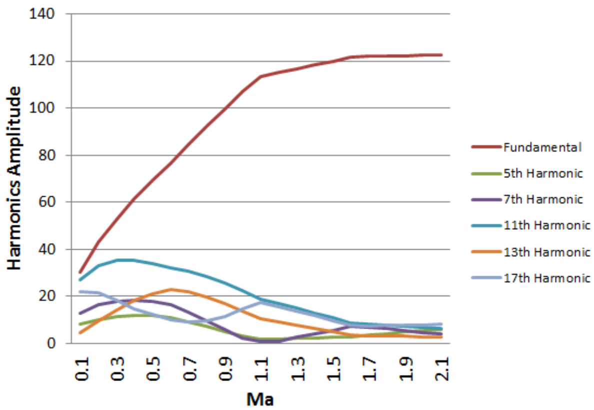

(a) VFSPWM $_{7-4}$ Harmonics

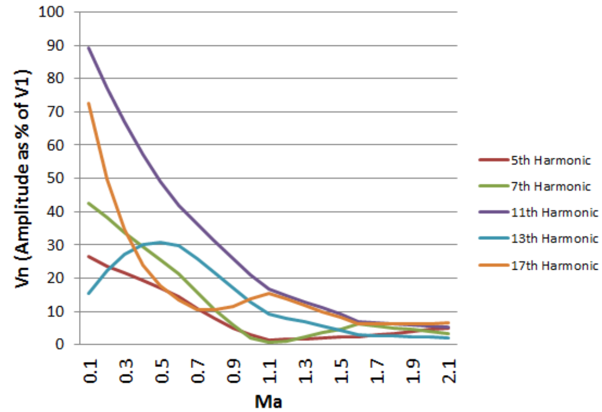

(b) VFSPWM $_{7-4}$ Harmonics (% of the Fund)

Figure 6.2: VFSPWM 7-4 Harmonics Analysis

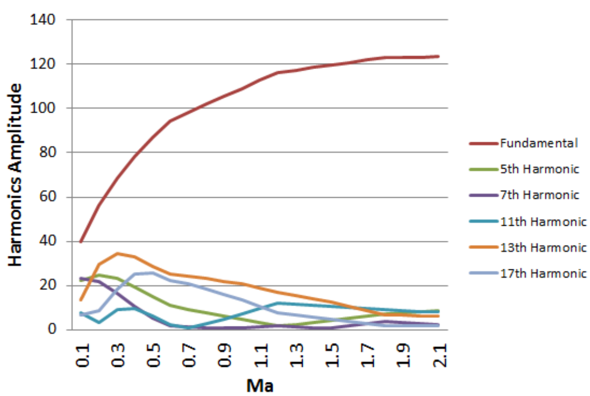

(a) VFSPWM $_{8-2}$ Harmonics

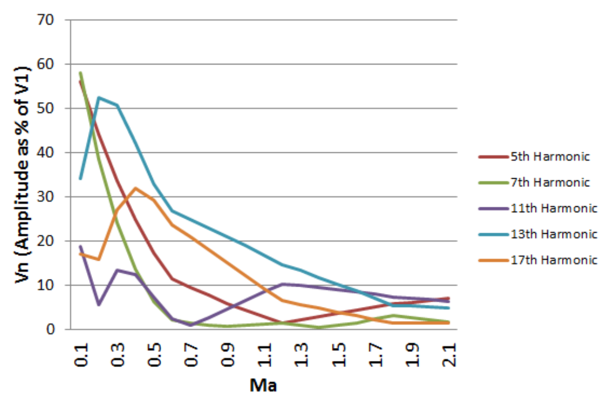

(b) VFSPWM $_{8-2}$ Harmonics (% of the Fund)

Figure 6.3: VFSPWM 8-2 Harmonics Analysis

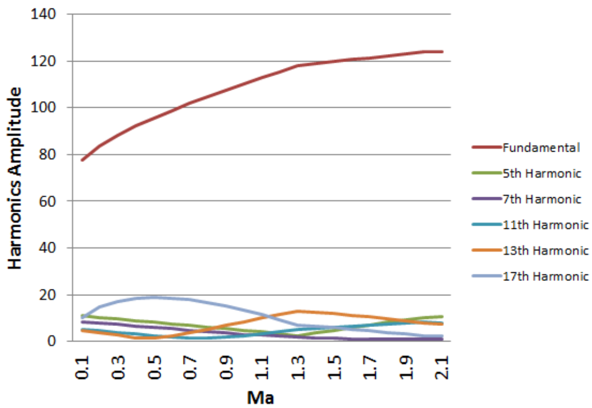

(a) VFSPWM $_{9-0}$ Harmonics

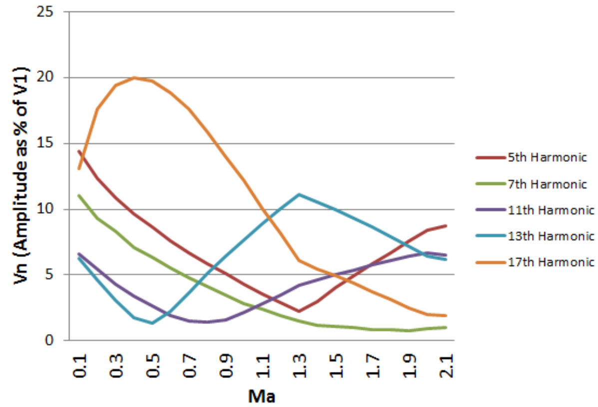

(b) VFSPWM $_{9-0}$ Harmonics (% of the Fund)

Figure 6.4: VFSPWM 9-0 Harmonics Analysis

the utilization of this technique should generate the harmonics in fewer orders in comparison to the other VFSPWM techniques. In Figure 6.4a, the 17^{th} harmonic reserve most of the harmonics energy between $m_a = 0.1$ and $m_a = 1$. Its value is considerably low in comparison to the SPWM technique. In Figure 6.4b, the maximum value of the 17^{th} harmonic is 20% of the fundamental that occurs at $m_a = 0.4$. Therefore, this technique should be preferred because it reduces the harmonics values and shifts the harmonic to a higher order that will lead to smaller and more economic filters.

Figure 6.5 categorizes the harmonics according to their order and shows the results in peak values and percentage to the fundamental component. If we focus on the operation region, $0.6 \leq m_a \leq 1$, it is evident that the highest harmonics occurs at $m_a = 0.6$ for the SPWM. These harmonics are the 11^{th} and The 13^{th}.

6.2.2 Similar Stress

The VFSPWM switching frequencies that maintain the same stress as in the SPWM with a modulation ration m_f equal to 12 is (6-0), (6,3) and (6-6). In this section we are analyzing the 5^{th}, 7^{th}, 11^{th}, 13^{th} and 17^{th} harmonics and then comparing them to the SPWM.

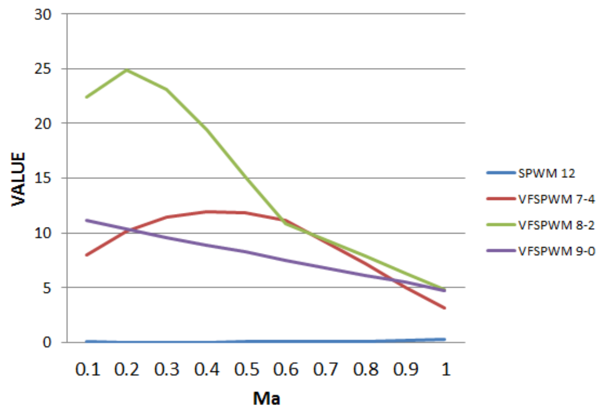

(a) 5^{th} Harmonic (peak value)

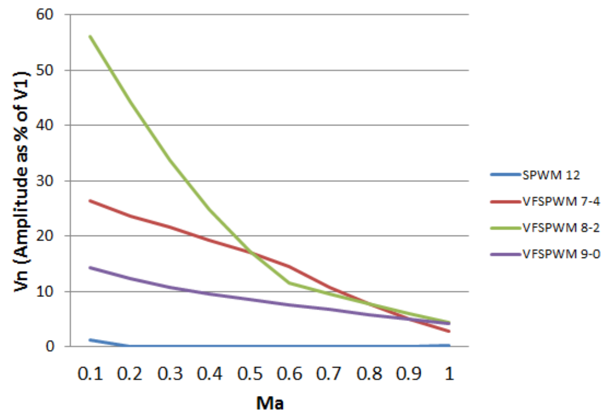

(b) 5^{th} Harmonic (% of the Fund)

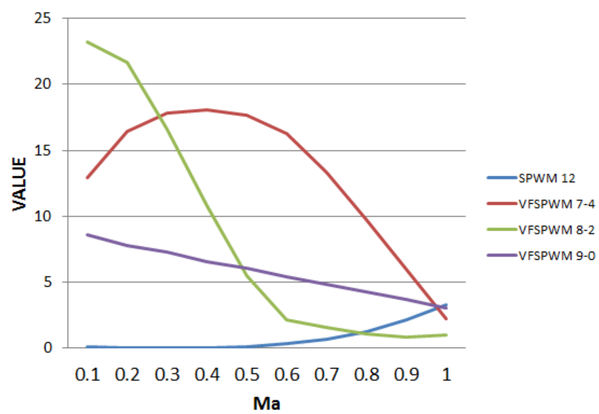

(c) 7^{th} Harmonic (peak value)

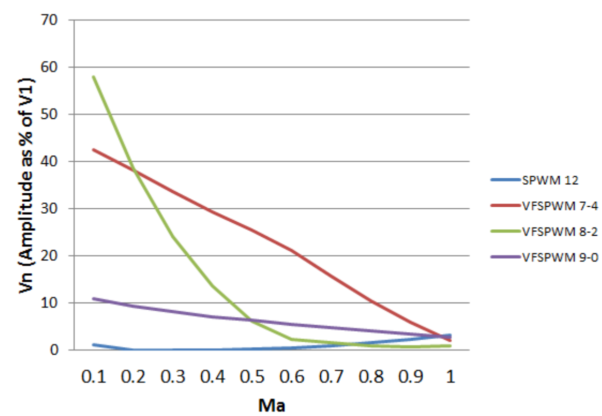

(d) 7^{th} Harmonic (% of the Fund)

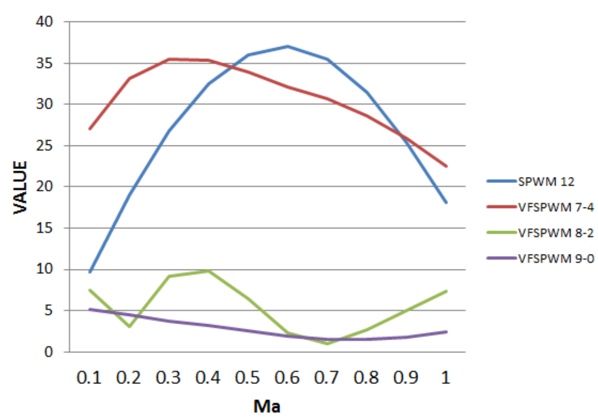

(e) 11^{th} Harmonic (peak value)

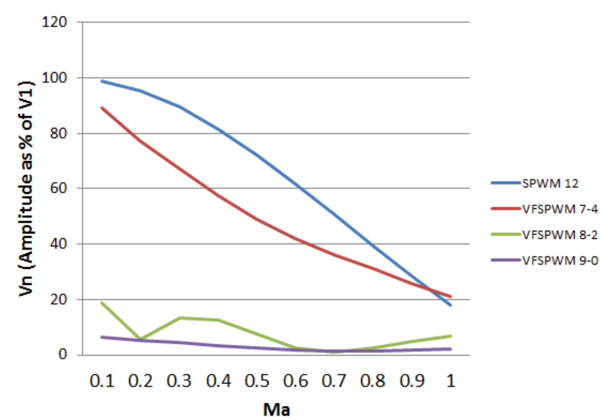

(f) 11^{th} Harmonic (% of the Fund)

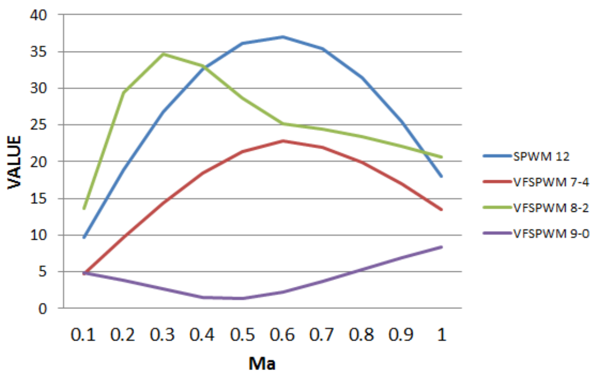

(g) 13^{th} Harmonic (peak value)

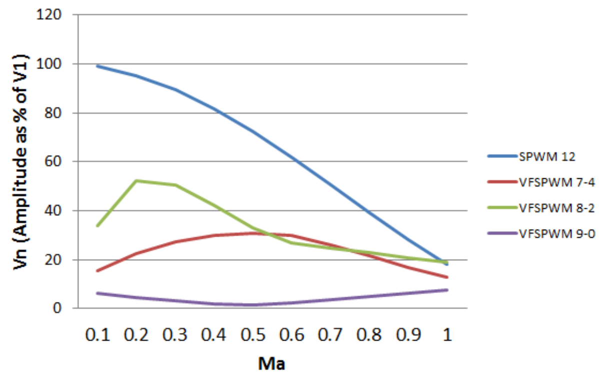

(h) 13^{th} Harmonic (% of the Fund)

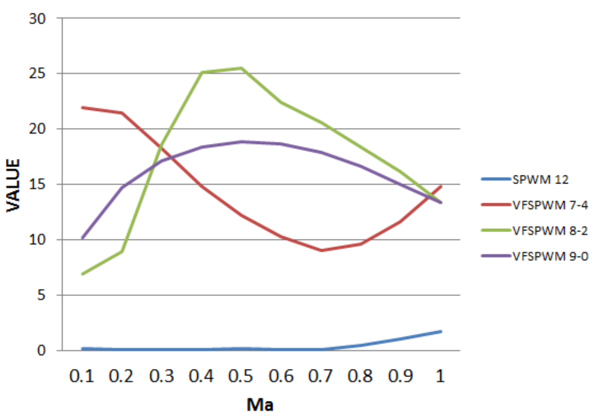

(i) 17^{th} Harmonic (peak value)

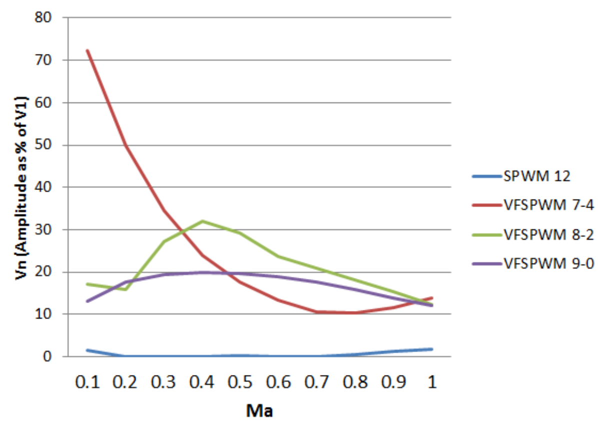

(j) 17^{th} Harmonic (% of the Fund)

Figure 6.5: Harmonics Comparison

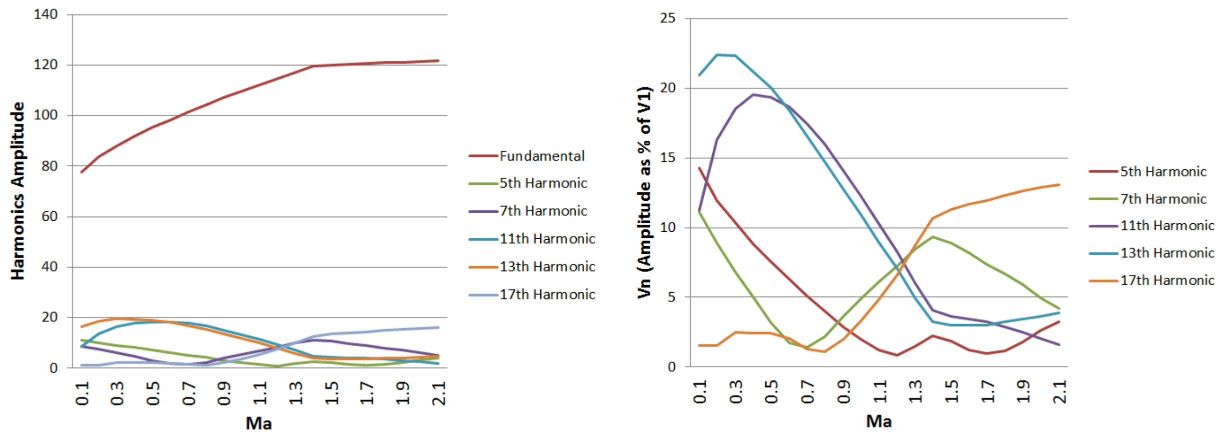

(a) VFSPWM $_{6-0}$ Harmonics

(b) VFSPWM $_{6-0}$ Harmonics (% of the Fund)

Figure 6.6: VFSPWM 6-0 Harmonics Analysis

6.2.2.1 VFSPWM$_{6-0}$ This modulation technique has a feature that it has one switching frequency only. In other words, its harmonics will be a function of one modulation ratio, $m_f = 6$. Therefore, the harmonics that reserve most of the energy, besides the fundamental, are the 11^{th} and the 13^{th}. The fundamental component of this modulation technique starts with high amplitude because the inverter conducts in the middle period of each half cycle. The harmonics amplitude are shown in Figure 6.6a. The maximum summation of these two harmonics is 40% when the modulation index is about 0.4. In the operation range, $0.6 \leq m_a \leq 1$, the other harmonics are at the lowest values where they are less than 10%, Figure 6.6b.

6.2.2.2 VFSPWM$_{6-3}$ The fundamental componenet of the VFSPWM$_{6-3}$ has a steep slop but its low modulation ratio is small enough to put some energy in the 5^{th} and 7^{th} harmonics. It may require larger filters because the order of the harmonics is closer to the fundamental. Besides, the 11^{th} and 13^{th} harmonics get their energy from the high modulation ratio, $m_f = 6$, Figure 6.7a. Still, all the harmonics are less than 20% in the operation region.

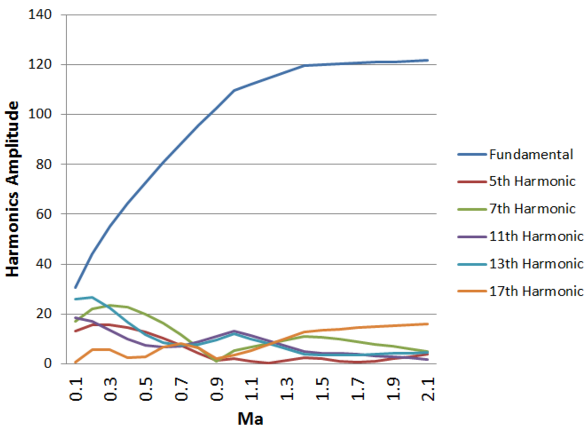

(a) VFSPWM $_{6-3}$ Harmonics

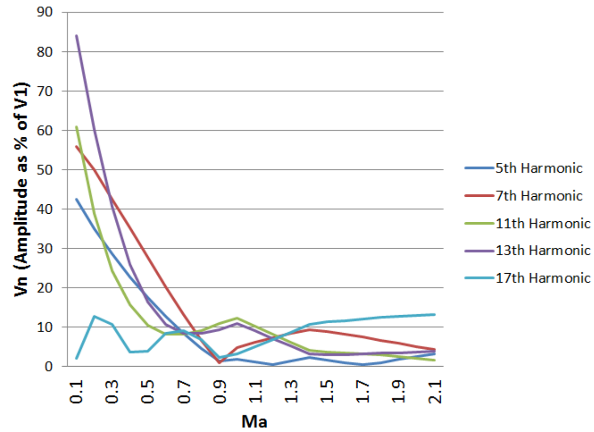

(b) VFSPWM $_{6-3}$ Harmonics (% of the Fund)

Figure 6.7: VFSPWM 6-3 Harmonics Analysis

6.2.2.3 Sinusoidal Inverse Pulse Width Modulation It is worth presenting the modulation technique that the VFSPWM is developed from. It switches at one frequency like the SPWM technique. Figure 6.8a shows how this technique behaves like the SPWM except that its fundamental is higher. The 11^{th} and the 13^{th} are gaining the highest energy, after the fundamental, because of the switching frequency. These two harmonics reserve very high energy that may demand high filters. They conserve about 80% of the fundamental during the operation region, specially when $m_a = 0.6$. Figure 6.8b depicts the energy distribution among the harmonics in percentage of the fundamental.

Figure 6.9 shows the comparison between these modulation techniques and the SPWM. It can be noticed that the 5^{th} and the 7^{th} harmonics are the lowest for the SPWM and the highest, total of 33% at $m_a = 0.6$, when using VFSPWM $_{6-3}$. On the other hand, 11^{th} and the 13^{th} harmonics are very high with the SPWM, total of 125% at $m_a = 0.6$. Where VFSPWM $_{6-0}$ and VFSPWM $_{6-3}$ are the lowest. the 17^{th} harmonic is considered low using any of these techniques.

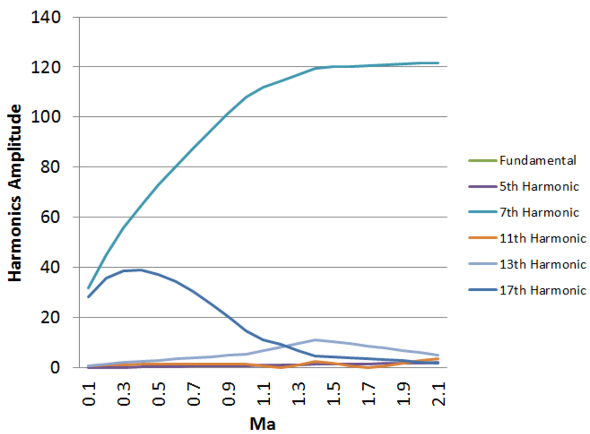

(a) Sinusoidal Inverse PWM Harmonics

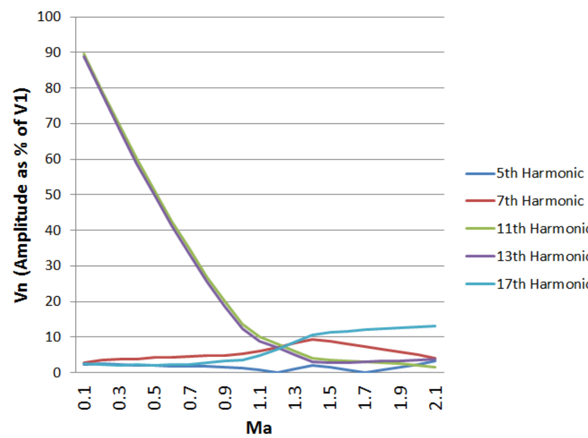

(b) Sinusoidal Inverse PWM Harmonics (% of the Fund)

Figure 6.8: VFSPWM 6-6 Harmonics Analysis

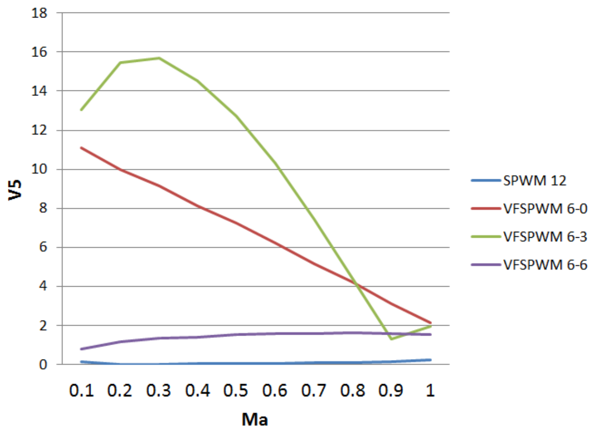

(a) 5^{th} Harmonic (peak value)

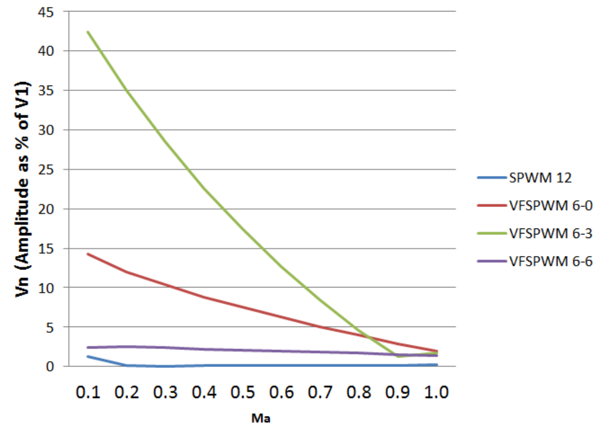

(b) 5^{th} Harmonic (% of the Fund)

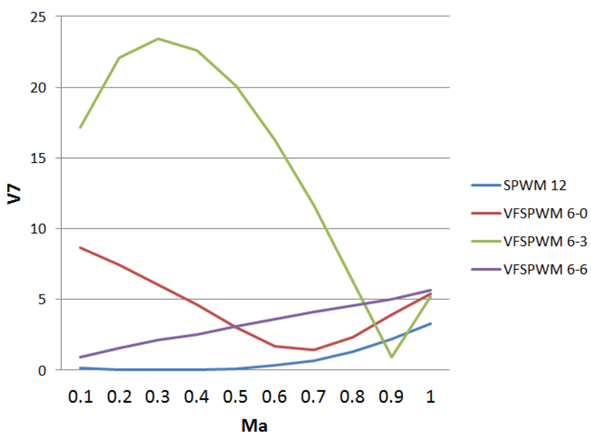

(c) 7^{th} Harmonic (peak value)

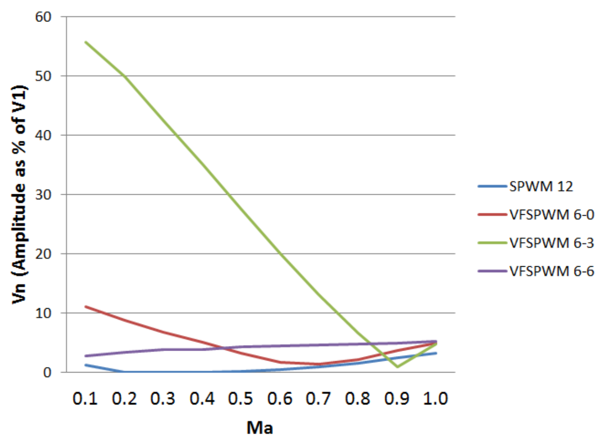

(d) 7^{th} Harmonic (% of the Fund)

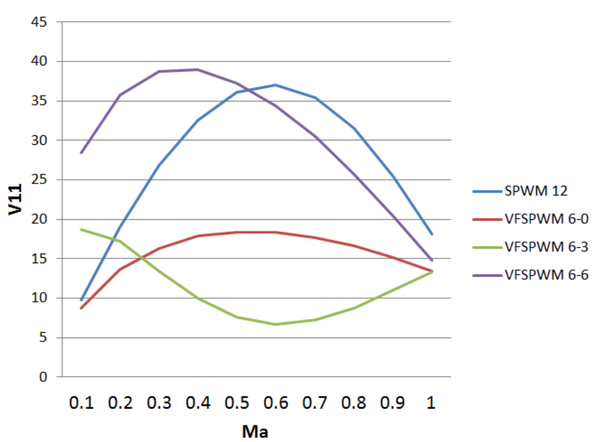

(e) 11^{th} Harmonic (peak value)

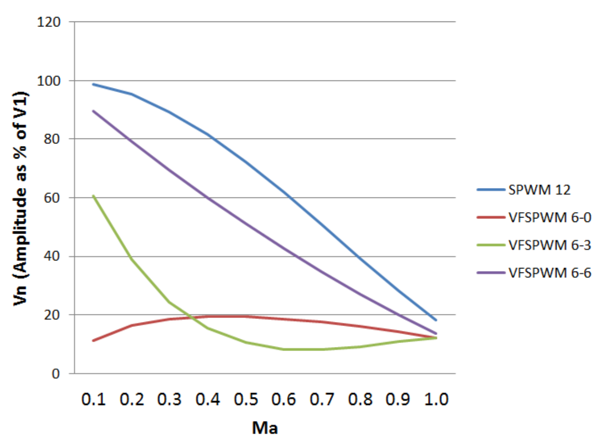

(f) 11^{th} Harmonic (% of the Fund)

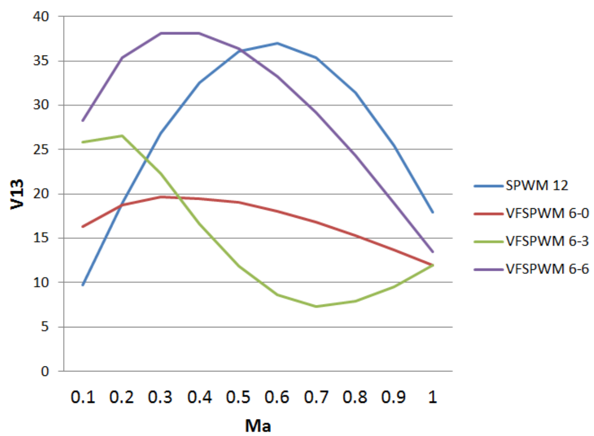

(g) 13^{th} Harmonic (peak value)

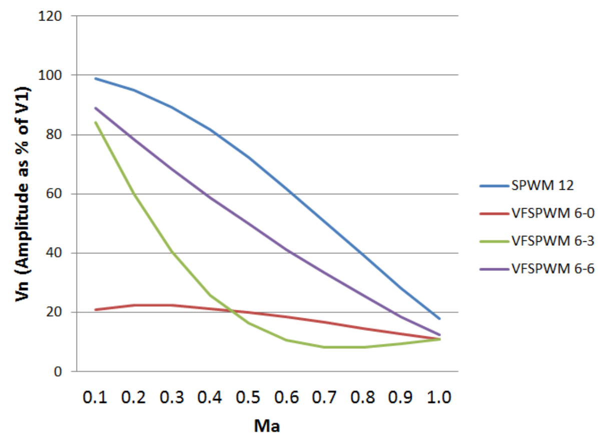

(h) 13^{th} Harmonic (% of the Fund)

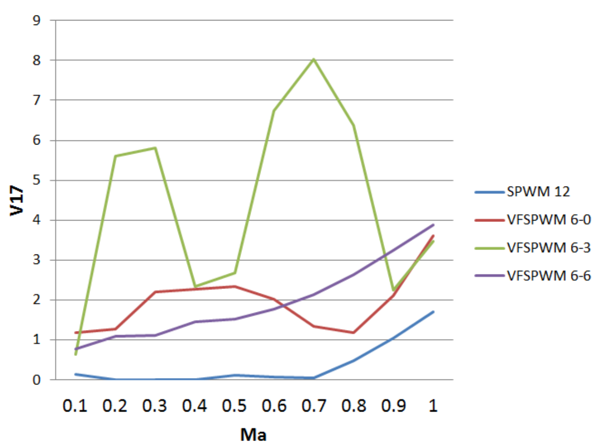

(i) 17^{th} Harmonic (peak value)

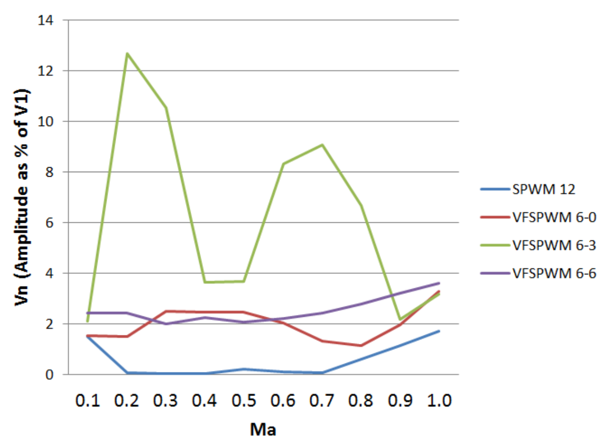

(j) 17^{th} Harmonic (% of the Fund)

Figure 6.9: Harmonics Comparison

7.0 THREE-PHASE VFSPWM

In the previous chapters, the VFSPWM techniques have been tested and analyzed for one phase. We are analyzing the performance of this new modulation technique for three-phase. This chapter starts by presenting the three-phase PSCAD model. Then the components of the three-phase VFSPWM controller are explained. Then, the fundamental component and the THD of the three-phase VFSPWM is analyzed and compered to the SPWM technique. The three-phase VFSPWM waves along with the gating signal are shown in Figure 7.1. Figure 7.2 shows the output of the three-phase inverter using the VFSPWM technique.

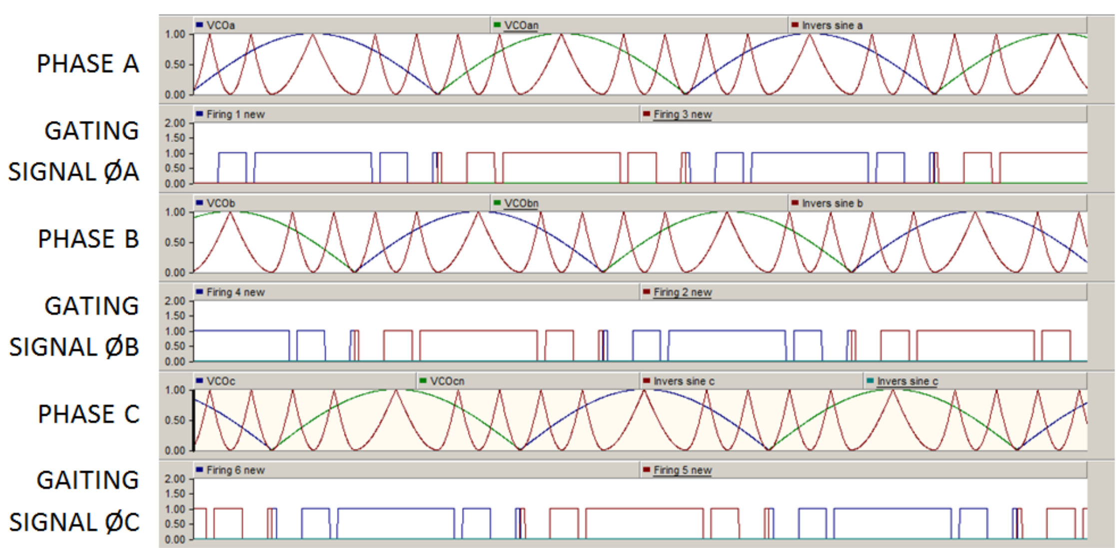

Figure 7.1: Three-Phase VFSPWM Waves and Gating Signals

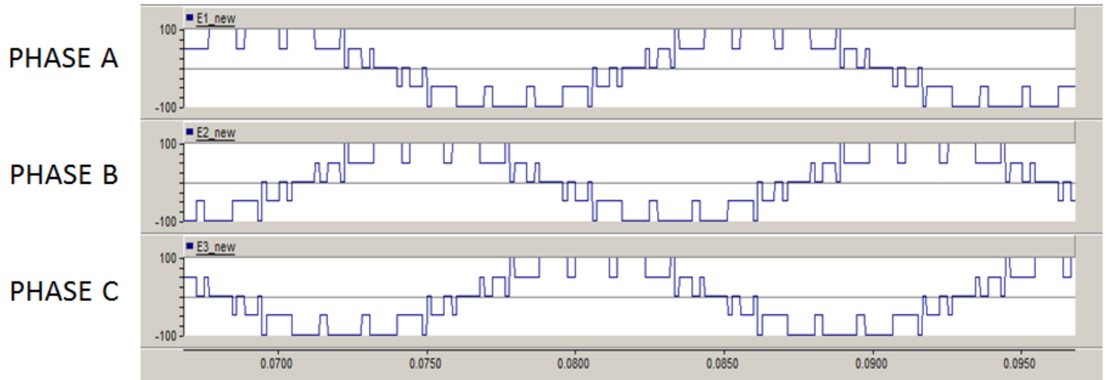

Figure 7.2: Three-Phase VFSPWM Inverter Output

7.1 THREE-PHASE INVERTER

The function of the inverter is to convert the power from DC into AC. This process can be accomplished by using power electronics switches that turn on and off to form a signal that has a desired RMS value. This signal is basically a chain of square waves that should behave similar to the sinusoidal wave on the power equipment. The structure of the three-phase inverter is that it consists of three parallel half-bridge inverters, legs, with one common DC source. Each leg has an upper switch and lower one. When the upper switch is closed "ON" while the lower is "OFF", the leg will be conducting and supplying positive voltage. For simplicity, it is common to refer to the whole leg as positive. On the other hands, when the lower switch is conduction and the upper one is blocking the leg is supplying negative voltage. Figure 7.3 shows the three-phase inverter. The DC capacitance connected in parallel with the DC source is to balance the DC voltage between the upper and lower switches. This is the inverer structure that can be controlled by most of the modulation controllers such as SPWM, Sawtooth modualtion, VFSPWM and more.

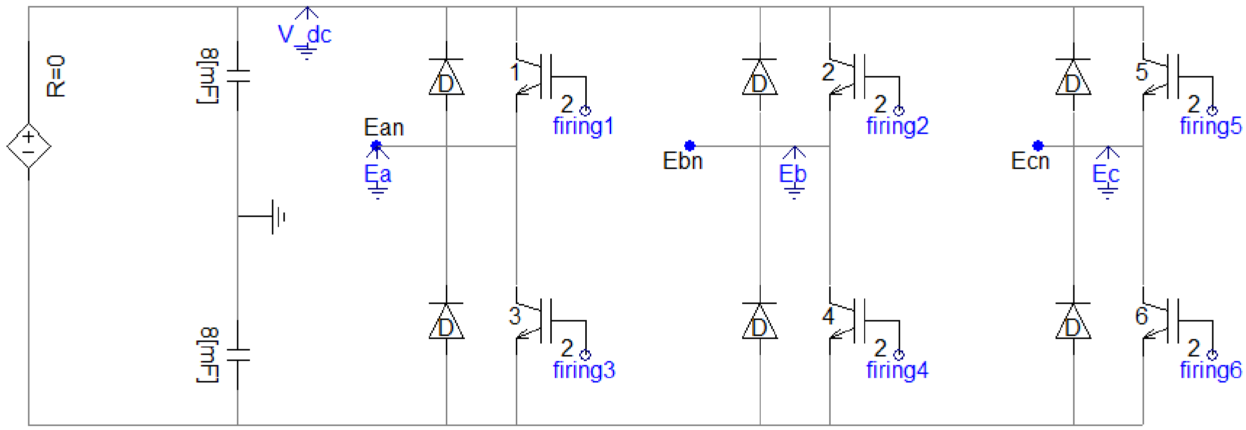

Figure 7.3: Three-Phase Inverter

7.2 THREE-PHASE VFSPWM

In order to get a desired AC signal out of the inverter, a controller has to operate the inverter in a certain pattern. This controller defines the patterns based on two main inputs. The first one is the reference signal and the second one is the carrier. The Three-phase VFSPWM controller is similar to the single phase. It consists of three main components: reference generator, carrier generator and comparators.

7.2.1 Reference generator

This generator is producing two three-phase ideal sinusoidal signals that each should mimic the grid voltage wave (amplitude, frequency and phase). One signal is dedicated for the upper switch and shown in Figure 7.4a. The other one for the lower and shifted by 180° from the first one, Figure 7.4b. The controller's job is to have the inverter RMS output equal to this sinusoidal signal's RMS value. The amplitude of this sinusoidal signal is scaled from zero through 1. Figure 7.4 shows the three-phase reference generator.

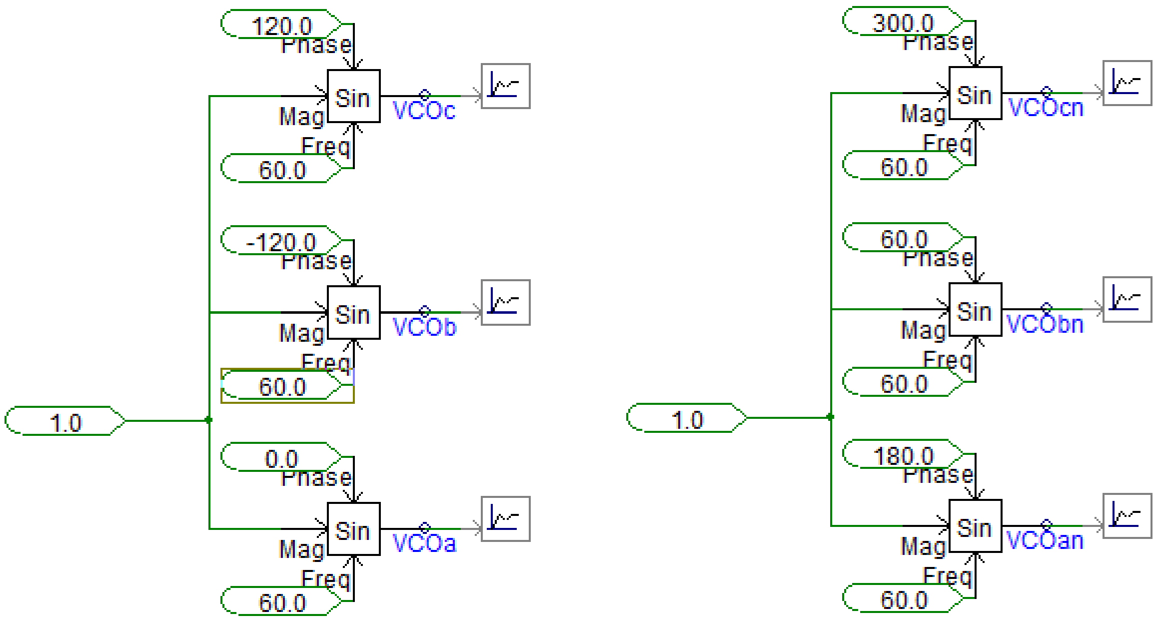

(a) Upper References

(b) Lower References

Figure 7.4: Three-Phase Reference Generators

7.2.2 Carrier generator

The carrier generator is the component that provides a signal that replaces the triangular carrier in the SPWM. The purpose of this carrier is to determine the width of the pulses the inverter is producing. When the frequency of this carrier is high, the pulses will be narrow. Hence, the harmonics that the the inverter generates are having a frequency, and its multiples, of the carrier frequency. That means the filters should be smaller and this is one of the main features in these PWM techniques.

Figure 7.5 shows the carrier generator. This generator consists of an alternator that determines the frequency of the a sinusoidal wave. This alternator switches between two frequencies to keep each one on for 60°. One of them is high and the other one is low. In this example the high is 6 times the fundamental frequency, 60 Hz, and the low is 3 times the fundamental frequency. The sinusoidal signal with the two frequencies is then rectified to have positive sign only. It is then subtracted by 1 and called "*carrier A*" for phase A. Two more signals are generated like carrier A where they have the same amplitude and frequencies. The first one is shifted by 120° and called "*carrier B*" for phase B and the second one is shifted by 240° and called "*carrier C*" for phase C.

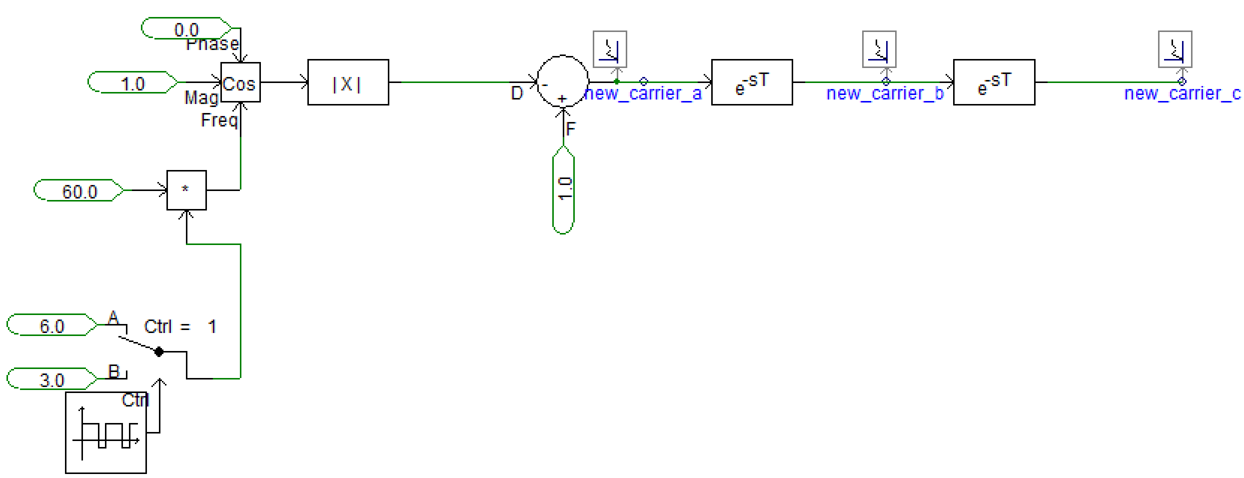

Figure 7.5: Three-Phase Carrier Generator

7.2.3 Comparators

The reference signals and the carrier signals are compared to generate gating signals for the inverter switches. This process is accomplished by the comparator. For the upper switches, the comparator generates a pulse when the value of the reference greater than the carrier. The comparator generates a pulse when the reference is smaller than the carrier for the lower switches. Figure 7.6 shows the comparotrs of the three phases where each phase has two comparators, one for the upper leg and the other one for the lower.

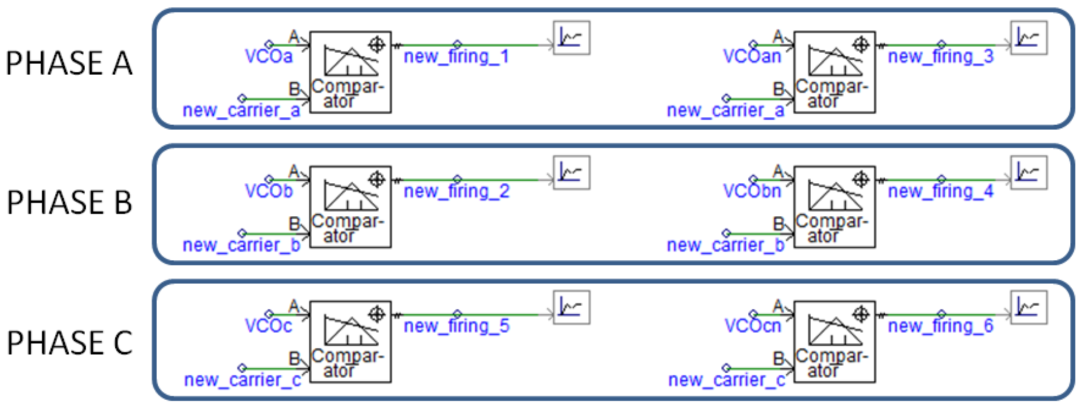

Figure 7.6: Three-Phase Comparators

7.3 THREE-PHASE COMPARISON RESULTS

This comparison is divided into two parts: same pulses and same stress. The two parameters that we are using for the comparison are the fundamental component and the WTHD.

7.3.1 Similar Pulses

Figure 7.7 shows the fundamental component of the SPWM and the VFSPWM configurations, (7-4), (8-2) and (9-0). The three VFSPWM techniques are greater than the SPWM by an average of 40%. VFSPWM$_{9-0}$ maintains the highest fundamental component in the linear region, $0 \leq m_a \leq 1$. Besides, the WTHD is lower for the three VFSPWM techniques, Figure 7.8. This indicates that the the filters are smaller and cheaper.

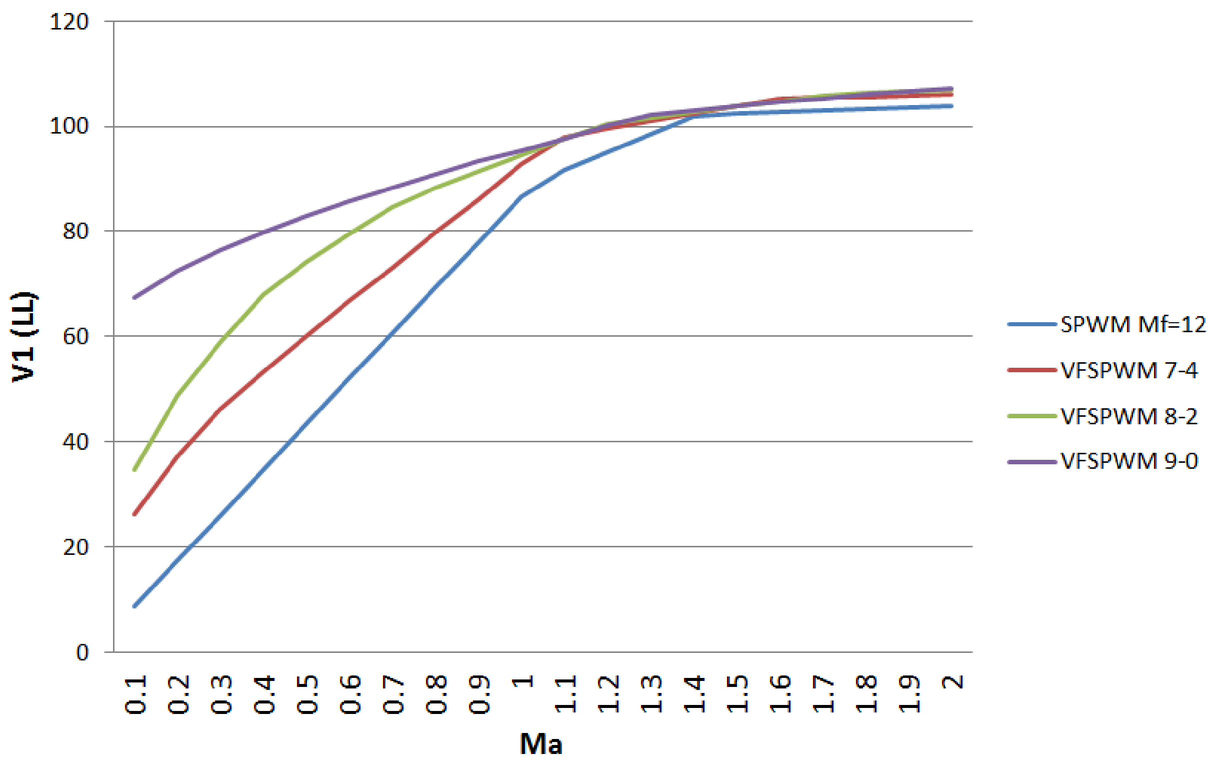

Figure 7.7: Three-Phase Fundamental Component Comparison (Same Pulses)

7.3.2 Similar Stress

The VFSPWM techniques in the similar stress test are more linear than the case of the similar pulses in the linear region. Figure 7.9 shows the comparison of the fundamental component. VFSPWM_{6-0} has the highest V_1 while VFSPWM_{6-3} is almost identical to the original technology that this technique is developed from, simply we called it VFSPWM_{6-6}. SPWM has the lowest V_1 among them. In terms of WTHD, VFSPWM_{6-0} has the lowest distortion. The VFSPWM_{6-3} is out performing the VFSPWM_{6-6} in the WTHD by an average of 32%. Figure 7.10 shows the WTHD comparison.

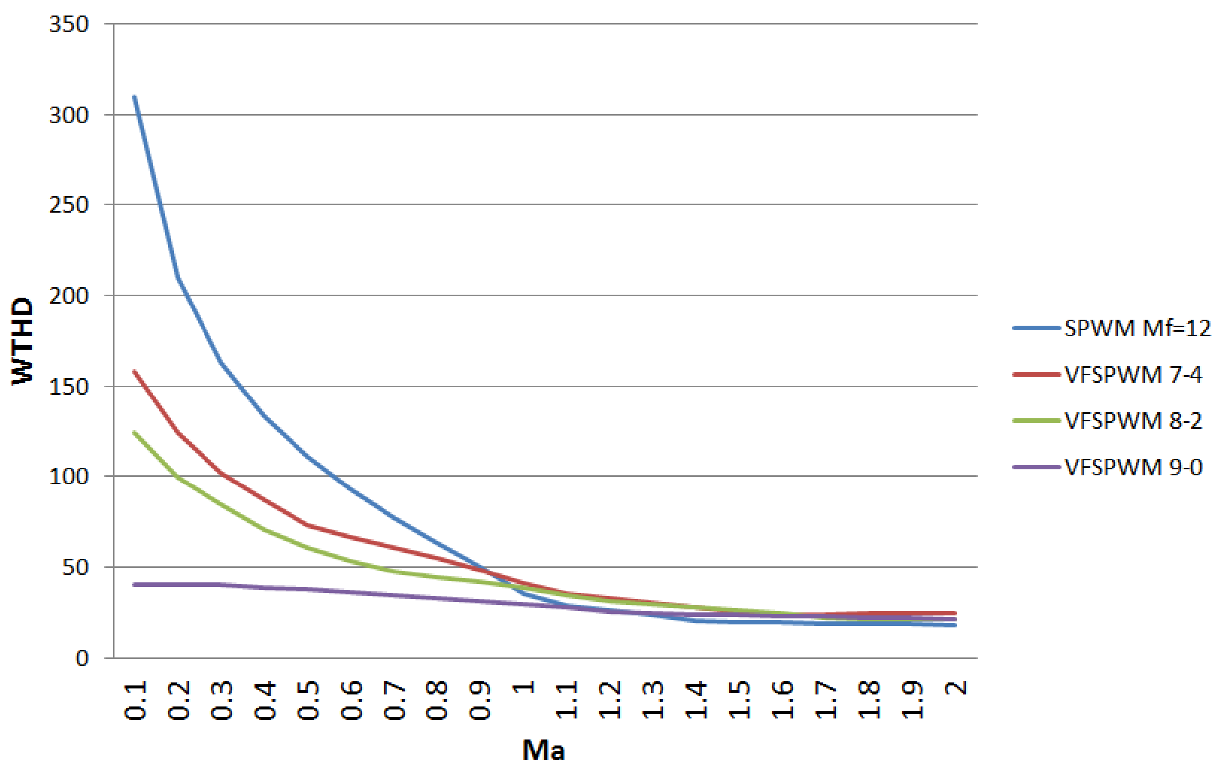

Figure 7.8: Three-Phase WTHD Comparison (Same Pulses)

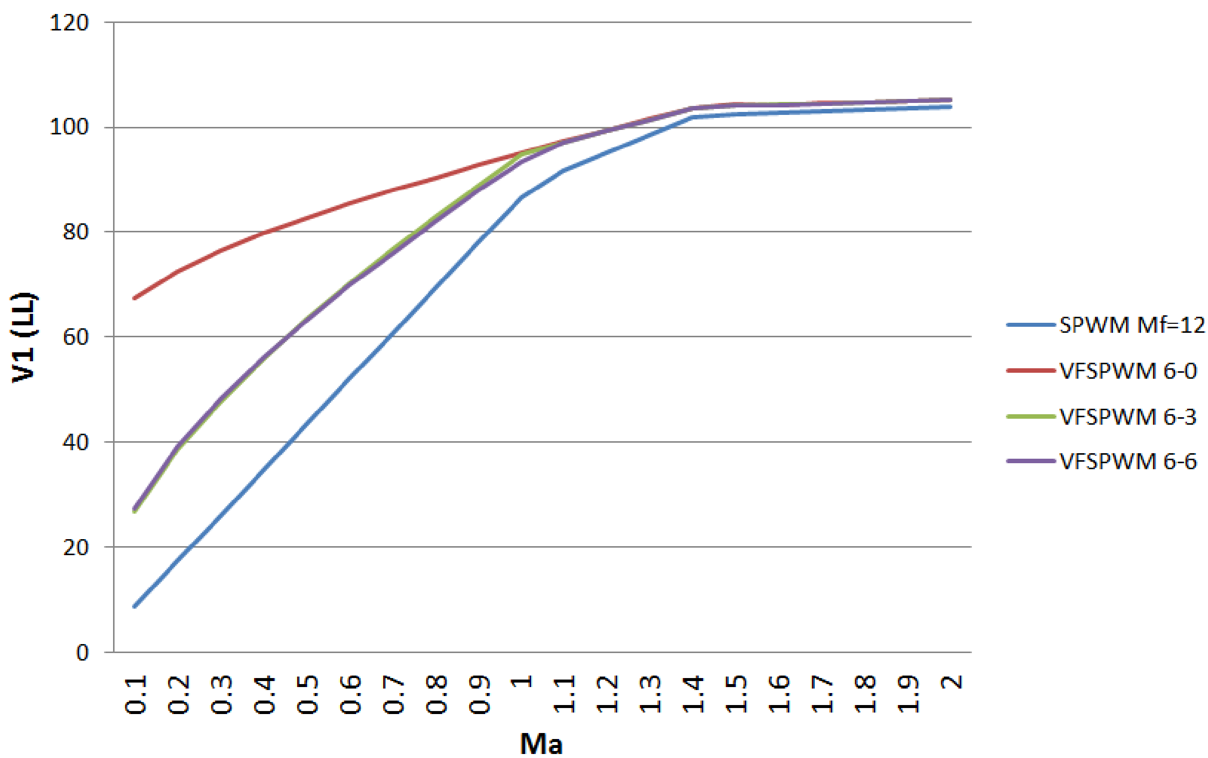

Figure 7.9: Three-Phase Fundamental Component Comparison (Same Stress)

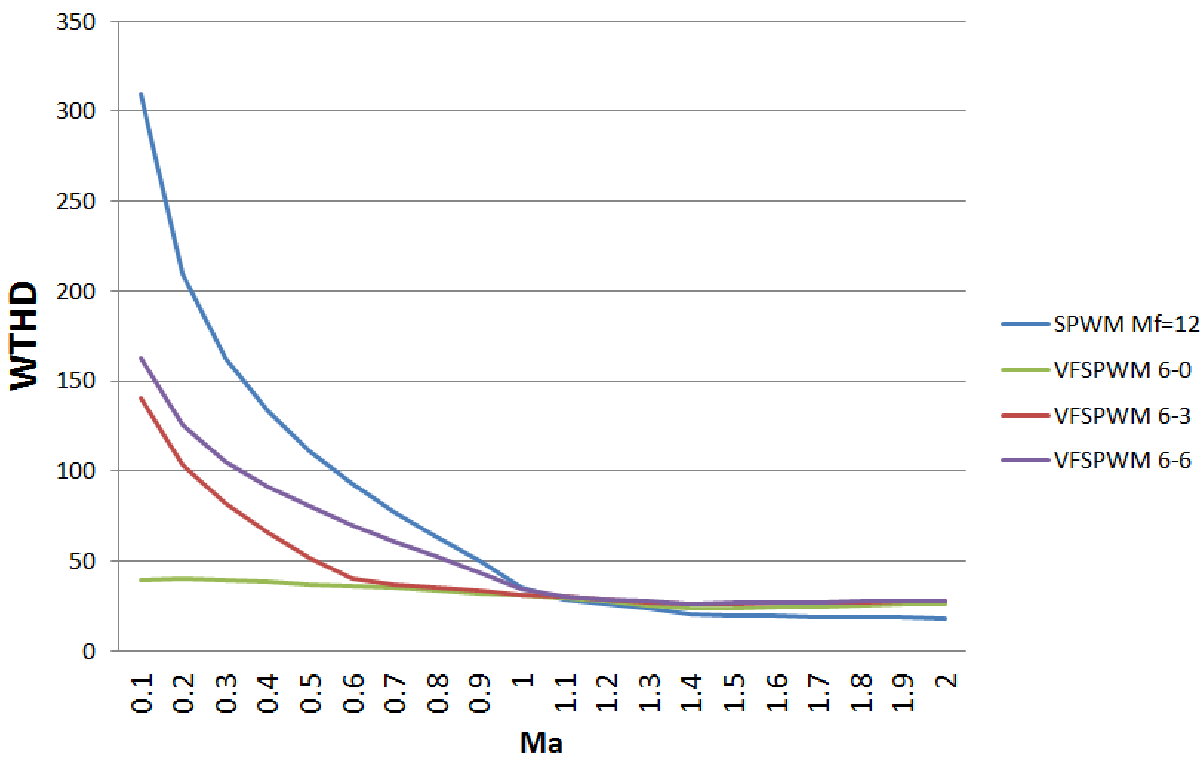

Figure 7.10: Three-Phase WTHD Comparison (Same Stress)

8.0 VFSPWM APPLICATION

In the previous chapters, the analysis of the VFSPWM modulation techniques confirm several major advancements. These techniques increase the fundamental component, reduce the switching losses and decrease the harmonics. In this chapter, we are presenting the benefit of using the VFSPWM technique in Flixible AC Transmission Systems (FACTS) application and compare it to the the SPWM technique. First, A brief introduction on FACTS system is presented. Then, STATCOM, one of FACTS controllers, system is discussed in more details. Finally, a STATCOM model is built as a backbone of the comparison between the VFSPWM and SPWM technique. In this comparison we are using the unipolar technique, hence we are presenting the VFSPWM techniques of the same stress test only.

8.1 FACTS TECHNOLOGY BACKGROUND

The architecture of the power system was built to transfer the power from the generation to the load (distribution system) through the transmission system. This power system is divided into three categories: Radial systems, inter-connected areas and complex network. The use of the transmission system must maintain the adequacy and the security of the system. Unfortunately, This transmission system has steady-state limits such as angular stability, thermal and voltage limits. Besides, the transmission system is constrained by several stability conditions influenced by transient, dynamic voltage or sub-synchronous resonance phenomena. These issues can be solved by properly manipulating the system parameters. One of the common methods to control these parameters is by supplying and absorbing reactive power. For example, when the system under heavy load the voltage may fall below the allowed limit. To solve this issue, it is required to supply reactive power to correct the load power factor. This can be achieved by applying the classical method, mechanically switched shunt capacitors (MSC), or engaging FACTS devices. FACTS controllers are used to increase the limits of the existing transmission system and mitigate the risk of the stability issues. It is preferred to use FACTS system over MSC because it has a rapid controllability of the voltage, current, frequency and phase of the power system. The FACTS controller that serve in this case is either Static Var Compensator (SVC) or Static Synchronous Compensator (STATCOM). STATCOM is the technology that we are using to evaluate the performance of the VFSPWM technique. [1, 47–49]

8.2 STATCOM SYSTEM

STATCOM systems consist of a DC source behind a VSC devices that is connected to the grid through a coupling transformer. Figure 8.1 shows the single line diagram of the STATCOM system. The reactive power exchange between the converter and the grid is based on the voltage difference across the coupling transformer that has (X) reactance. In other words, when the voltage at the converter, E_s is greater than the grid voltage, E_t, the reactive current I_q flows from the converter to the grid and the converter is acting as a capacitor and supplies reactive power. On the other hand, when the voltage at the converter, E_s is less than the grid voltage, E_t, the reactive current I_q flows from the grid to the converter to act as an inductance and absorbs reactive power. These two voltages are in phase. The grid voltage E_t increases when it absorbs reactive power and decreases when supplies reactive power. The amount of the reactive power exchanged between the converter and the grid can be calculated using equation (8.1). The exchange in the reactive power is shown in Figure 8.2.

$$Q = \frac{E_t^2 - E_t E_s}{X} \tag{8.1}$$

The converter voltage E_s is controlled by changing the modulation index, m_a for the inverter. Initially, the value of the m_a is chosen to be equal to 0.8, the nominal value. Figure

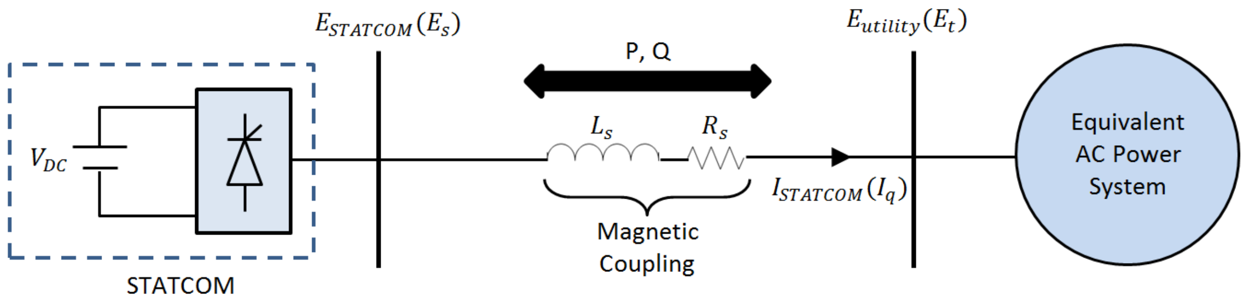

Figure 8.1: STATCOM Single-Line Diagram

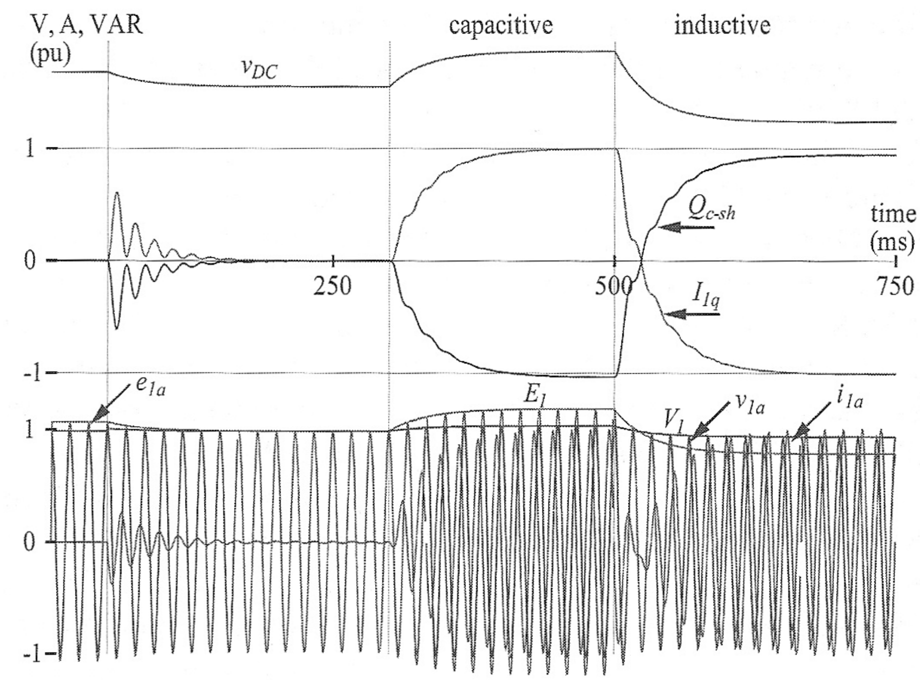

Figure 8.2: STATCOM Reactive Power Exchange [1]

8.3 shows the control of the converter voltage by changing m_a. The operation region is $0.6 \leq m_a \leq 1$. When m_a is equal to 0.8, there is no reactive power exchange between the converter and the grid because the inverter output voltage E_s is equal to the grid voltage E_t. When $m_a \leq 0.8$ the grid is supply reactive power and when $m_a \geq 0.8$ the grid is absorbing reactive power from the converter. [1,47]

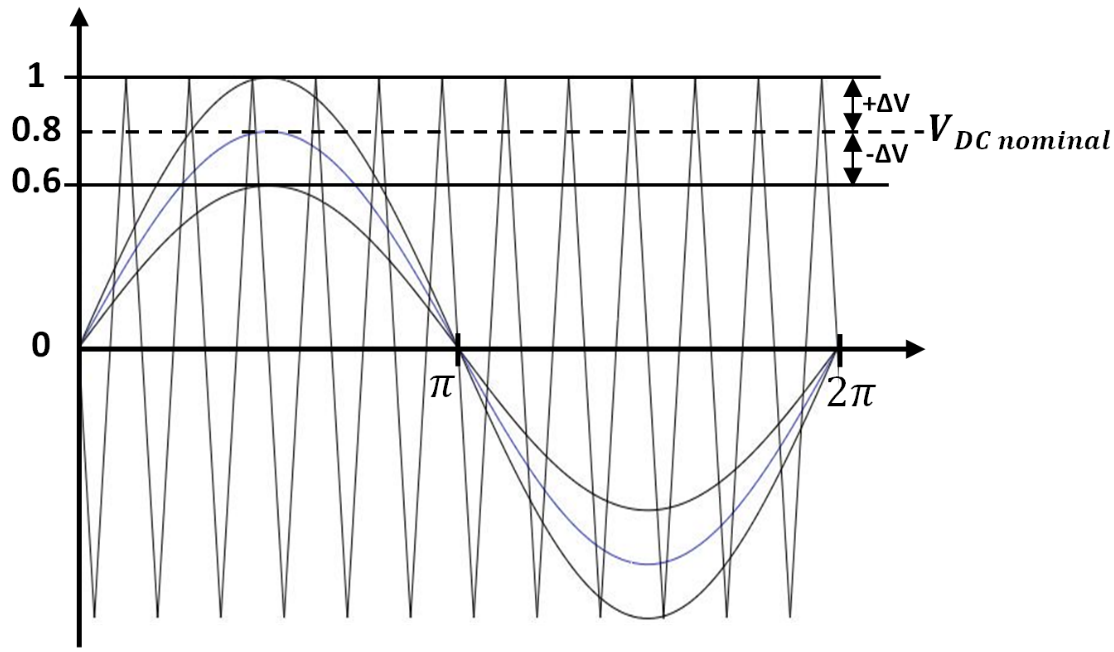

Figure 8.3: STATCOM VSC Output Control

8.3 SYSTEM ANALYSIS

In this section we analyze a network that is simplified to the Thevenin circuit. The PSCAD model of this system is shown in Figure 8.4. The AC Grid is represented by the short-circuit capacity (SSC) and system impedance that is described by the X/R ratio. These parameters can identify the strength of the system. For example, when the X/R ratio is small, the AC system may be called a "*weak system*". Also, when the SSC is low with respect to the actual system capacity, the AC system is weak as well.

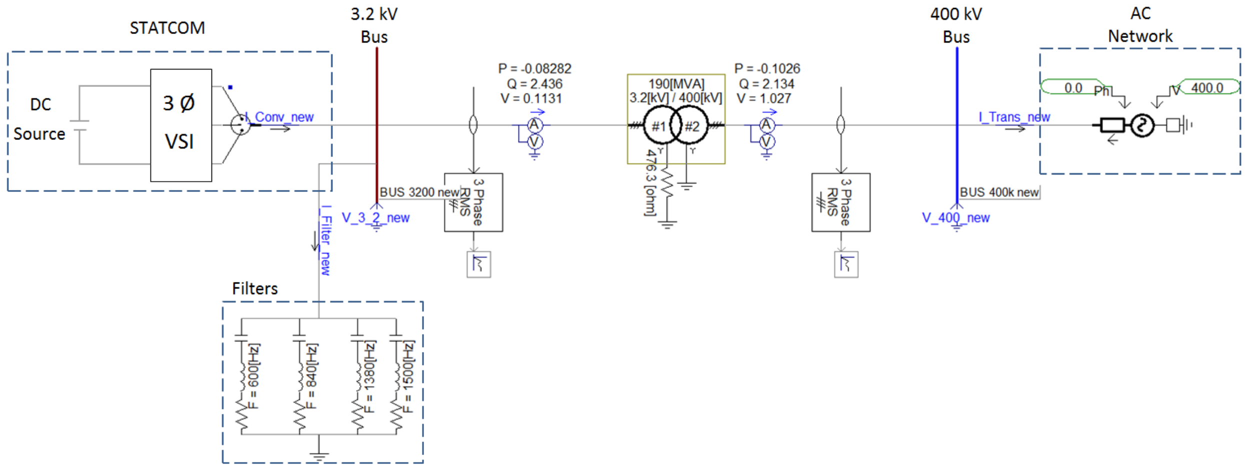

Figure 8.4: PSCAD Model of the STATCOM Application

The purpose of this section is to compare the VFSPWM techniques to the SPWM in the STATCOM application. The major advantage of the VFSPWM is the increase in the fundamental component of the inverter output voltage. In other words, when using the VFSPWM technique on the same system that uses the SPWM technique, the increase in the fundamental component allow using a smaller DC source and the inverter may generate the same nominal voltage. Table 8.1 shows a comparison between the ratings of the DC source. The reduction in the sizing of the DC source is ranging from 5 % to 23.4 %. This reduction introduces a potential savings in the STATCOM projects. The rest of this section presents the design of the filters for each technique. The AC system has the following specifications:

- Power system network
  - Voltage: 400kV
  - Short-circuit level: SCC=10000 MVA, X/R=20.
- Transformer
  - Voltage levels: 400/3.2 kV
  - Rating: 190 MVA
  - Impedance: $Z_T = 0.38 + j11.995\%$
  - Connection: Solidly-grounded Y / Resistance-grounded Y ($R_g = 476.3\Omega$)

Table 8.1: STATCOM DC Source Rating Comparison

	V_{DC} (kV)	DC Source Reduced (% of SPWM)	Ractive Power (MVar)
SPWM	6.53	-	120-120
VFSPWM $_{12-0}$	5	23.4	23-17
VFSPWM $_{12-3}$	6.2	5	147-135
VFSPWM $_{12-6}$	5.6	14.2	71-71
VFSPWM $_{12-9}$	5.7	12.7	80-80

8.3.1 SPWM System Analysis

8.3.1.1 System Impedance The calculation of the system should be in per unit, therefore base values are the first thing that is calculated. The base values at the low-voltage bus are calculated as follows:

$$\begin{aligned} S_{base} &= 100\,MVA \\ V_{baseL} &= 3.2\,kV \\ I_{baseL} &= \frac{100MVA}{(\sqrt{3}*3.2kV)} \\ &= 18.042\,kA \\ Z_{baseL} &= \frac{(3.2kV)^2}{100MVA} \\ &= 0.1024\,\Omega \end{aligned}$$

The base values at the high-voltage bus

$$\begin{aligned} S_{base} &= 100\,MVA \\ V_{baseH} &= 400\,kV \end{aligned}$$

$$
\begin{aligned}
I_{baseH} &= \frac{100MVA}{(\sqrt{3} * 400kV)} \\
&= 144.33\,A \\
Z_{baseH} &= \frac{(400kV)^2}{100MVA} \\
&= 1600\,\Omega
\end{aligned}
$$

- 400 kV equivalent system

$$
\begin{aligned}
SCC &= 10000MVA \\
V &= 400kV \\
Z_{sys} &= \frac{(400kV)^2}{10000MVA} \angle tan^{-1}(20) \\
&= 16\angle 87.14^{\circ}\Omega \\
I_{3\phi SC} &= \frac{(400kV)}{\sqrt{3} * 16\angle 87.14^{\circ}} \\
&= 14.43\angle -87.14kA \\
&= 100\angle -87.14^{\circ} \text{ pu}
\end{aligned}
$$

using $I_{1\phi SC} = 0.9 I_{3\phi SC}$,

$$
\begin{aligned}
I_{1\phi SC} &= I_{3\phi SC} \\
&= 12.99\angle -87.14kA \\
&= 90\angle -87.14^{\circ} \text{ pu} \\
Z^{+} &= \frac{1}{I_{3\phi SC}} \\
&= 0.01\angle -87.14^{\circ} \text{ pu} \\
&= 0.0005 + j0.00999 \text{ pu} \\
Z^{0} &= \frac{3}{I_{1\phi SC}} - 2Z^{+} \\
&= 0.013333\angle 87.14^{\circ} pu \\
&= 0.000666 + j0.013316 \text{ pu} \\
Z_{sys}(h) &= \begin{cases} 0.000666 + j0.013316 * h \text{ pu}, & h = 3n = 3, 6, 9, 12, \ldots \\ 0.0005 + j0.00999 * h \text{ pu} \end{cases} \qquad (8.2)
\end{aligned}
$$

- Transformer

$$
\begin{aligned}
R_g &= \frac{476.3}{0.1024} \\
&= 46.5137 \text{ pu} \\
Z_T^+ = Z_T^- &= \frac{S_{new}}{S_{old}} * Z_T \\
&= \frac{100}{190}(0.0038 + j11.995) \\
&= 0.002 + j0.063132 \text{ pu} \\
Z_T^0 &= Z_T^+ + \frac{3 + R_g}{Z_{baseL}} \\
&= (0.002 + j0.063132) + (3 * 46.5137) \\
&= 139.5411 + j0.063132 \text{ pu} \\
Z_T(h) &= \begin{cases} 139.5411 + j0.063132 * h \text{ pu}, \; h = 3n = 3, 6, 9, 12, \ldots \\ 0.002 + j0.063132 * h \text{ pu} \end{cases}
\end{aligned} \tag{8.3}
$$

- Filters

This has four-branch filters where

Q_{10}= 16 MVar

Q_{14}= 16 MVar

Q_{23}= 16 MVar

Q_{25}= 16 MVar

Therefore, the total is Q_f=64 MVar.

1. Branch 1: $h_n = 10$

$$\begin{aligned}
Q_{C_{10}} &= Q_{10}\frac{h_n^2 - 1}{h_n^2} \\
&= 16(\frac{10^2 - 1}{10^2}) \\
&= 15.84 \text{ MVar} \\
X_{C_{10}} &= \frac{V_{LL}^2}{3 * Q_{C_{10}}} \\
&= \frac{3.2kV^2}{3 * 15.84MVar} \\
&= 0.2155\Omega \\
C_{10} &= \frac{1}{2 * \pi * f * X_{C_{10}}} \\
&= \frac{1}{2 * \pi * 60 * 0.2155} \\
&= 12.31\text{mF} \\
X_{L_{10}} &= \frac{X_{C_{10}}}{h_n^2} \\
&= \frac{0.2155}{10^2} \\
&= 0.002155\Omega \\
L_{10} &= \frac{X_{L_{10}}}{2 * \pi * f} \\
&= \frac{0.002155}{2 * \pi * 60} \\
&= 5.7162\ \mu H \\
X_n &= \sqrt{X_{C_{10}} * X_{L_{10}}} \\
&= \sqrt{0.2155 * 0.002155} \\
&= 0.02155\Omega \\
R_{10} &= \frac{X_n}{Q},\ \text{where } Q = 60 \\
&= \frac{0.02155}{60} \\
&= 0.0003592\Omega \\
Z_{F_1} &= 0.0003592 + j(h * 0.002155 - \frac{0.2155}{h}) \qquad (8.4)
\end{aligned}$$

2. Branch 2: $h_n = 14$

$$
\begin{aligned}
Q_{C_{14}} &= Q_{14}\frac{h_n^2-1}{h_n^2} \\
&= 16(\frac{14^2-1}{14^2}) \\
&= 15.91837 \text{ MVar} \\
X_{C_{14}} &= \frac{V_{LL}^2}{3*Q_{C_{14}}} \\
&= \frac{3.2kV^2}{3*15.91837MVar} \\
&= 0.214427\Omega \\
C_{14} &= \frac{1}{2*\pi*f*X_{C_{14}}} \\
&= \frac{1}{2*\pi*60*0.214427} \\
&= 12.37\text{mF} \\
X_{L_{14}} &= \frac{X_{C_{14}}}{h_n^2} \\
&= \frac{0.214427}{14^2} \\
&= 0.001094\Omega \\
L_{14} &= \frac{X_{L_{14}}}{2*\pi*f} \\
&= \frac{0.001094}{2*\pi*60} \\
&= 2.902\ \mu H \\
X_n &= \sqrt{X_{C_{14}}*X_{L_{14}}} \\
&= \sqrt{0.214427*0.001094} \\
&= 0.015316\Omega \\
R_{14} &= \frac{X_n}{Q},\ \text{where } Q=60 \\
&= \frac{0.015316}{60} \\
&= 0.0002553\Omega \\
Z_{F_2} &= 0.0002553 + j(h*0.001094 - \frac{0.214427}{h}) \qquad (8.5)
\end{aligned}
$$

3. Branch 3: $h_n = 23$

$$\begin{aligned}
Q_{C_{23}} &= Q_{23}\frac{h_n^2-1}{h_n^2} \\
&= 16(\frac{23^2-1}{23^2}) \\
&= 15.9698 \text{ MVar} \\
X_{C_{23}} &= \frac{V_{LL}^2}{3*Q_{C_{23}}} \\
&= \frac{3.2kV^2}{3*15.9698MVar} \\
&= 0.213737\Omega \\
C_{23} &= \frac{1}{2*\pi*f*X_{C_{23}}} \\
&= \frac{1}{2*\pi*60*0.213737} \\
&= 12.41\text{mF} \\
X_{L_{23}} &= \frac{X_{C_{23}}}{h_n^2} \\
&= \frac{0.213737}{23^2} \\
&= 0.000404\Omega \\
L_{23} &= \frac{X_{L_{23}}}{2*\pi*f} \\
&= \frac{0.000404}{2*\pi*60} \\
&= 1.07175\ \mu H \\
X_n &= \sqrt{X_{C_{23}}*X_{L_{23}}} \\
&= \sqrt{0.213737*0.000404} \\
&= 0.00929\Omega \\
R_{23} &= \frac{X_n}{Q},\ \text{where } Q=60 \\
&= \frac{0.00929}{60} \\
&= 0.00015488\Omega \\
Z_{F_3} &= 0.00015488 + j(h*0.000404 - \frac{0.213737}{h}) \qquad (8.6)
\end{aligned}$$

4. Branch 4: $h_n = 25$

$$
\begin{aligned}
Q_{C_{25}} &= Q_{25}\frac{h_n^2 - 1}{h_n^2} \\
&= 16(\frac{25^2 - 1}{25^2}) \\
&= 15.9744 \text{ MVar} \\
X_{C_{25}} &= \frac{V_{LL}^2}{3 * Q_{C_{25}}} \\
&= \frac{3.2kV^2}{3 * 15.9744MVar} \\
&= 0.213675\Omega \\
C_{25} &= \frac{1}{2 * \pi * f * X_{C_{25}}} \\
&= \frac{1}{2 * \pi * 60 * 0.213675} \\
&= 12.414\text{mF} \\
X_{L_{25}} &= \frac{X_{C_{25}}}{h_n^2} \\
&= \frac{0.213675}{25^2} \\
&= 0.000342\Omega \\
L_{25} &= \frac{X_{L_{25}}}{2 * \pi * f} \\
&= \frac{0.000342}{2 * \pi * 60} \\
&= 0.90687\ \mu H \\
X_n &= \sqrt{X_{C_{25}} * X_{L_{25}}} \\
&= \sqrt{0.213675 * 0.000342} \\
&= 0.008547\Omega \\
R_{25} &= \frac{X_n}{Q},\ \text{where } Q = 60 \\
&= \frac{0.008547}{60} \\
&= 0.00014245\Omega \\
Z_{F_4} &= 0.00014245 + j(h * 0.000342 - \frac{0.213675}{h}) \qquad (8.7)
\end{aligned}
$$

The filter impedance is calculated as follows:

$$Z_F = \frac{1}{Z_{baseL}\left(\frac{1}{Z_{F_1}} + \frac{1}{Z_{F_2}} + \frac{1}{Z_{F_3}} + \frac{1}{Z_{F_4}}\right)}$$

Figure 8.5a shows the impedance of the filter. It can be noticed that the filter is acting like a short circuit when the frequency is: 600 Hz, 840 Hz, 1380 Hz and 1500 Hz. The phase of the filter is depicted in Figure 8.5b. The phase is alternating between 90° and -90° at these resonance frequency. The filters supply the system with reactive power at the line frequency, capacitive. Figure 8.5c shows the filter resistance versus the reactance. This figure shows the four points where the filter is almost like a short circuit, very small resistance and zero reactance.

8.3.1.2 Impedance Scan The impedance when we look from the 3.2 kV bus can be calculated as follows:

$$\begin{aligned} Z_{3.2}(h) &= Z_{sys}(h) + Z_T(h) \\ &= (0005 + j0.00999 * h) + (0.002 + j0.063135 * h) \\ &= 0.0025 + j0.073155 * h \text{ pu} \end{aligned} \tag{8.8}$$

Where the impedance of the system when looking for the converter end is as follows:

$$Z_{eq}(h) = \frac{1}{\frac{1}{Z_F(h)} + \frac{1}{Z_{3.2}(h)}} \tag{8.9}$$

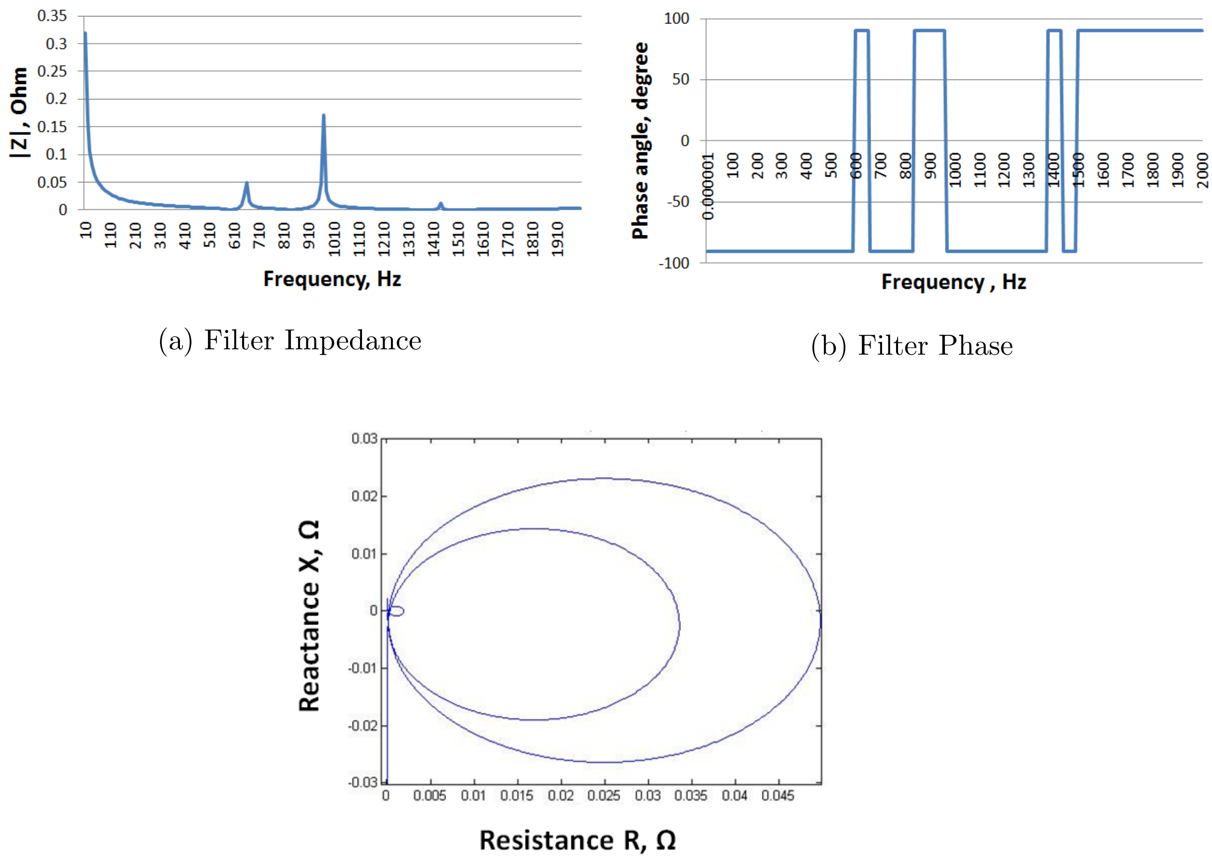

(a) Filter Impedance

(b) Filter Phase

(c) Filter Impedance Locus

Figure 8.5: Filter Impedance and Impedance Locus using SPWM

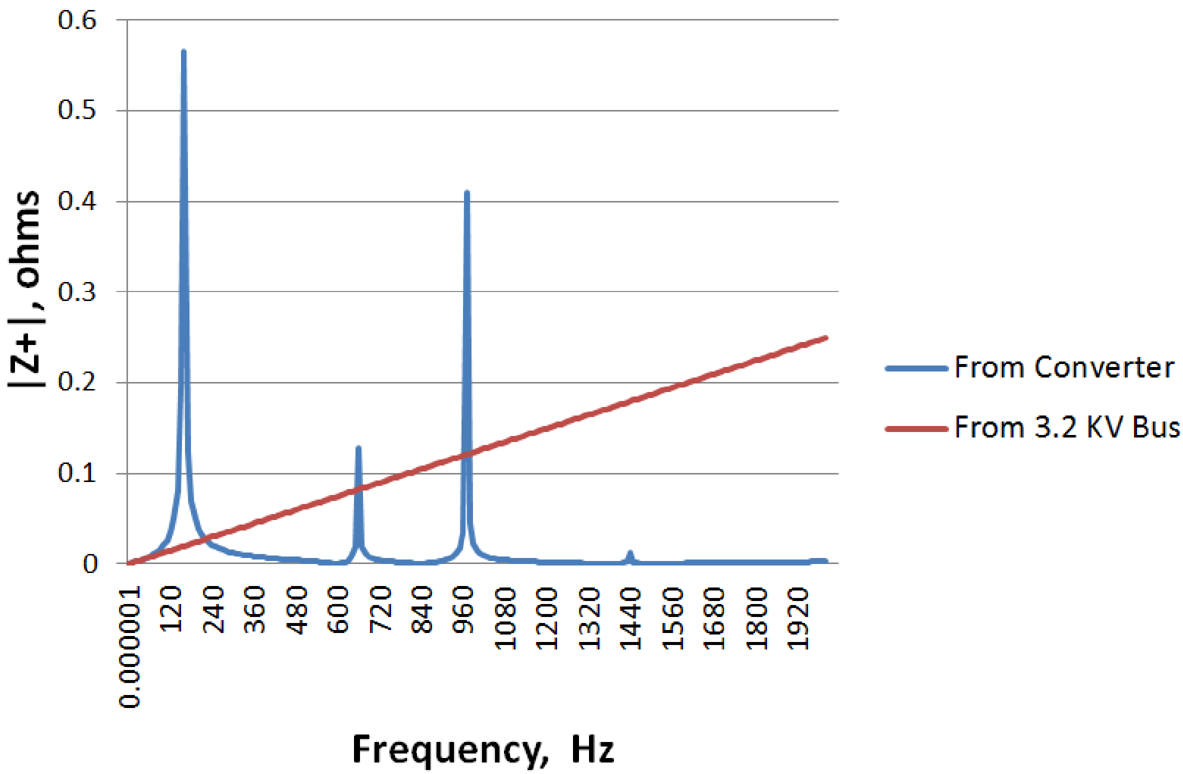

Figure 8.6: System Impedance using SPWM

8.3.1.3 Harmonic Injection

The voltage source harmonics, $V_{3.2}(h)$, is calculated using the equations in section 3.4.1.1. The filter current is calculated usign equation (8.8) :

$$I_F(h) \;=\; \frac{V_{3.2}(h)}{Z_F(h)} \tag{8.10}$$

From equation (8.8), the current that flows through the transformer to the system has the following relationship:

$$I_T(h) \;=\; I_{sys}(h) = \frac{V_{3.2}(h)}{Z_{3.2}(h)} \tag{8.11}$$

Finally the voltage at the 400 kV bus can be calculated as follows:

$$V_{400}(h) \;=\; Z_{sys}(h) * I_{sys}(h) \tag{8.12}$$

The impedance from the 3.2 kV bus, $Z_{3.2}$, and from the converter, Z_{eq}, are plotted in Figure 8.6. The system resonance is at 130 Hz with a value equal to 0.566 Ω. The rest of the resonance are caused by the filter and placed at the harmonic orders they are filtering, 10^{th}, 14^{th}, 23^{rd}, and 25^{th}. Table 8.2 shows the calculated harmonics. These values comply with IEEE 519 harmonic distortion limits:

$$V_h \leq 3\% \text{ and } THD_v \leq 5\% \text{ for } V \leq 69kV$$
$$V_h \leq 1\% \text{ and } THD_v \leq 1.5\% \text{ for } V \geq 161kV \text{ [50]}$$

The transformer is safe because the K-factor is 1.0615 which less than 4. The equation used to calculate the K-factor is:

$$K = \frac{\sum_{h=1}\left(\frac{hI_h}{I_1}\right)^2}{1 + THD_I^2}$$

And the derating factor is

$$D = \frac{1.15}{1 + 1.15K}$$

By using the standard transformer, it can not be loaded more than 99.20%.

Table 8.2: SPWM Harmonic Distortion Results

		3.2 kV bus	Converter Current	Current to Transformer	Current to Filter	400kV bus
THD. %		6.135	238.5	1.659	148.17	0.838
Fundamental	PU	1.08	1.33E-03	0.00173	0.02123	1
h=2	% of Fund.	0.1252	4.868	0.03386	3.024	0.01711
3		0.1463	5.689	0.03958	3.535	0.01999
4		0.1616	6.282	0.04370	3.903	0.02208
5		0.3533	13.734	0.09554	8.533	0.04827
6		0.1200	4.666	0.03246	2.899	0.01640
7		0.2595	10.089	0.07019	6.268	0.03546
8		0.2114	8.217	0.05716	5.105	0.02888
9		0.0628	2.441	0.01698	1.516	0.00858
10		0.6635	25.792	0.17943	16.025	0.09064
11		0.5525	21.477	0.14941	13.344	0.07548
12		5.4791	213.002	1.48177	132.336	0.74856
13		0.2681	10.422	0.07250	6.475	0.03663
14		0.2828	10.992	0.07647	6.829	0.03863
15		0.3016	11.725	0.08156	7.284	0.04120
16		0.2716	10.558	0.07345	6.560	0.03711
17		0.1364	5.304	0.03690	3.295	0.01864
18		0.1378	5.357	0.03727	3.329	0.01883
19		0.5524	21.475	0.14939	13.342	0.07547
20		0.2152	8.364	0.05819	5.197	0.02939
21		1.2273	47.713	0.33192	29.644	0.16768
22		0.5482	21.312	0.14826	13.241	0.07490
23		0.8704	33.838	0.23540	21.023	0.11892
24		0.0432	1.678	0.01167	1.042	0.00590
25		0.8820	34.288	0.23853	21.303	0.12050
26		0.7493	29.131	0.20265	18.099	0.10238
27		0.2028	7.884	0.05485	4.898	0.02771
28		0.5638	21.918	0.15248	13.618	0.07703
29		0.1246	4.842	0.03369	3.009	0.01702
30		1.2102	47.048	0.32729	29.230	0.16534
31		0.3219	12.514	0.08706	7.775	0.04398
K-factor=				1.061505223		
D=				0.992041427		

8.3.2 VFSPWM$_{12-9}$ System Analysis

In this section we are calculating the harmonics at several points in the STATCOM system using the the VFSPWM$_{12-9}$. The calculation is brief because it follows the same procedure that presented in section 8.3.1.

8.3.2.1 System Impedance The system impedance is the same. We are presenting the values here for convenience.

$$\begin{aligned} S_{base} &= 100MVA \\ V_{baseL} &= 3.2kV \\ I_{baseL} &= 18.042kA \\ Z_{baseL} &= 0.1024\Omega \end{aligned}$$

The base values at the high-voltage bus

$$\begin{aligned} S_{base} &= 100MVA \\ V_{baseH} &= 400kV \\ I_{baseH} &= 144.33A \\ Z_{baseH} &= 1600\Omega \end{aligned}$$

- 400 kV equivalent system

$$
\begin{aligned}
SCC &= 10000MVA \\
V &= 400kV \\
Z_{sys} &= 16\angle 87.14°\Omega \\
I_{3\phi SC} &= 100\angle -87.14° \text{ pu}
\end{aligned}
$$

using $I_{1\phi SC} = 0.9 I_{3\phi SC}$,

$$
\begin{aligned}
I_{1\phi SC} &= 90\angle -87.14° \text{ pu} \\
Z^{+} &= 0.0005 + j0.00999 \text{ pu} \\
Z^{0} &= 0.000666 + j0.013316 \text{ pu} \\
Z_{sys}(h) &= \begin{cases} 0.000666 + j0.013316 * h \text{ pu}, \;\; h = 3n = 3, 6, 9, 12, \ldots \\ 0.0005 + j0.00999 * h \text{ pu} \end{cases}
\end{aligned} \tag{8.13}
$$

- Transformer

$$
\begin{aligned}
R_g &= 46.5137 \text{ pu} \\
Z_T^{+} = Z_T^{-} &= 0.002 + j0.063132 \text{ pu} \\
Z_T^{0} &= 139.5411 + j0.063132 \text{ pu} \\
Z_T(h) &= \begin{cases} 139.5411 + j0.063132 * h \text{ pu}, \;\; h = 3n = 3, 6, 9, 12, \ldots \\ 0.002 + j0.063132 * h \text{ pu} \end{cases}
\end{aligned} \tag{8.14}
$$

- Filters

This has five-branch filters where Q_{11}=30 MVar, Q_{13}= 25 MVar, Q_{18}= 10, Q_{24}= 20 MVar and Q_{30}= 10 MVar. Therefore, the total is Q_f=95 MVar.

1. Branch 1: $h_n = 11$

$$\begin{aligned}
Q_{C_{11}} &= 29.752 \text{ MVar} \\
X_{C_{11}} &= 0.11473 \ \Omega \\
C_{11} &= 23.121 \text{ mF} \\
X_{L_{11}} &= 0.000948 \ \Omega \\
L_{11} &= 2.515 \ \mu H \\
X_n &= 0.01043 \ \Omega \\
R_{11} &= 0.00017383 \ \Omega \\
Z_{F_1} &= 0.00017383 + j(h * 0.000948 - \frac{0.11473}{h})
\end{aligned} \tag{8.15}$$

2. Branch 2: $h_n = 13$

$$\begin{aligned}
Q_{C_{13}} &= 24.85207 \text{ MVar} \\
X_{C_{13}} &= 0.137346 \ \Omega \\
C_{13} &= 19.31315 \text{ mF} \\
X_{L_{13}} &= 0.000813 \ \Omega \\
L_{13} &= 2.1557 \ \mu H \\
X_n &= 0.010565 \ \Omega \\
R_{13} &= 0.000176085 \ \Omega \\
Z_{F_2} &= 0.000176085 + j(h * 0.000813 - \frac{0.137346}{h})
\end{aligned} \tag{8.16}$$

3. Branch 3: $h_n = 18$

$$\begin{aligned}
Q_{C_{18}} &= 9.9654 \text{ MVar} \\
X_{C_{18}} &= 0.34252\ \Omega \\
C_{18} &= 7.744 \text{ mF} \\
X_{L_{18}} &= 0.001185\ \Omega \\
L_{18} &= 3.1438\ \mu H \\
X_n &= 0.020148\ \Omega \\
R_{18} &= 0.0003358\ \Omega \\
Z_{F_3} &= 0.0003358 + j(h * 0.001185 - \frac{0.34252}{h})
\end{aligned} \tag{8.17}$$

4. Branch 4: $h_n = 24$

$$\begin{aligned}
Q_{C_{24}} &= 19.96528 \text{ MVar} \\
X_{C_{24}} &= 0.170963\ \Omega \\
C_{24} &= 15.515505 \text{ mF} \\
X_{L_{24}} &= 0.000297\ \Omega \\
L_{24} &= 0.787318\ \mu H \\
X_n &= 0.007123\ \Omega \\
R_{24} &= 0.000118725\ \Omega \\
Z_{F_4} &= 0.000118725 + j(h * 0.000297 - \frac{0.170963}{h})
\end{aligned} \tag{8.18}$$

5. Branch 5: $h_n = 30$

$$
\begin{aligned}
Q_{C_{30}} &= 9.9888 \text{ MVar} \\
X_{C_{30}} &= 0.341713\ \Omega \\
C_{30} &= 7.7626 \text{ mF} \\
X_{L_{30}} &= 0.00038\ \Omega \\
L_{30} &= 1.00714\ \mu H \\
X_n &= 0.01139\ \Omega \\
R_{30} &= 0.000189891\ \Omega \\
Z_{F_5} &= 0.000189891 + j(h * 0.00038 - \frac{0.341713}{h}) \qquad (8.19)
\end{aligned}
$$

The filter impedance is calculated as follows:

$$
Z_F = \frac{1}{Z_{baseL}\left(\frac{1}{Z_{F_1}} + \frac{1}{Z_{F_2}} + \frac{1}{Z_{F_3}} + \frac{1}{Z_{F_4}} + \frac{1}{Z_{F_5}}\right)}
$$

Figure 8.7a shows the impedance of the filter.The filter short circuits the voltagas at 660 Hz, 780 Hz, 1080 Hz, 1440 and 1800 Hz. The phase of the filter is depicted in Figure 8.7b. The phase is alternating between 90° and -90° at these resonance frequency. The filters supply the system with reactive power at the line frequency, capacitive. Figure 8.7c shows the filter resistance versus the reactance. This figure shows the four points where the filter is almost like a short circuit, very small resistance and zero reactance.

8.3.2.2 Impedance Scan The impedance when we look from the 3.2 kV bus can be calculated as follows:

$$
\begin{aligned}
Z_{3.2}(h) &= Z_{sys}(h) + Z_T(h) \\
&= (0005 + j0.00999 * h) + (0.002 + j0.063135 * h) \\
&= 0.0025 + j0.073155 * h \text{ pu} \qquad (8.20)
\end{aligned}
$$

Where the impedance of the system when looking for the converter end is as follows:

$$
Z_{eq}(h) = \frac{1}{\frac{1}{Z_F(h)} + \frac{1}{Z_{3.2}(h)}} \qquad (8.21)
$$

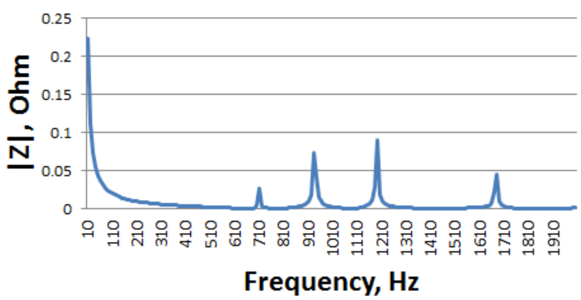

(a) Filter Impedance

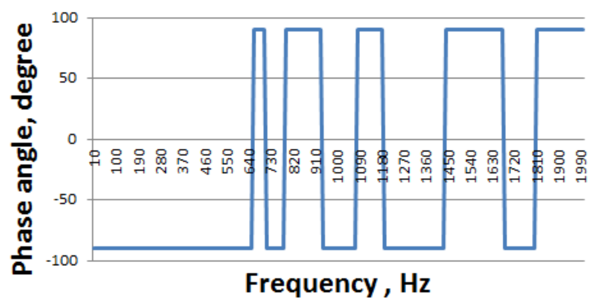

(b) Filter Phase

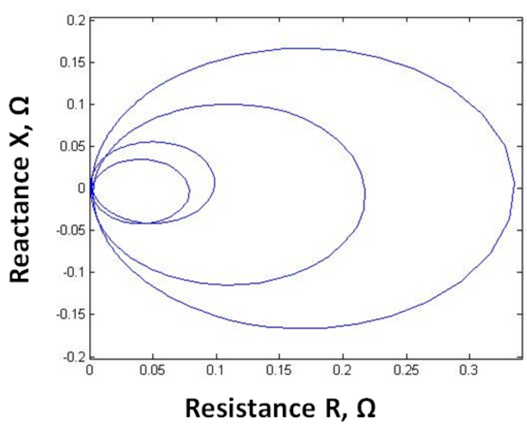

(c) Filter Impedance Locus

Figure 8.7: Filter Impedance and Impedance Locus using VFSPWM$_{12-9}$

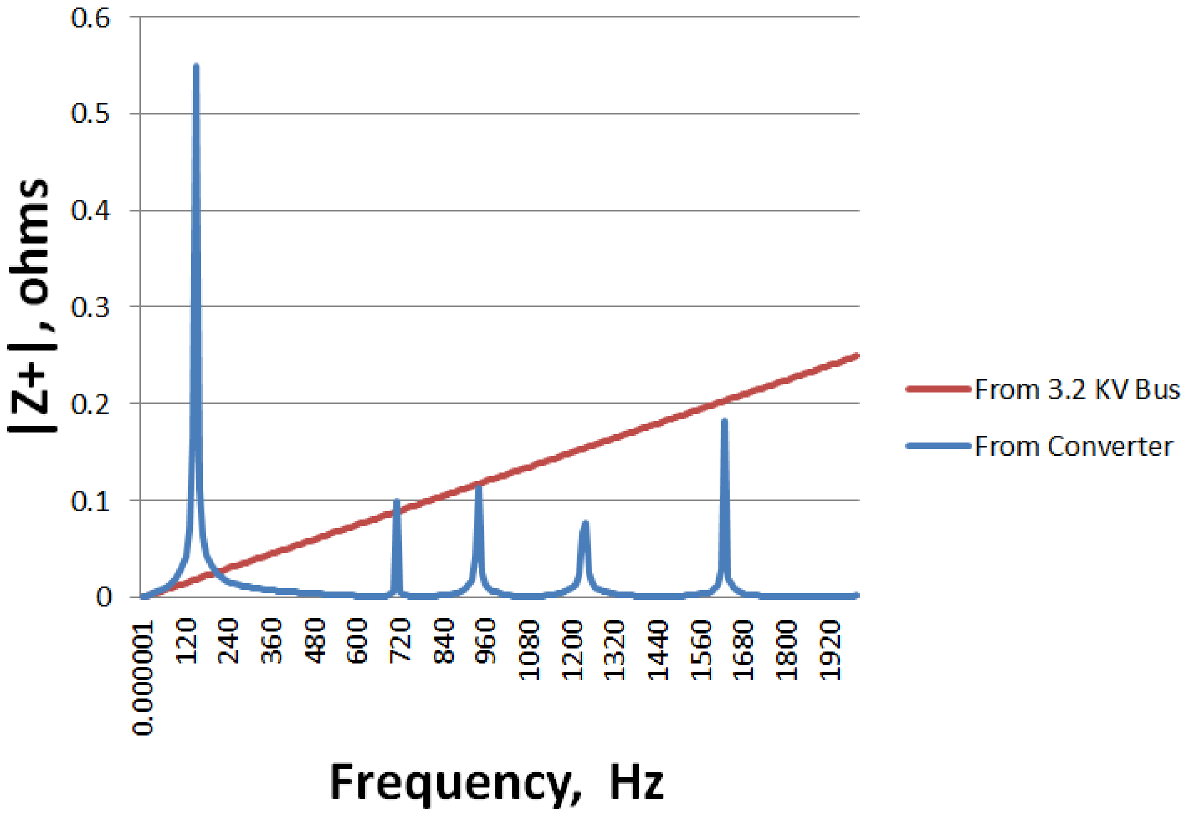

Figure 8.8: System Impedance using VFSPWM_{12-9}

8.3.2.3 Harmonic Injection The voltage source harmonics, $V_{3.2}(h)$, is calculated using the equations in section 3.4.1.2. The filter current is calculated usign equation (8.20):

$$I_F(h) = \frac{V_{3.2}(h)}{Z_F(h)} \tag{8.22}$$

From equation (8.20), the current that flows through the transformer to the system has the following relationship:

$$I_T(h) = I_{sys}(h) = \frac{V_{3.2}(h)}{Z_{3.2}(h)} \tag{8.23}$$

Finally the voltage at the 400 kV bus can be calculated as follows:

$$V_{400}(h) = Z_{sys}(h) * I_{sys}(h) \tag{8.24}$$

The impedance from the 3.2 kV bus, $Z_{3.2}$, and from the converter, Z_{eq}, are plotted in Figure 8.8. The system resonance is at 130 Hz with a value equal to 0.566 Ω. The rest of the resonance are caused by the filter and placed at the harmonic orders they are filtering, 11^{th}, 13^{th}, 18^{th}, 24^{th} and 30^{th}. Table 8.3 shows the calculated harmonics. These values comply with IEEE 519 harmonic distortion limits:

$$V_h \leq 3\% \text{ and } THD_v \leq 5\% \text{ for } V \leq 69kV$$

$$V_h \leq 1\% \text{ and } THD_v \leq 1.5\% \text{ for } V \geq 161kV \text{ [50]}$$

The transformer is safe because the K-factor is 1.458 which less than 4. The equation used to calculate the K-factor is:

$$K = \frac{\sum_{h=1} \left(\frac{hI_h}{I_1}\right)^2}{1 + THD_I^2}$$

And the derating factor is

$$D = \frac{1.15}{1 + 1.15K}$$

By using the standard transformer, it can not be loaded more than 94.38%.

Table 8.3: VFSPWM$_{(12-9)}$ Harmonic Distortion Results

		3.2 kV bus	Converter Current	Current to Transformer	Current to Filter	400kV bus
THD. %		10.81	1413	2.92	883.6	1.47
Fundamental	PU	1.196	7.63E-04	0.002741	0.003262	1.02
h=2		0.7567	107.910	0.20465	55.72	0.10339
3	% of Fund.	1.0255	146.239	0.27735	75.51	0.14011
4		1.1672	166.445	0.31567	85.95	0.15947
5		3.5535	506.722	0.96101	261.65	0.48549
6		1.1184	159.476	0.30245	82.35	0.15279
7		1.1184	159.476	0.30245	82.35	0.15279
8		1.2830	182.947	0.34696	94.47	0.17528
9		1.0995	156.782	0.29734	80.96	0.15021
10		0.9104	129.814	0.24620	67.03	0.12437
11		5.2549	749.339	1.42114	386.93	0.71793
12		0.5902	84.160	0.15961	43.46	0.08063
13		3.6463	519.951	0.98610	268.48	0.49816
14		1.0177	145.127	0.27524	74.94	0.13905
15		0.8777	125.152	0.23735	64.62	0.11991
16		0.5256	74.945	0.14213	38.70	0.07180
17		3.9623	565.011	1.07156	291.75	0.54133
18		0.4485	63.962	0.12130	33.03	0.06128
19		1.5967	227.682	0.43180	117.57	0.21814
20		0.3341	47.637	0.09035	24.60	0.04564
21		2.8082	400.441	0.75945	206.77	0.38366
22		1.5354	218.937	0.41522	113.05	0.20976
23		1.5582	222.195	0.42140	114.73	0.21288
24		1.1247	160.379	0.30416	82.81	0.15366
25		3.1947	455.558	0.86398	235.23	0.43647
26		0.3786	53.990	0.10239	27.88	0.05173
27		0.2519	35.913	0.06811	18.54	0.03441
28		0.7113	101.434	0.19237	52.38	0.09718
29		0.8036	114.586	0.21731	59.17	0.10978
30		0.4711	67.180	0.12741	34.69	0.06436
31		2.7439	391.272	0.74206	202.04	0.37487
K-factor=				1.458680612		
D=				0.943549414		

8.3.3 VFSPWM$_{12-6}$ System Analysis

In this section we are calculating the harmonics at several points in the STATCOM system using the the VFSPWM$_{12-6}$. The calculation is brief because it follows the same procedure that presented in section 8.3.1.

8.3.3.1 System Impedance

The system impedance is the same. We are presenting the values here for convenience.

$$
\begin{aligned}
S_{base} &= 100MVA \\
V_{baseL} &= 3.2kV \\
I_{baseL} &= 18.042kA \\
Z_{baseL} &= 0.1024\Omega
\end{aligned}
$$

The base values at the high-voltage bus

$$
\begin{aligned}
S_{base} &= 100MVA \\
V_{baseH} &= 400kV \\
I_{baseH} &= 144.33A \\
Z_{baseH} &= 1600\Omega
\end{aligned}
$$

- 400 kV equivalent system

$$
\begin{aligned}
SCC &= 10000MVA \\
V &= 400kV \\
Z_{sys} &= 16\angle 87.14°\Omega \\
I_{3\phi SC} &= 100\angle -87.14° \text{ pu}
\end{aligned}
$$

using $I_{1\phi SC} = 0.9 I_{3\phi SC}$,

$$
\begin{aligned}
I_{1\phi SC} &= 90\angle -87.14° \text{ pu} \\
Z^{+} &= 0.0005 + j0.00999 \text{ pu} \\
Z^{0} &= 0.000666 + j0.013316 \text{ pu} \\
Z_{sys}(h) &= \begin{cases} 0.000666 + j0.013316 * h \text{ pu}, \;\; h = 3n = 3, 6, 9, 12, \ldots \\ 0.0005 + j0.00999 * h \text{ pu} \end{cases}
\end{aligned} \tag{8.25}
$$

- Transformer

$$
\begin{aligned}
R_g &= 46.5137 \text{ pu} \\
Z_T^{+} = Z_T^{-} &= 0.002 + j0.063132 \text{ pu} \\
Z_T^{0} &= 139.5411 + j0.063132 \text{ pu} \\
Z_T(h) &= \begin{cases} 139.5411 + j0.063132 * h \text{ pu}, \;\; h = 3n = 3, 6, 9, 12, \ldots \\ 0.002 + j0.063132 * h \text{ pu} \end{cases}
\end{aligned} \tag{8.26}
$$

- Filters

This has three-branch filters where Q_{10}=30 MVar, Q_{14}= 25 MVar, Q_{21}= 20. Therefore, the total is Q_f=75 MVar.

1. Branch 1: $h_n = 10$

$$\begin{aligned}
Q_{C_{10}} &= 29.7 \text{ MVar} \\
X_{C_{10}} &= 0.115\ \Omega \\
C_{10} &= 23.05 \text{ mF} \\
X_{L_{10}} &= 0.001149\ \Omega \\
L_{10} &= 3.048\ \mu H \\
X_n &= 0.01149\ \Omega \\
R_{10} &= 0.0001915\ \Omega \\
Z_{F_1} &= 0.0001915 + j(h * 0.001149 - \frac{0.115}{h})
\end{aligned} \tag{8.27}$$

2. Branch 2: $h_n = 14$

$$\begin{aligned}
Q_{C_{14}} &= 24.87 \text{ MVar} \\
X_{C_{14}} &= 0.1372\ \Omega \\
C_{14} &= 19.33 \text{ mF} \\
X_{L_{14}} &= 0.0007\ \Omega \\
L_{14} &= 1.857\ \mu H \\
X_n &= 0.0098\ \Omega \\
R_{14} &= 0.0001634\ \Omega \\
Z_{F_2} &= 0.0001634 + j(h * 0.0007 - \frac{0.1372}{h})
\end{aligned} \tag{8.28}$$

3. Branch 3: $h_n = 21$ (second-order damped filter)

$$\begin{aligned}
Q_{C_{21}} &= 19.95 \text{ MVar} \\
X_{C_{21}} &= 0.17105\ \Omega \\
C_{21} &= 15.51 \text{ mF} \\
X_{L_{21}} &= 0.00038788\ \Omega \\
L_{21} &= 1.0289\ \mu H \\
X_n &= 0.008145\ \Omega \\
R_{21} &= Q * X_n, \text{ where Q=5} \\
&= 5 * 0.008145 \\
&= 0.04073\ \Omega \\
Z_{F_3} &= \frac{jR_{21}hX_{L_{21}}}{R_{21} + jhX_{L21}} - j\frac{X_{C_{21}}}{h} \\
&= \frac{R_{21}(hX_{L_{21}})^2}{R_{21}^2 + (hX_{L_{21}})^2} + j\left(\frac{R_{21}^2 hX_{L_{21}}}{R_{21}^2 + (hX_{L_{21}})^2} - \frac{X_{C_{21}}}{h}\right) \\
&= \frac{6.128 * 10^{-9}h^2}{0.001659 + 1.5 * 10^{-7}h^2} + j\left(\frac{6.4347 * 10^{-6}}{0.001659 + 1.5 * 10^{-7}h^2} - \frac{0.17105}{h}\right)
\end{aligned} \tag{8.29}$$

The filter impedance is calculated as follows:

$$Z_F = \frac{1}{Z_{baseL}\left(\frac{1}{Z_{F_1}} + \frac{1}{Z_{F_2}} + \frac{1}{Z_{F_3}}\right)}$$

Figure 8.9a shows the impedance of the filter.The filter short circuits the voltages at 600 Hz, 840 Hz, and ate 1260 Hz and higher. The phase of the filter is depicted in Figure 8.9b. The phase is alternating between 90° and -90° at these resonance frequency. The filters supply the system with reactive power at the line frequency, capacitive. Figure 8.9c shows the filter resistance versus the reactance. This figure shows the four points where the filter is almost like a short circuit, very small resistance and zero reactance.

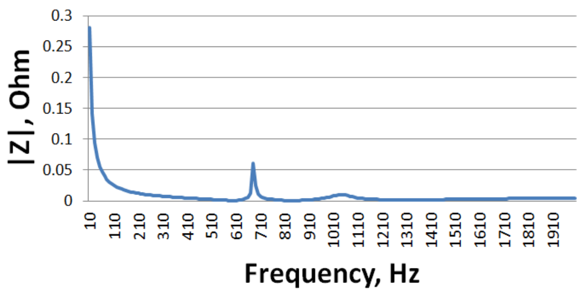

(a) Filter Impedance

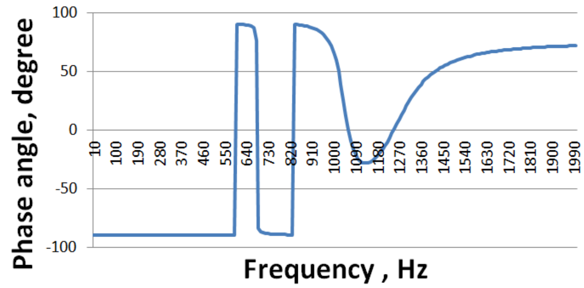

(b) Filter Phase

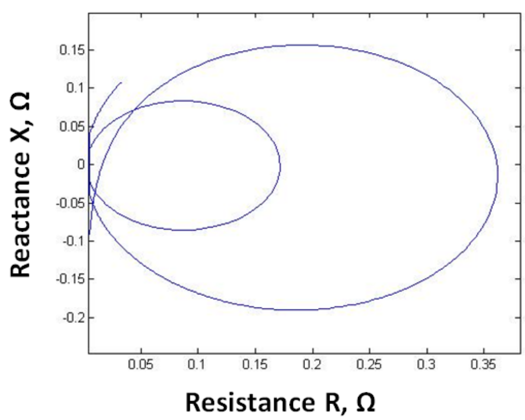

(c) Filter Impedance Locus

Figure 8.9: Filter Impedance and Impedance Locus using VFSPWM_{12-6}

8.3.3.2 Impedance Scan The impedance when we look from the 3.2 kV bus can be calculated as follows:

$$\begin{aligned} Z_{3.2}(h) &= Z_{sys}(h) + Z_T(h) \\ &= (0005 + j0.00999 * h) + (0.002 + j0.063135 * h) \\ &= 0.0025 + j0.073155 * h \text{ pu} \end{aligned} \tag{8.30}$$

Where the impedance of the system when looking for the converter end is as follows:

$$Z_{eq}(h) = \frac{1}{\frac{1}{Z_F(h)} + \frac{1}{Z_{3.2}(h)}} \tag{8.31}$$

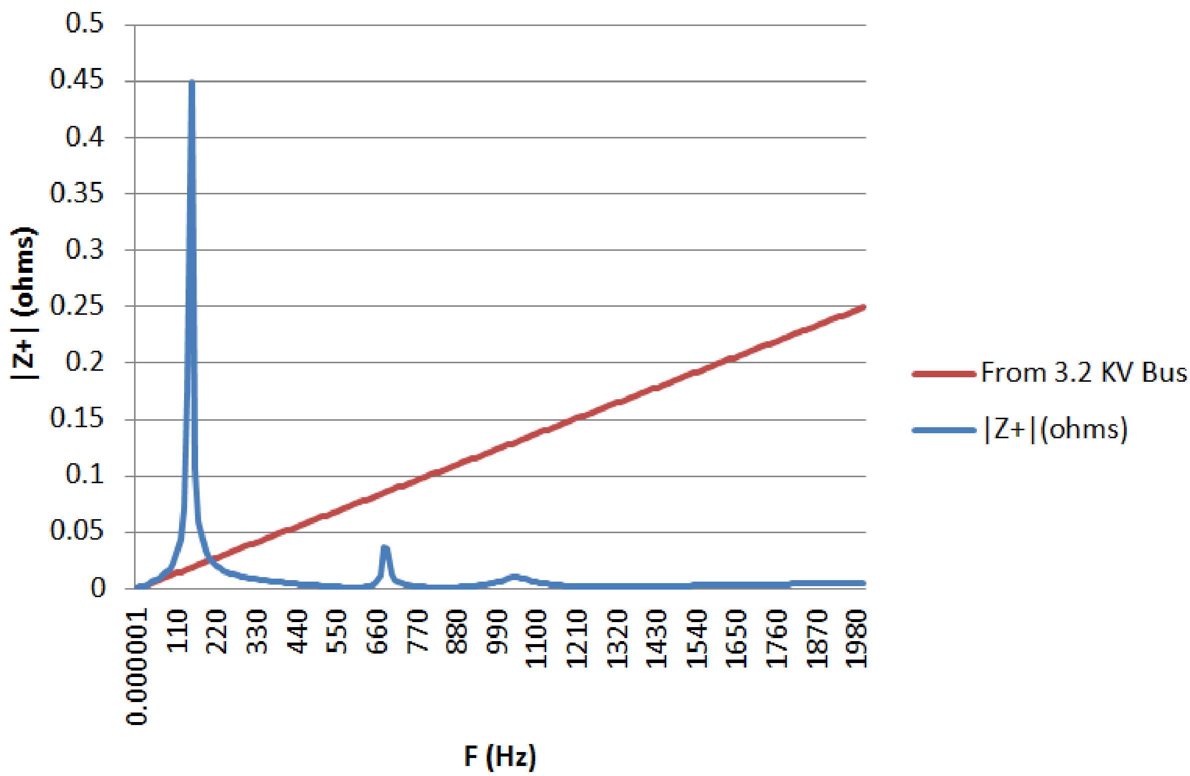

Figure 8.10: System Impedance using VFSPWM_{12-6}

8.3.3.3 Harmonic Injection

The voltage source harmonics, $V_{3.2}(h)$, is calculated using the equations in section 3.4.1.2. The filter current is calculated using equation (8.30):

$$I_F(h) = \frac{V_{3.2}(h)}{Z_F(h)} \tag{8.32}$$

From equation (8.30), the current that flows through the transformer to the system has the following relationship:

$$I_T(h) = I_{sys}(h) = \frac{V_{3.2}(h)}{Z_{3.2}(h)} \tag{8.33}$$

Finally the voltage at the 400 kV bus can be calculated as follows:

$$V_{400}(h) = Z_{sys}(h) * I_{sys}(h) \tag{8.34}$$

The impedance from the 3.2 kV bus, $Z_{3.2}$, and from the converter, Z_{eq}, are plotted in Figure 8.10. The system resonance is at 130 Hz with a value equal to 0.566 Ω. The rest of the resonance are caused by the filter and placed at the harmonic orders they are filtering, 10^{th}, 14^{th}, 21^{th}. Table 8.4 shows the calculated harmonics. These values comply with IEEE 519 harmonic distortion limits:

$$V_h \leq 3\% \text{ and } THD_v \leq 5\% \text{ for } V \leq 69kV$$

$$V_h \leq 1\% \text{ and } THD_v \leq 1.5\% \text{ for } V \geq 161kV \text{ [50]}$$

The transformer is safe because the K-factor is 1.5277 which less than 4. The equation used to calculate the K-factor is:

$$K = \frac{\sum_{h=1} \left(\frac{hI_h}{I_1}\right)^2}{1 + THD_I^2}$$

And the derating factor is

$$D = \frac{1.15}{1 + 1.15K}$$

By using the standard transformer, it can not be loaded more than 93.56%.

Table 8.4: VFSPWM$_{(12-6)}$ Harmonic Distortion Results

		3.2 kV bus	Converter Current	Current to Transformer	Current to Filter	400kV bus
THD. %		10.68	198	2.889	122	1.45
Fundamental	PU	1.11	1.23E-03	0.0019	0.0245	1
h=2		2.4570	49.724	0.66447	25.31	0.33568
3	% of Fund.	1.5794	31.964	0.42714	16.27	0.21578
4		3.6794	74.463	0.99506	37.90	0.50269
5		1.9454	39.371	0.52612	20.04	0.26579
6		0.9737	19.706	0.26334	10.03	0.13303
7		0.5665	11.464	0.15320	5.83	0.07739
8		3.1734	64.223	0.85822	32.68	0.43356
9		0.7222	14.616	0.19531	7.44	0.09867
10		1.6039	32.459	0.43376	16.52	0.21913
11		2.6238	53.099	0.70957	27.02	0.35846
12		2.8136	56.940	0.76090	28.98	0.38439
13		1.9207	38.870	0.51943	19.78	0.26241
14		2.7930	56.525	0.75535	28.77	0.38159
15		1.5888	32.154	0.42968	16.36	0.21707
16		2.4876	50.343	0.67275	25.62	0.33986
17		0.7124	14.417	0.19265	7.34	0.09732
18		0.7599	15.378	0.20550	7.83	0.10382
19		1.6757	33.912	0.45318	17.26	0.22894
20		2.0539	41.567	0.55547	21.15	0.28061
21		1.5767	31.908	0.42639	16.24	0.21540
22		0.7731	15.647	0.20909	7.96	0.10563
23		1.4605	29.557	0.39498	15.04	0.19953
24		0.8129	16.452	0.21985	8.37	0.11106
25		1.8159	36.751	0.49110	18.70	0.24810
26		1.9710	39.889	0.53304	20.30	0.26928
27		2.8967	58.622	0.78338	29.83	0.39575
28		2.0431	41.347	0.55252	21.04	0.27913
29		0.4494	9.095	0.12154	4.63	0.06140
30		2.0728	41.948	0.56056	21.35	0.28319
31		0.7735	15.653	0.20918	7.97	0.10567
K-factor=				1.527760527		
D=				0.93559519		

8.3.4 VFSPWM$_{12-3}$ System Analysis

In this section we are calculating the harmonics at several points in the STATCOM system using the the VFSPWM$_{12-3}$. The calculation is brief because it follows the same procedure that presented in section 8.3.1.

8.3.4.1 System Impedance The system impedance is the same. We are presenting the values here for convenience.

$$
\begin{aligned}
S_{base} &= 100MVA \\
V_{baseL} &= 3.2kV \\
I_{baseL} &= 18.042kA \\
Z_{baseL} &= 0.1024\Omega
\end{aligned}
$$

The base values at the high-voltage bus

$$
\begin{aligned}
S_{base} &= 100MVA \\
V_{baseH} &= 400kV \\
I_{baseH} &= 144.33A \\
Z_{baseH} &= 1600\Omega
\end{aligned}
$$

- 400 kV equivalent system

$$
\begin{aligned}
SCC &= 10000MVA \\
V &= 400kV \\
Z_{sys} &= 16\angle 87.14°\Omega \\
I_{3\phi SC} &= 100\angle -87.14° \text{ pu}
\end{aligned}
$$

using $I_{1\phi SC} = 0.9 I_{3\phi SC}$,

$$
\begin{aligned}
I_{1\phi SC} &= 90\angle -87.14° \text{ pu} \\
Z^{+} &= 0.0005 + j0.00999 \text{ pu} \\
Z^{0} &= 0.000666 + j0.013316 \text{ pu} \\
Z_{sys}(h) &= \begin{cases} 0.000666 + j0.013316 * h \text{ pu}, \;\; h = 3n = 3, 6, 9, 12, \ldots \\ 0.0005 + j0.00999 * h \text{ pu} \end{cases}
\end{aligned} \tag{8.35}
$$

- Transformer

$$
\begin{aligned}
R_g &= 46.5137 \text{ pu} \\
Z_T^{+} = Z_T^{-} &= 0.002 + j0.063132 \text{ pu} \\
Z_T^{0} &= 139.5411 + j0.063132 \text{ pu} \\
Z_T(h) &= \begin{cases} 139.5411 + j0.063132 * h \text{ pu}, \;\; h = 3n = 3, 6, 9, 12, \ldots \\ 0.002 + j0.063132 * h \text{ pu} \end{cases}
\end{aligned} \tag{8.36}
$$

- Filters

This has seven-branch filters where Q_5= Q_7= Q_{11}= 15 MVar, Q_{13}=20 MVar,and Q_{17}= Q_{23}= Q_{25}= 10 MVar. Therefore, the total is Q_f=95 MVar.

1. Branch 1: $h_n = 5$

$$\begin{aligned}
Q_{C_5} &= 14.4 \text{ MVar} \\
X_{C_5} &= 0.237037037\ \Omega \\
C_5 &= 11.190591 \text{ mF} \\
X_{L_5} &= 0.009481481\ \Omega \\
L_5 &= 25.1504\ \mu H \\
X_n &= 0.047407407\ \Omega \\
R_5 &= 0.000790123\ \Omega \\
Z_{F_1} &= 0.000790123 + j(h * 0.009481481 - \frac{0.237037037}{h})
\end{aligned} \tag{8.37}$$

2. Branch 2: $h_n = 7$

$$\begin{aligned}
Q_{C_7} &= 14.69387755 \text{ MVar} \\
X_{C_7} &= 0.232296296\ \Omega \\
C_7 &= 11.418971 \text{ mF} \\
X_{L_7} &= 0.004740741\ \Omega \\
L_7 &= 12.5752\ \mu H \\
X_n &= 0.033185185\ \Omega \\
R_7 &= 0.000553086\ \Omega \\
Z_{F_2} &= 0.000553086 + j(h * 0.004740741 - \frac{0.232296296}{h})
\end{aligned} \tag{8.38}$$

3. Branch 3: $h_n = 11$ (second-order damped filter)

$$\begin{aligned}
Q_{C_{11}} &= 14.87603306 \text{ MVar} \\
X_{C_{11}} &= 0.229451852\ \Omega \\
C_{11} &= 11.560528 \text{ mF} \\
X_{L_{11}} &= 0.001896296\ \Omega \\
L_{11} &= 5.03009\ \mu H \\
X_n &= 0.020859259\ \Omega \\
R_{11} &= 0.000347654\ \Omega \\
Z_{F_3} &= 0.000347654 + j(h * 0.001896296 - \frac{0.229451852}{h})
\end{aligned} \tag{8.39}$$

4. Branch 4: $h_n = 13$

$$\begin{aligned}
Q_{C_{13}} &= 19.8816568 \text{ MVar} \\
X_{C_{13}} &= 0.17168254\ \Omega \\
C_{13} &= 15.450521 \text{ mF} \\
X_{L_{13}} &= 0.001015873\ \Omega \\
L_{13} &= 2.69469\ \mu H \\
X_n &= 0.013206349\ \Omega \\
R_{13} &= 0.000220106\ \Omega \\
Z_{F_4} &= 0.000220106 + j(h * 0.001015873 - \frac{0.17168254}{h})
\end{aligned} \tag{8.40}$$

5. Branch 5: $h_n = 17$

$$
\begin{aligned}
Q_{C_{17}} &= 9.965397924 \text{ MVar} \\
X_{C_{17}} &= 0.342518519\ \Omega \\
C_{17} &= 7.74435 \text{ mF} \\
X_{L_{17}} &= 0.001185185\ \Omega \\
L_{17} &= 3.1438\ \mu H \\
X_n &= 0.020148148\ \Omega \\
R_{17} &= 0.000335802\ \Omega \\
Z_{F_5} &= 0.000335802 + j(h * 0.001185185 - \frac{0.342518519}{h})
\end{aligned} \tag{8.41}
$$

6. Branch 6: $h_n = 23$

$$
\begin{aligned}
Q_{C_{23}} &= 9.981096408 \text{ MVar} \\
X_{C_{23}} &= 0.341979798\ \Omega \\
C_{23} &= 7.756554 \text{ mF} \\
X_{L_{23}} &= 0.000646465\ \Omega \\
L_{23} &= 1.7148E\ \mu H \\
X_n &= 0.014868687\ \Omega \\
R_{23} &= 0.000247811\ \Omega \\
Z_{F_6} &= 0.000247811 + j(h * 0.000646465 - \frac{0.341979798}{h})
\end{aligned} \tag{8.42}
$$

7. Branch 7: $h_n = 25$

$$\begin{aligned}
Q_{C_{25}} &= 9.984 \text{ MVar} \\
X_{C_{25}} &= 0.341880342\ \Omega \\
C_{25} &= 7.75881 \text{ mF} \\
X_{L_{25}} &= 0.000547009\ \Omega \\
L_{25} &= 1.45099\ \mu H \\
X_n &= 0.01367521\ \Omega \\
R_{25} &= 0.00022792\ \Omega \\
Z_{F_7} &= 0.00022792 + j(h * 0.000547009 - \frac{0.341880342}{h}) \qquad (8.43)
\end{aligned}$$

The filter impedance is calculated as follows:

$$Z_F = \frac{1}{Z_{baseL}\left(\frac{1}{Z_{F_1}} + \frac{1}{Z_{F_2}} + \frac{1}{Z_{F_3}} + \frac{1}{Z_{F_4}} + \frac{1}{Z_{F_5}} + \frac{1}{Z_{F_6}} + \frac{1}{Z_{F_7}}\right)}$$

Figure 8.11a shows the impedance of the filter.The filter short circuits the voltages at 300 Hz, 420 Hz, 660 Hz, 780 Hz, 1020 Hz, 1380 Hz and 1500 Hz. The phase of the filter is depicted in Figure 8.11b. The phase is alternating between 90° and -90° at these resonance frequency. The filters supply the system with reactive power at the line frequency, capacitive. Figure 8.11c shows the filter resistance versus the reactance. This figure shows the four points where the filter is almost like a short circuit, very small resistance and zero reactance.

8.3.4.2 Impedance Scan The impedance when we look from the 3.2 kV bus can be calculated as follows:

$$\begin{aligned}
Z_{3.2}(h) &= Z_{sys}(h) + Z_T(h) \\
&= (0005 + j0.00999 * h) + (0.002 + j0.063135 * h) \\
&= 0.0025 + j0.073155 * h \text{ pu} \qquad (8.44)
\end{aligned}$$

Where the impedance of the system when looking for the converter end is as follows:

$$Z_{eq}(h) = \frac{1}{\frac{1}{Z_F(h)} + \frac{1}{Z_{3.2}(h)}} \qquad (8.45)$$

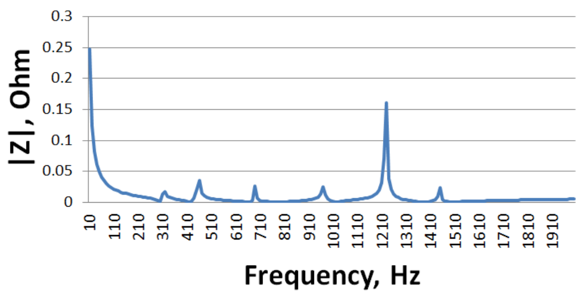

(a) Filter Impedance

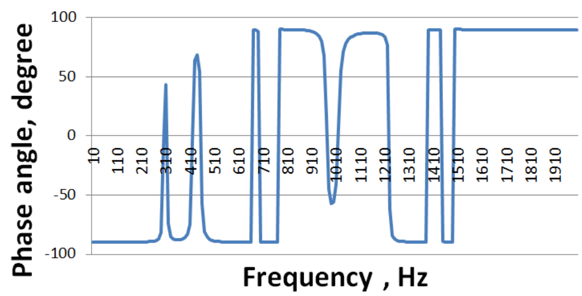

(b) Filter Phase

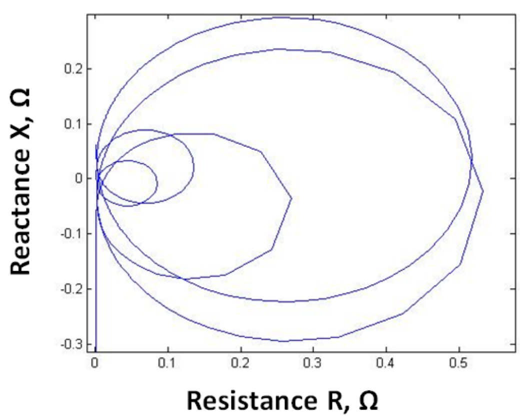

(c) Filter Impedance Locus

Figure 8.11: Filter Impedance and Impedance Locus using VFSPWM_{12-3}

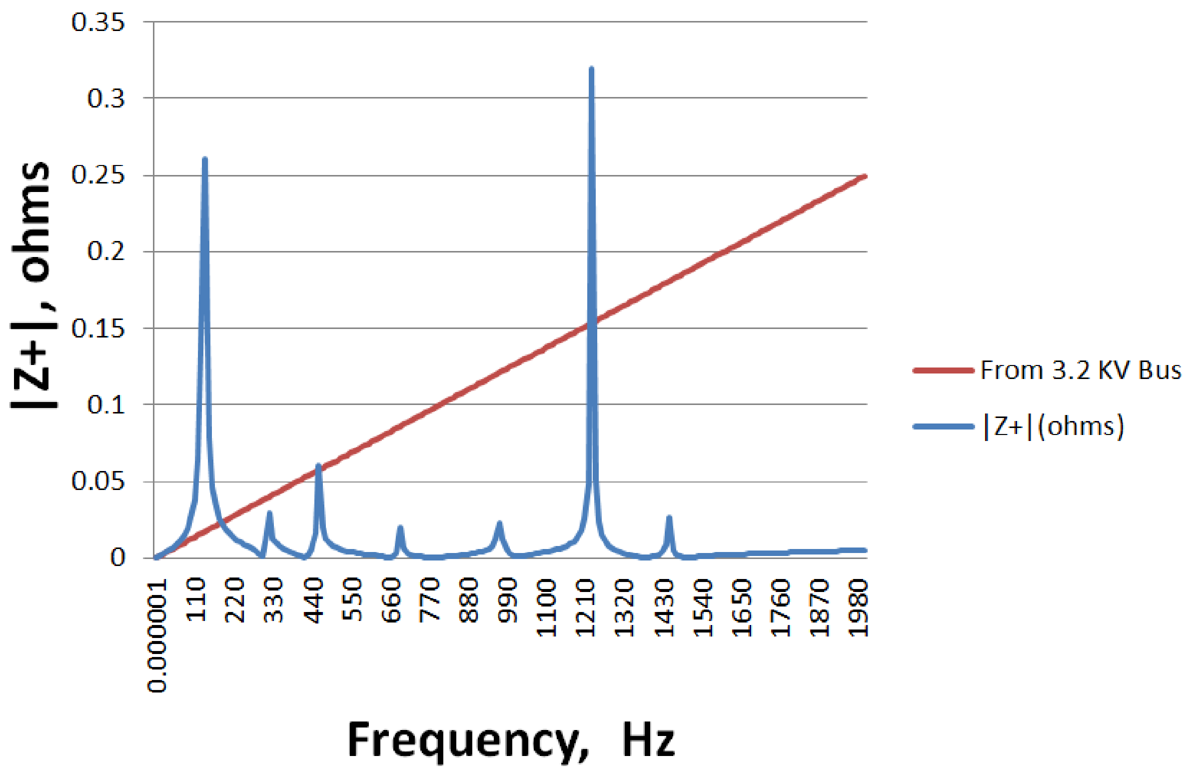

Figure 8.12: System Impedance using VFSPWM_{12-3}

8.3.4.3 Harmonic Injection

The voltage source harmonics, $V_{3.2}(h)$, is calculated using the equations in section 3.4.1.2. The filter current is calculated usign equation (8.44):

$$I_F(h) = \frac{V_{3.2}(h)}{Z_F(h)} \tag{8.46}$$

From equation (8.44), the current that flows through the transformer to the system has the following relationship:

$$I_T(h) = I_{sys}(h) = \frac{V_{3.2}(h)}{Z_{3.2}(h)} \tag{8.47}$$

Finally the voltage at the 400 kV bus can be calculated as follows:

$$V_{400}(h) = Z_{sys}(h) * I_{sys}(h) \tag{8.48}$$

The impedance from the 3.2 kV bus, $Z_{3.2}$, and from the converter, Z_{eq}, are plotted in Figure 8.12. The system resonance is at 130 Hz with a value equal to 0.566 Ω. The rest of the resonance are caused by the filter and placed at the harmonic orders they are filtering, 5^{th}, 7^{th}, 11^{th}, 13^{th}, 17^{th}, 23^{th} and , 25^{th}. Table 8.5 shows the calculated harmonics. These values comply with IEEE 519 harmonic distortion limits:

$$V_h \leq 3\% \text{ and } THD_v \leq 5\% \text{ for } V \leq 69kV$$
$$V_h \leq 1\% \text{ and } THD_v \leq 1.5\% \text{ for } V \geq 161kV$$ [50]

The transformer is safe because the K-factor is 1.5277 which less than 4. The equation used to calculate the K-factor is:

$$K = \frac{\sum_{h=1} \left(\frac{hI_h}{I_1}\right)^2}{1 + THD_I^2}$$

And the derating factor is

$$D = \frac{1.15}{1 + 1.15K}$$

By using the standard transformer, it can not be loaded more than 93.56%.

Table 8.5: VFSPWM$_{(12-3)}$ Harmonic Distortion Results

		3.2 kV bus	Converter Current	Current to Transformer	Current to Filter	400kV bus
THD. %		10.899	61.28	1.528	83.31	1.489
Fundamental	PU	1.02	3.59E-03	0.00312	0.0245	1
h=2		0.1326	0.745	0.01860	1.01	0.01810
3	% of Fund.	1.0809	6.078	0.15160	8.26	0.14770
4		0.1811	1.018	0.02540	1.38	0.02470
5		3.0428	17.110	0.42670	23.26	0.41570
6		0.4608	2.591	0.06460	3.52	0.06300
7		4.3068	24.218	0.60400	32.92	0.58840
8		0.2194	1.234	0.03080	1.68	0.03000
9		1.9435	10.928	0.27250	14.86	0.26550
10		0.4861	2.733	0.06820	3.72	0.06640
11		3.0239	17.004	0.42410	23.12	0.41310
12		0.6483	3.646	0.09090	4.96	0.08860
13		3.3577	18.881	0.47090	25.67	0.45870
14		0.5835	3.281	0.08180	4.46	0.07970
15		0.9087	5.110	0.12740	6.95	0.12420
16		0.3812	2.144	0.05350	2.91	0.05210
17		2.2213	12.491	0.31150	16.98	0.30350
18		0.1024	0.576	0.01440	0.78	0.01400
19		0.9599	5.398	0.13460	7.34	0.13110
20		1.0972	6.170	0.15390	8.39	0.14990
21		5.2145	29.322	0.73130	39.86	0.71240
22		0.5880	3.306	0.08250	4.49	0.08030
23		1.8723	10.528	0.26260	14.31	0.25580
24		0.5362	3.015	0.07520	4.10	0.07330
25		2.1291	11.972	0.29860	16.28	0.29090
26		0.9835	5.531	0.13790	7.52	0.13440
27		2.5408	14.287	0.35630	19.42	0.34710
28		0.5226	2.939	0.07330	3.99	0.07140
29		2.9505	16.591	0.41380	22.56	0.40310
30		1.1719	6.590	0.16430	8.96	0.16010
31		1.6216	9.118	0.22740	12.40	0.22150
K-factor=				1.527760527		
D=				0.93559519		

8.3.5 VFSPWM$_{12-0}$ System Analysis

In this section we are calculating the harmonics at several points in the STATCOM system using the the VFSPWM$_{12-0}$. The calculation is brief because it follows the same procedure that presented in section 8.3.1.

8.3.5.1 System Impedance

The system impedance is the same. We are presenting the values here for convenience.

$$\begin{aligned} S_{base} &= 100MVA \\ V_{baseL} &= 3.2kV \\ I_{baseL} &= 18.042kA \\ Z_{baseL} &= 0.1024\Omega \end{aligned}$$

The base values at the high-voltage bus

$$\begin{aligned} S_{base} &= 100MVA \\ V_{baseH} &= 400kV \\ I_{baseH} &= 144.33A \\ Z_{baseH} &= 1600\Omega \end{aligned}$$

- 400 kV equivalent system

$$\begin{aligned}
SCC &= 10000MVA \\
V &= 400kV \\
Z_{sys} &= 16\angle 87.14^{\circ}\Omega \\
I_{3\phi SC} &= 100\angle -87.14^{\circ} \text{ pu}
\end{aligned}$$

using $I_{1\phi SC} = 0.9 I_{3\phi SC}$,

$$\begin{aligned}
I_{1\phi SC} &= 90\angle -87.14^{\circ} \text{ pu} \\
Z^{+} &= 0.0005 + j0.00999 \text{ pu} \\
Z^{0} &= 0.000666 + j0.013316 \text{ pu} \\
Z_{sys}(h) &= \begin{cases} 0.000666 + j0.013316 * h \text{ pu}, & h = 3n = 3, 6, 9, 12, \ldots \\ 0.0005 + j0.00999 * h \text{ pu} \end{cases} \qquad (8.49)
\end{aligned}$$

- Transformer

$$\begin{aligned}
R_g &= 46.5137 \text{ pu} \\
Z_T^{+} = Z_T^{-} &= 0.002 + j0.063132 \text{ pu} \\
Z_T^{0} &= 139.5411 + j0.063132 \text{ pu} \\
Z_T(h) &= \begin{cases} 139.5411 + j0.063132 * h \text{ pu}, & h = 3n = 3, 6, 9, 12, \ldots \\ 0.002 + j0.063132 * h \text{ pu} \end{cases} \qquad (8.50)
\end{aligned}$$

- Filters

This has seven-branch filters where Q_{10}= Q_{14}=20 MVar and Q_{23}= Q_{25}=15 MVar. Therefore, the total is Q_f=70 MVar.

1. Branch 1: $h_n = 10$

$$
\begin{aligned}
Q_{C_{10}} &= 19.8 \text{ MVar} \\
X_{C_{10}} &= 0.172390572\ \Omega \\
C_{10} &= 15.387063 \text{ mF} \\
X_{L_{10}} &= 0.001723906\ \Omega \\
L_{10} &= 4.57281\ \mu H \\
X_n &= 0.017239057\ \Omega \\
R_{10} &= 0.000287318\ \Omega \\
Z_{F_1} &= 0.000287318 + j(h * 0.001723906 - \frac{0.172390572}{h})
\end{aligned}
\tag{8.51}
$$

2. Branch 2: $h_n = 14$

$$
\begin{aligned}
Q_{C_{14}} &= 19.89795918 \text{ MVar} \\
X_{C_{14}} &= 0.17154188\ \Omega \\
C_{14} &= 15.46319 \text{ mF} \\
X_{L_{14}} &= 0.000875214\ \Omega \\
L_{14} &= 2.32158\ \mu H \\
X_n &= 0.012252991\ \Omega \\
R_{14} &= 0.000204217\ \Omega \\
Z_{F_2} &= 0.000204217 + j(h * 0.000875214 - \frac{0.17154188}{h})
\end{aligned}
\tag{8.52}
$$

3. Branch 3: $h_n = 23$ (second-order damped filter)

$$\begin{aligned}
Q_{C_{23}} &= 14.97164461 \text{ MVar} \\
X_{C_{23}} &= 0.227986532\ \Omega \\
C_{23} &= 11.63483 \text{ mF} \\
X_{L_{23}} &= 0.000430976\ \Omega \\
L_{23} &= 1.1432\ \mu H \\
X_n &= 0.009912458\ \Omega \\
R_{23} &= 0.000165208\ \Omega \\
Z_{F_3} &= 0.000165208 + j(h * 0.000430976 - \frac{0.227986532}{h}) \qquad (8.53)
\end{aligned}$$

4. Branch 4: $h_n = 25$

$$\begin{aligned}
Q_{C_{25}} &= 14.976 \text{ MVar} \\
X_{C_{25}} &= 0.227920228\ \Omega \\
C_{25} &= 11.638215 \text{ mF} \\
X_{L_{25}} &= 0.000364672\ \Omega \\
L_{25} &= 0.967324\ \mu H \\
X_n &= 0.009116809\ \Omega \\
R_{25} &= 0.000151947\ \Omega \\
Z_{F_4} &= 0.000151947 + j(h * 0.000364672 - \frac{0.227920228}{h}) \qquad (8.54)
\end{aligned}$$

The filter impedance is calculated as follows:

$$Z_F = \frac{1}{Z_{baseL}\left(\frac{1}{Z_{F_1}} + \frac{1}{Z_{F_2}} + \frac{1}{Z_{F_3}} + \frac{1}{Z_{F_4}}\right)}$$

Figure 8.13a shows the impedance of the filter.The filter short circuits the voltages at 600 Hz, 840 Hz, 1380 Hz and 1500 Hz. The phase of the filter is depicted in Figure 8.13b. The phase is alternating between 90° and -90° at these resonance frequency. The filters supply the system with reactive power at the line frequency, capacitive. Figure 8.13c shows the filter resistance versus the reactance. This figure shows the four points where the filter is almost like a short circuit, very small resistance and zero reactance.

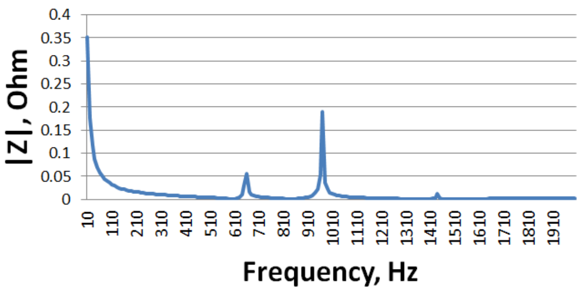

(a) Filter Impedance

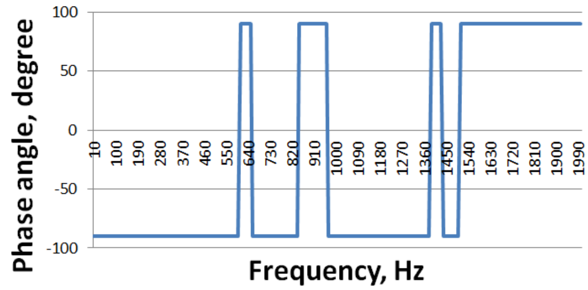

(b) Filter Phase

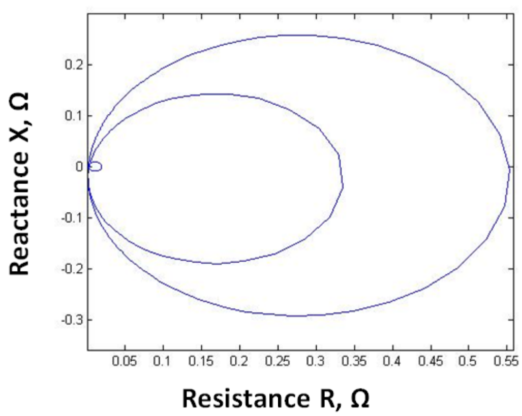

(c) Filter Impedance Locus

Figure 8.13: Filter Impedance and Impedance Locus using VFSPWM_{12-0}

8.3.5.2 Impedance Scan The impedance when we look from the 3.2 kV bus can be calculated as follows:

$$\begin{aligned} Z_{3.2}(h) &= Z_{sys}(h) + Z_T(h) \\ &= (0005 + j0.00999 * h) + (0.002 + j0.063135 * h) \\ &= 0.0025 + j0.073155 * h \text{ pu} \qquad (8.55) \end{aligned}$$

Where the impedance of the system when looking for the converter end is as follows:

$$Z_{eq}(h) = \frac{1}{\frac{1}{Z_F(h)} + \frac{1}{Z_{3.2}(h)}} \qquad (8.56)$$

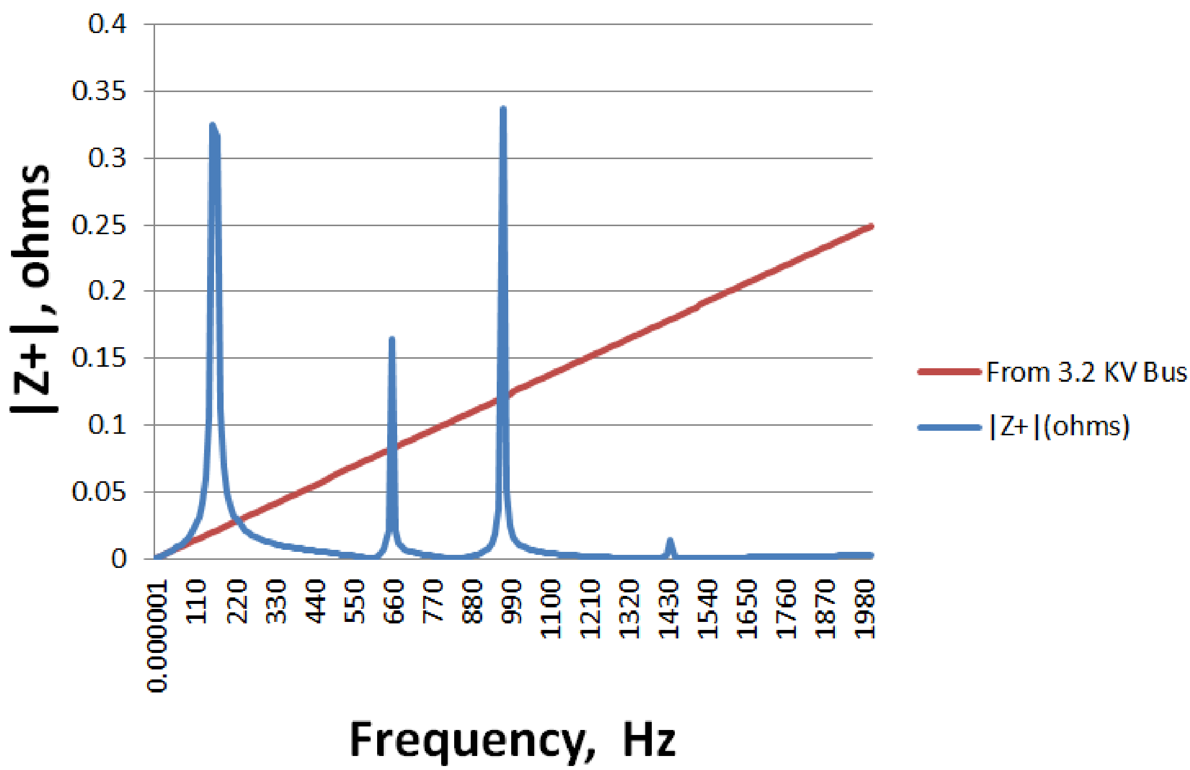

Figure 8.14: System Impedance using VFSPWM_{12-0}

8.3.5.3 Harmonic Injection The voltage source harmonics, $V_{3.2}(h)$, is calculated using the equations in section 3.4.1.2. The filter current is calculated usign equation (8.55):

$$I_F(h) = \frac{V_{3.2}(h)}{Z_F(h)} \tag{8.57}$$

From equation (8.55), the current that flows through the transformer to the system has the following relationship:

$$I_T(h) = I_{sys}(h) = \frac{V_{3.2}(h)}{Z_{3.2}(h)} \tag{8.58}$$

Finally the voltage at the 400 kV bus can be calculated as follows:

$$V_{400}(h) = Z_{sys}(h) * I_{sys}(h) \tag{8.59}$$

The impedance from the 3.2 kV bus, $Z_{3.2}$, and from the converter, Z_{eq}, are plotted in Figure 8.14. The system resonance is at 130 Hz with a value equal to 0.566 Ω. The rest of the resonance are caused by the filter and placed at the harmonic orders they are filtering, 10^{th}, 14^{th}, 23^{th} and 25^{th}. Table 8.6 shows the calculated harmonics. These values comply with IEEE 519 harmonic distortion limits:

$$V_h \leq 3\% \text{ and } THD_v \leq 5\% \text{ for } V \leq 69kV$$
$$V_h \leq 1\% \text{ and } THD_v \leq 1.5\% \text{ for } V \geq 161kV \text{ [50]}$$

The transformer is safe because the K-factor is 2.25 which less than 4. The equation used to calculate the K-factor is:

$$K = \frac{\sum_{h=1} \left(\frac{hI_h}{I_1}\right)^2}{1 + THD_I^2}$$

And the derating factor is

$$D = \frac{1.15}{1 + 1.15K}$$

By using the standard transformer, it can not be loaded more than 85.96%.

Table 8.6: VFSPWM$_{(12-0)}$ Harmonic Distortion Results

		3.2 kV bus	Converter Current	Current to Transformer	Current to Filter	400kV bus
THD. %		11.01	289.19	3.44	497.35	1.5
Fundamental	PU	1.08	1.08E-03	0.001407	0.001875	1
h=2		2.2790	103.9	0.71350	59.3	0.31140
3	% of Fund.	0.5749	26.2	0.18000	15	0.07850
4		3.7184	169.5	1.16420	96.8	0.50800
5		4.3504	198.3	1.36210	113.2	0.59440
6		0.6081	27.7	0.19040	15.8	0.08310
7		2.6559	121.1	0.83150	69.1	0.36280
8		0.4140	18.9	0.12960	10.8	0.05660
9		0.9429	43	0.29520	24.5	0.12880
10		3.2040	146	1.00320	83.4	0.43770
11		2.6909	122.7	0.84250	70	0.36760
12		4.3514	198.3	1.36240	113.2	0.59450
13		1.1596	52.9	0.36310	30.2	0.15840
14		3.8332	174.7	1.20010	99.8	0.52370
15		0.6927	31.6	0.21690	18	0.09460
16		0.4822	22	0.15100	12.5	0.06590
17		1.5352	70	0.48070	40	0.20970
18		0.5077	23.1	0.15900	13.2	0.06940
19		1.4856	67.7	0.46510	38.7	0.20300
20		1.1089	50.5	0.34720	28.9	0.15150
21		1.1143	50.8	0.34890	29	0.15220
22		0.7759	35.4	0.24290	20.2	0.10600
23		2.0195	92	0.63230	52.6	0.27590
24		1.0793	49.2	0.33790	28.1	0.14750
25		1.6958	77.3	0.53090	44.1	0.23170
26		0.5707	26	0.17870	14.9	0.07800
27		0.3252	14.8	0.10180	8.5	0.04440
28		0.4501	20.5	0.14090	11.7	0.06150
29		1.3474	61.4	0.42190	35.1	0.18410
30		0.5282	24.1	0.16540	13.7	0.07220
31		1.6020	73	0.50160	41.7	0.21890
K-factor=				2.252		
D=				0.859620272		

9.0 CONCLUSION AND FUTURE RESEARCH

9.1 CONCLUSION

The purpose of this research is to improve the efficiency of power electronics conversion systems. Power system equipment today is capable of operating at higher power ratings. Unfortunately, poor power conversion resulting in lower efficiency is one of the obstacles that prevents full utilization of existing infrastructure. Researchers realized that improvements in the power electronics technology efficiency can be accomplish in two ways. Several researchers preferred to modernize power electronics circuitry. These modifications raised the efficiency to an acceptable level. However, this solution may be economically unattractive. Other researchers provided new modulation controllers that lower the losses of the power electronic conversion. It is the latter approach that has been emphasized throughout this body of work. This dissertation shows a novel carrier based pulse width modulation (PWM) technique called the Variable Frequency Inverse Sinusoidal Pulse Width Modulation, VFSPWM, that combines several concepts to improve power converter performance.

A single- and three-phase PSCAD model has been built to simulate the VFSPWM operation. The carrier signal switches at two different frequencies. Each half-cycle is divided, evenly,into three regions. The carrier in the first and last regions switches at high frequency, while it switches at low frequency in the second area. The carrier has a shape of an inverse sinusoidal wave. This structure widens the pulses of the controller, hence, allow the switches to conduct longer. When the pulses are wider, the total area of the pulses is greater resulting in higher fundamental component.

A mathematical model has be represented to validate the PSCAD model. The fundamental component and the total harmonic distortions (THD) are calculated to validate the

PSCAD model. To increase confidence in the validation, a PSPICE model has been built to compare the converter fundamental component and THD to the PSCAD model. The results of the two validation methods guaranteed the reliability of the PSCAD model.

The PSCAD model is based upon deal operation of the converter switching devices. The output of the converter would be more realistic if the model added several switching characteristics such as switching rise/fall time and switching delay. Therefore, a PSPICE model that replaced ideal switching devices with switches that perform similarly to the real physical components was built. Also, the ideal comparators of the controllers were replaced by real operational amplifiers models. The comparison between the ideal and "real" model has showed that the converters in the ideal model performs similarly to the real model when the modulation index is greater than 0.4.

9.2 CONTRIBUTION

The analysis of the single- and three-phase versions of the VFSPWM techniques has been presented. Sinusoidal Pulse Width Modulation (SPWM) is the benchmark in this dissertation due to its widely used applications in power electronics circuits. Since VFSPWM operates at two combined switching frequencies, the performance comparison to the SPWM is presented in two methods. The first method is when the VFSPWM and the SPWM have the same number of pulses per cycle. In this dissertation, this method is denoted *similar pulses test*. The second method is to compare the VFSPWM technique to the SPWM while the switching devices are under the same switching stress. Therefore, this method is called *similar stress* test in the dissertation work.

VFSPWM shows a significant increase in the converter fundamental voltage and current in comparison to the SPWM technique. This increase in the fundamental component means better utilization of the DC source.

During the switching of the power electronics devices in the converter, the voltage across the switching devices and the current that flows through the device are not simultaneously zero. The multiplication of these two quantities is considered a loss, known as switching power loss. VFSPWM reduces the total switching power loss because the number of pulses per half-cycle is reduced in comparison to the SPWM.

Improvement in the THD is observed as well. The analysis of the low-order harmonics ($5^{th}, 7^{th}, 11^{th}, 13^{th}$ and 17^{th}) has been conducted. When the switching rate is high, the harmonic components are shifted to high orders. The switching frequencies in the VFSPWM technique are greater than or equal to the SPWM switching frequencies. Therefore, the filters are more economic for the VFSPWM.

The performance of the VFSPWM technique was examined for a STATCOM application. The increase in the fundamental component results in substituting a DC source in the STATCOM application with a smaller and more affordable one. For example, the STATCOM application showed that the DC source using the VFSPWM technique is reduced by upto one-forth of that applying SPWM.

9.3 LIMITATIONS

The analysis of the VFSPWM technique neglected the protection circuits, known as snubber circuits. These circuits protect the converter switching devices from the overvoltage phenomena caused by voltage transient, and current spikes. It was better to analyze the model with omitted snubber circuits to reduce the sophistication of the evaluations. In addition, this approach helped to present clear, theoretical results and eliminate external unwanted factors.

The DC source applied in the analysis is assumed to be ideal. Usually the sources contain small ripple on top of the nominal DC value and have series impedances.

9.4 FUTURE RESEARCH

The VFSPWM technique can be used to other converter topologies. For example, it can be applied on multi-level converters such as the neutral-clamping point (NPC) technology. In the industrial applications, most of the converters are multi-level resulting in an output with less harmonic content and sometimes require no filters.

Each SPWM switching frequency has several corresponding switching frequencies in the VFSPWM technique. Finding the VFSPWM optimal switching frequency is a great potential research area. For instance, linear programming technique can be applied to calculate the optimal switching combination based on several variables such as switching losses, fundamental component, WTHD, and more.

A STATCOM controller is the application used to evaluate the VFSPWM performance algorithm in this dissertation work. It is recommended to analyze network stability under dynamic contingencies. In addition, it is of great benefit to examine the VFSPWM technique when applied to different transmission and distribution systems. For example, High-Voltage AC (HVDC) technology is a viable application that can be used to evaluate the quality of the transmitted power. Also, discharge time of different industrial butteries can be studied when applying the VFSPWM technique.

The comparison in this dissertation work is based on main measurements, i.e., fundamental component and WTHD. It is recommended to analyze the VFSPWM techniques using different factors such as power factor, distortion factor or lowest order harmonic factor.

APPENDIX

DATASHEETS

IXYS

	V_{CES}	I_{C25}	$V_{CE(sat)}$
Low $V_{CE(sat)}$ IGBT **IXGH/IXGM 40 N60**	**600 V**	**75 A**	**2.5 V**
High speed IGBT **IXGH/IXGM 40 N60A**	**600 V**	**75 A**	**3.0 V**

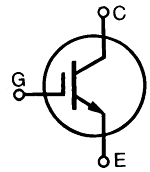

Symbol	Test Conditions	Maximum Ratings	
V_{CES}	T_J = 25°C to 150°C	600	V
V_{CGR}	T_J = 25°C to 150°C; R_{GE} = 1 MΩ	600	V
V_{GES}	Continuous	±20	V
V_{GEM}	Transient	±30	V
I_{C25}	T_C = 25°C, limited by leads	75	A
I_{C90}	T_C = 90°C	40	A
I_{CM}	T_C = 25°C, 1 ms	150	A
SSOA (RBSOA)	V_{GE}= 15 V, T_{VJ} = 125°C, R_G = 22 Ω Clamped inductive load, L = 30 µH	I_{CM} = 80 @ 0.8 V_{CES}	A
P_C	T_C = 25°C	250	W
T_J		-55 ... +150	°C
T_{JM}		150	°C
T_{stg}		-55 ... +150	°C
M_d	Mounting torque (M3)	1.13/10	Nm/lb.in.
Weight		TO-204 = 18 g, TO-247 = 6 g	
Maximum lead temperature for soldering 1.6 mm (0.062 in.) from case for 10 s		300	°C

Symbol	Test Conditions		Characteristic Values (T_J = 25°C, unless otherwise specified) min.	typ.	max.	
BV_{CES}	I_C = 250 µA, V_{GE} = 0 V		600			V
$V_{GE(th)}$	I_C = 250 µA, V_{CE} = V_{GE}		2.5		5	V
I_{CES}	V_{CE} = 0.8 • V_{CES} V_{GE} = 0 V	T_J = 25°C T_J = 125°C			200 1	µA mA
I_{GES}	V_{CE} = 0 V, V_{GE} = ±20 V				±100	nA
$V_{CE(sat)}$	I_C = I_{C90}, V_{GE} = 15 V	40N60 40N60A			2.5 3.0	V V

TO-247 AD (IXGH)

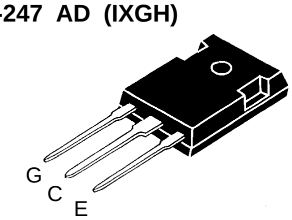

TO-204 AE (IXGM)

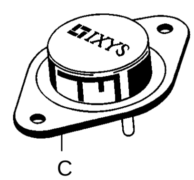

G = Gate, C = Collector,
E = Emitter, TAB = Collector

Features
- International standard packages
- 2nd generation HDMOS™ process
- Low $V_{CE(sat)}$
  - for low on-state conduction losses
- High current handling capability
- MOS Gate turn-on
  - drive simplicity
- Voltage rating guaranteed at high temperature (125°C)

Applications
- AC motor speed control
- DC servo and robot drives
- DC choppers
- Uninterruptible power supplies (UPS)
- Switch-mode and resonant-mode power supplies

Advantages
- Easy to mount with 1 screw (TO-247) (isolated mounting screw hole)
- High power density

Symbol	Test Conditions		Characteristic Values (T_J = 25°C, unless otherwise specified) min.	typ.	max.	
g_{fs}	$I_C = I_{C90}$; V_{CE} = 10 V, Pulse test, t ≤ 300 µs, duty cycle ≤ 2 %		25	35		S
C_{ies}	V_{CE} = 25 V, V_{GE} = 0 V, f = 1 MHz			4500		pF
C_{oes}				300		pF
C_{res}				60		pF
Q_g	$I_C = I_{C90}$, V_{GE} = 15 V, $V_{CE} = 0.5\ V_{CES}$			200	250	nC
Q_{ge}				45	80	nC
Q_{gc}				88	120	nC
$t_{d(on)}$	**Inductive load, T_J = 25°C**			100		ns
t_{ri}	$I_C = I_{C90}$, V_{GE} = 15 V, L = 100 µH			200		ns
$t_{d(off)}$	$V_{CE} = 0.8\ V_{CES}$, $R_G = R_{off}$ = 22 Ω			600		ns
t_{fi}	Switching times may increase for V_{CE} (Clamp) > 0.8 • V_{CES},	40N60A		200		ns
E_{off}	higher T_J or increased R_G	40N60A		3		mJ
$t_{d(on)}$	**Inductive load, T_J = 125°C**			100		ns
t_{ri}	$I_C = I_{C90}$, V_{GE} = 15 V,			200		ns
E_{on}	L = 100 µH			4		mJ
$t_{d(off)}$	$V_{CE} = 0.8\ V_{CES}$, $R_G = R_{off}$ = 22 Ω			600	1000	ns
t_{fi}	Remarks: Switching times	40N60		600	2000	ns
	may increase for V_{CE}	40N60A		300	800	ns
E_{off}	(Clamp) > 0.8 • V_{CES}, higher	40N60		12		mJ
	T_J or increased R_G	40N60A		6		mJ
R_{thJC}					0.5	K/W
R_{thCK}				0.25		K/W

TO-247 AD Outline

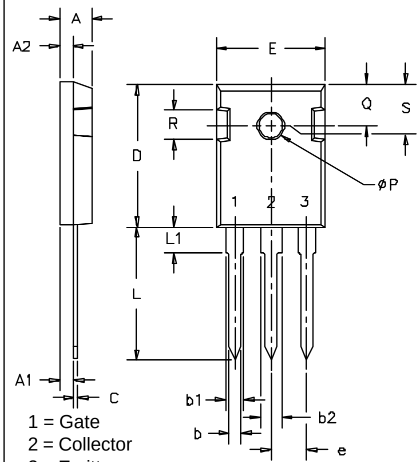

1 = Gate
2 = Collector
3 = Emitter
Tab = Collector

SYM	INCHES MIN	INCHES MAX	MILLIMETERS MIN	MILLIMETERS MAX
A	.185	.209	4.7	5.3
A1	.087	.102	2.2	2.54
A2	.059	.098	2.2	2.6
b	.040	.055	1.0	1.4
b1	.065	.084	1.65	2.13
b2	.113	.123	2.87	3.12
C	.016	.031	.4	.8
D	.819	.845	20.80	21.46
E	.610	.640	15.75	16.26
e	.215 BSC		5.45 BSC	
L	.780	.800	19.81	20.32
L1		.177		4.50
ØP	.140	.144	3.55	3.65
Q	.212	.244	5.4	6.2
R	.170	.216	4.32	5.49
S	.242 BSC		6.15 BSC	

TO-204AE Outline

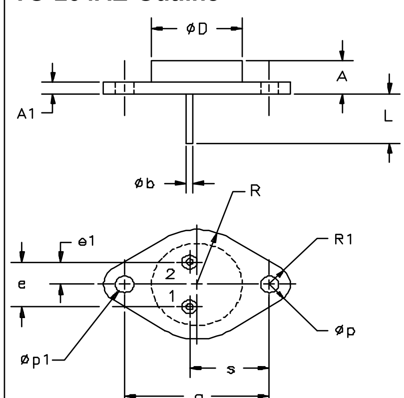

1 = Gate
2 = Emitter
Case = Collector

SYM	INCHES MIN	INCHES MAX	MILLIMETERS MIN	MILLIMETERS MAX
A	.250	.450	6.4	11.4
A1	.060	.135	1.53	3.42
Øb	.057	.063	1.45	1.60
ØD		.875		22.22
e	.420	.440	10.67	11.17
e1	.205	.225	5.21	5.71
L	.440	.480	11.18	12.19
Øp	.151	.165	3.84	4.19
Øp1	.151	.165	3.84	4.19
q	1.187 BSC		30.15 BSC	
R	.495	.525	12.58	13.33
R1	.131	.188	3.33	4.77
s	.655	.675	16.64	17.14

IXYS reserves the right to change limits, test conditions, and dimensions.

Fig. 1 Saturation Characteristics

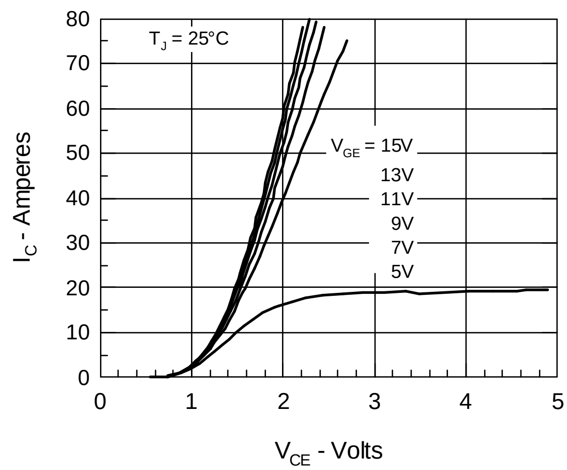

Fig. 2 Output Characterstics

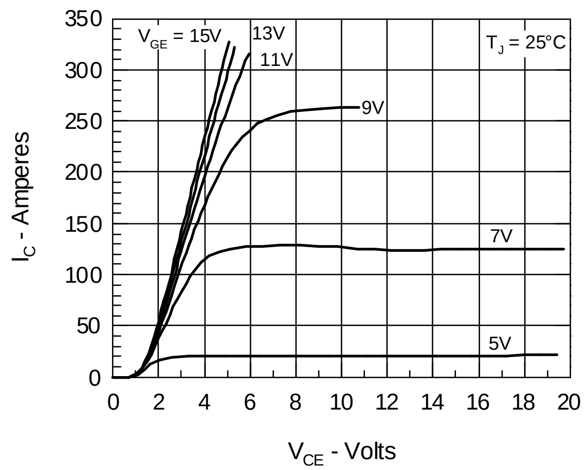

Fig. 3 Collector-Emitter Voltage vs. Gate-Emitter Voltage

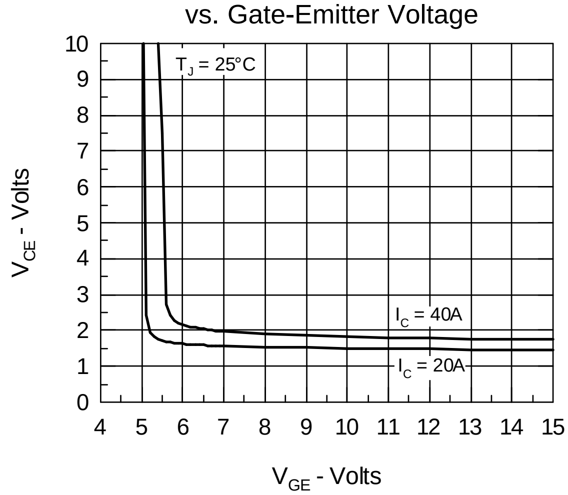

Fig. 4 Temperature Dependence of Output Saturation Voltage

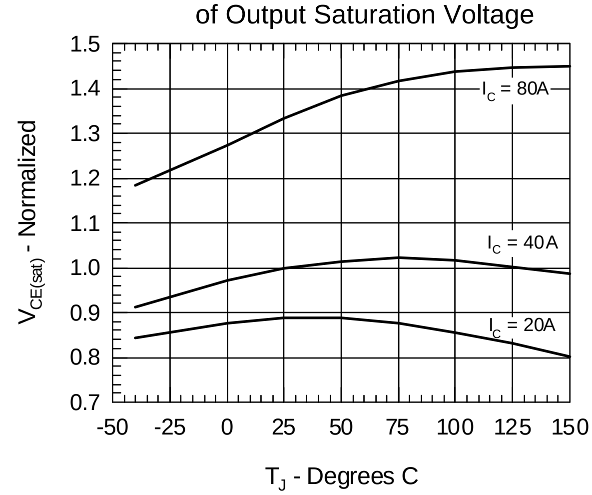

Fig. 5 Input Admittance

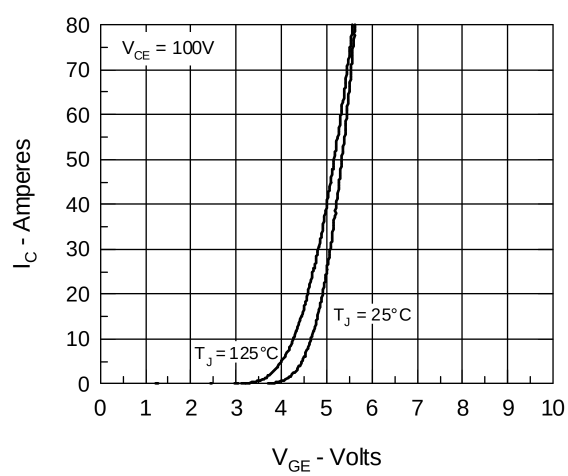

Fig. 6 Temperature Dependence of Breakdown and Threshold Voltage

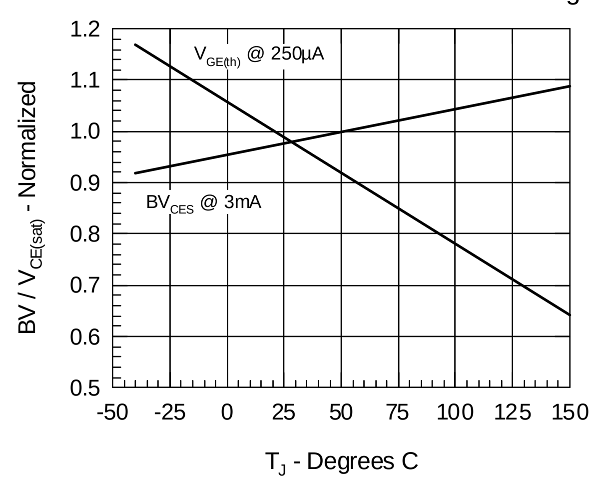

Fig.7 Gate Charge

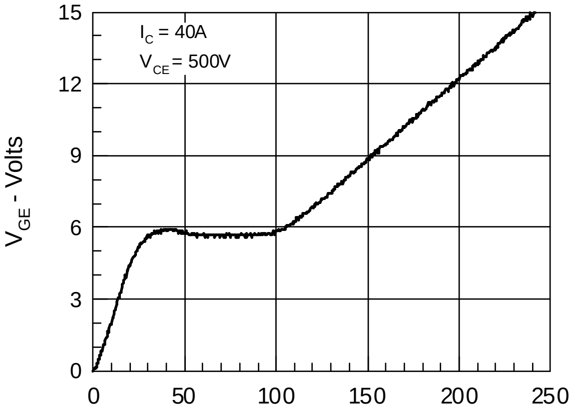

Fig.8 Turn-Off Safe Operating Area

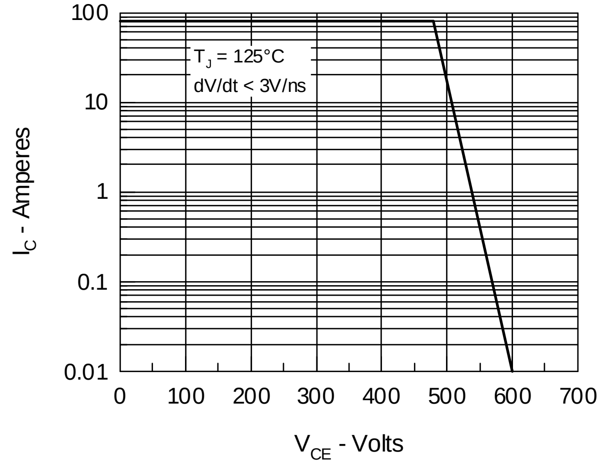

Fig.9 Capacitance Curves

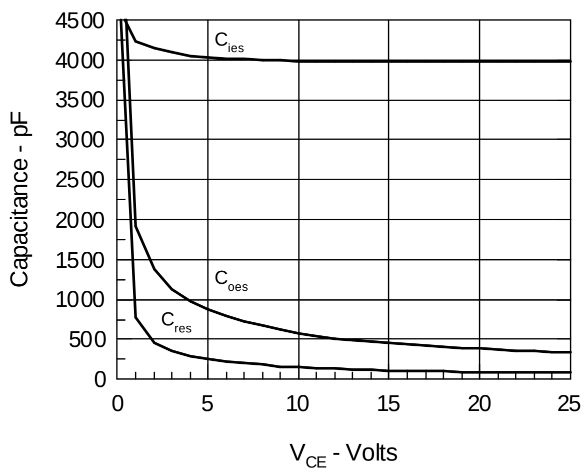

Fig.10 Transient Thermal Impedance

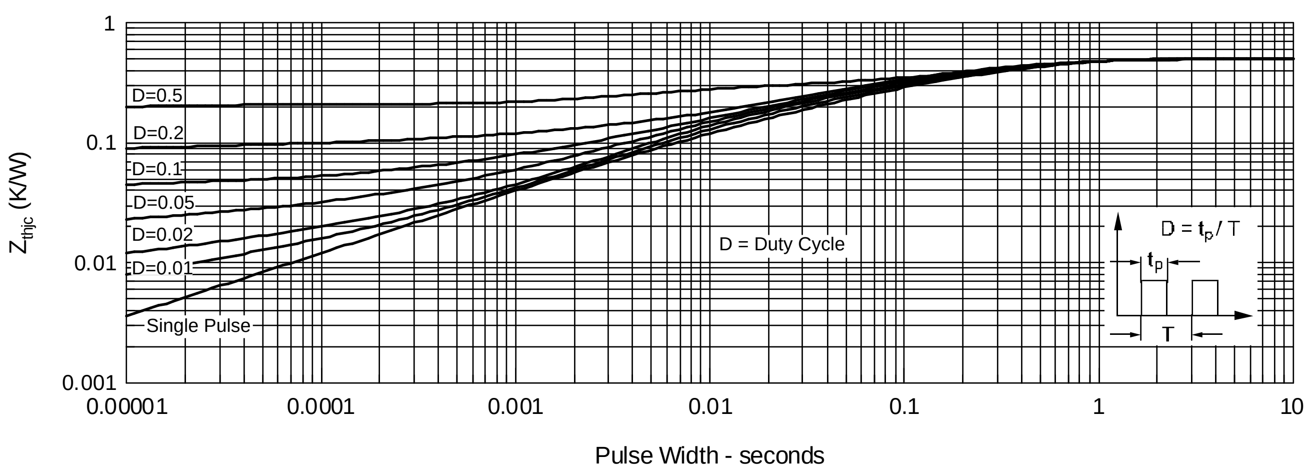

LM124
LM224 - LM324

LOW POWER QUAD OPERATIONAL AMPLIFIERS

- WIDE GAIN BANDWIDTH : 1.3MHz
- INPUT COMMON-MODE VOLTAGE RANGE INCLUDES GROUND
- LARGE VOLTAGE GAIN : 100dB
- VERY LOW SUPPLY CURRENT/AMPLI : 375µA
- LOW INPUT BIAS CURRENT : 20nA
- LOW INPUT OFFSET VOLTAGE : 5mV max.
  (for more accurate applications, use the equivalent parts LM124A-LM224A-LM324A which feature 3mV max)
- LOW INPUT OFFSET CURRENT : 2nA
- WIDE POWER SUPPLY RANGE :
  SINGLE SUPPLY : +3V TO +30V
  DUAL SUPPLIES : ±1.5V TO ±15V

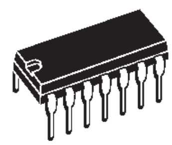

N
DIP14
(Plastic Package)

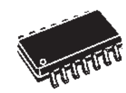

D
SO14
(Plastic Micropackage)

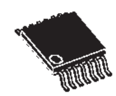

P
TSSOP14
(Thin Shrink Small Outline Package)

DESCRIPTION

These circuits consist of four independent, high gain, internally frequency compensated operational amplifiers . They operate from a single power supply over a wide range of voltages. Operation from split power supplies is also possible and the low power supply current drain is independent of the magnitude of the power supply voltage.

ORDER CODES

Part Number	Temperature Range	Package		
		N	D	P
LM124	-55°C, +125°C	•	•	•
LM224	-40°C, +105°C	•	•	•
LM324	0°C, +70°C	•	•	•
Example : LM224N				

PIN CONNECTIONS (top view)

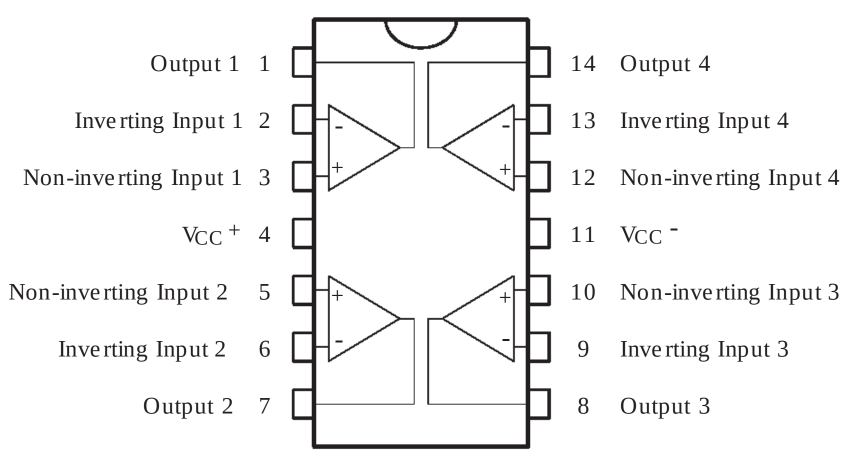

SCHEMATIC DIAGRAM (1/4 LM124)

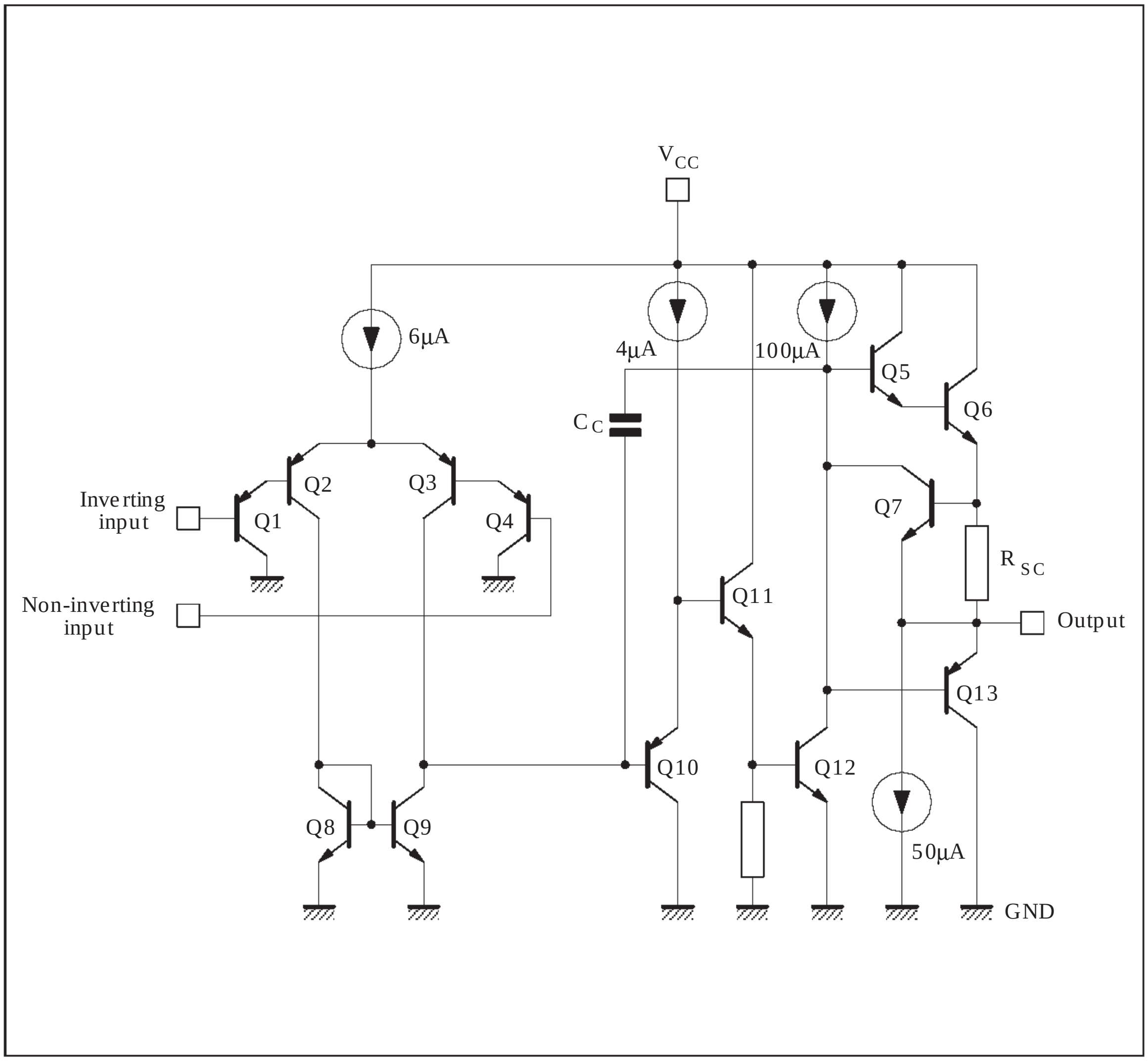

ABSOLUTE MAXIMUM RATINGS

Symbol	Parameter		LM124	LM224	LM324	Unit
V_{cc}	Supply Voltage		±16 or 32			V
V_i	Input Voltage		-0.3 to +32			V
V_{id}	Differential Input Voltage - (*)		+32	+32	+32	V
P_{tot}	Power Dissipation	N Suffix D Suffix	500 -	500 400	500 400	mW mW
-	Output Short-circuit Duration - (note 1)		Infinite			
I_{in}	Input Current – (note 6)		50	50	50	mA
T_{oper}	Operating Free Air Temperature Range		-55 to +125	-40 to +105	0 to +70	^oC
T_{stg}	Storage Temperature Range		-65 to +150	-65 to +150	-65 to +150	^oC

ELECTRICAL CHARACTERISTICS

V_{CC}^{+} = +5V, V_{CC}^{-} = Ground, V_O = 1.4V, T_{amb} = +25°C (unless otherwise specified)

Symbol	Parameter	LM124 - LM224 - LM324			Unit
		Min.	Typ.	Max.	
V_{io}	Input Offset Voltage (note 3) T_{amb} = +25°C LM324 $T_{min.} \leq T_{amb} \leq T_{max.}$ LM324		 2	 5 7 7 9	mV
I_{io}	Input Offset Current T_{amb} = +25°C $T_{min.} \leq T_{amb} \leq T_{max.}$		 2	 30 100	nA
I_{ib}	Input Bias Current (note 2) T_{amb} = +25°C $T_{min.} \leq T_{amb} \leq T_{max.}$		 20	 150 300	nA
A_{vd}	Large Signal Voltage Gain (V_{CC}^{+} = +15V, R_L = 2kΩ, V_O = 1.4V to 11.4V) T_{amb} = +25°C $T_{min.} \leq T_{amb} \leq T_{max.}$	 50 25	 100		V/mV
SVR	Supply Voltage Rejection Ratio ($R_S \leq$ 10kΩ) (V_{CC}^{+} = 5V to 30V) T_{amb} = +25°C $T_{min.} \leq T_{amb} \leq T_{max.}$	 65 65	 110		dB
I_{CC}	Supply Current, all Amp, no load T_{amb} = +25°C V_{CC} = +5V V_{CC} = +30V $T_{min.} \leq T_{amb} \leq T_{max.}$ V_{CC} = +5V V_{CC} = +30V		 0.7 1.5 0.8 1.5	 1.2 3 1.2 3	mA
V_{icm}	Input Common Mode Voltage Range (V_{CC} = +30V) - (note 4) T_{amb} = +25°C $T_{min.} \leq T_{amb} \leq T_{max.}$	 0 0		 V_{CC} -1.5 V_{CC} -2	V
CMR	Common-mode Rejection Ratio ($R_S \leq$ 10kΩ) T_{amb} = +25°C $T_{min.} \leq T_{amb} \leq T_{max}$	 70 60	 80		dB
I_{source}	Output Current Source (V_{id} = +1V) V_{CC} = +15V, V_o = +2V	 20	 40	 70	mA
I_{sink}	Output Sink Current (V_{id} = -1V) V_{CC} = +15V, V_o = +2V V_{CC} = +15V, V_o = +0.2V	 10 12	 20 50		 mA μA

ELECTRICAL CHARACTERISTICS (continued)

Symbol	Parameter	LM124 - LM224 - LM324			Unit
		Min.	Typ.	Max.	
V_{OH}	High Level Output Voltage (V_{CC} = +30V) T_{amb} = +25°C R_L = 2kΩ $T_{min.} \leq T_{amb} \leq T_{max.}$ T_{amb} = +25°C R_L = 10kΩ $T_{min.} \leq T_{amb} \leq T_{max.}$ (V_{CC} = +5V, R_L = 2kΩ) T_{amb} = +25°C $T_{min.} \leq T_{amb} \leq T_{max.}$	 26 26 27 27 3.5 3	 27 28		V
V_{OL}	Low Level Output Voltage (R_L = 10kΩ) T_{amb} = +25°C $T_{min.} \leq T_{amb} \leq T_{max.}$		 5	 20 20	mV
SR	Slew Rate V_{CC} = 15V, V_I = 0.5 to 3V, R_L = 2kΩ, C_L = 100pF, unity gain)		0.4		V/µs
GBP	Gain Bandwidth Product V_{CC} = 30V, f = 100kHz, V_{in} = 10mV R_L = 2kΩ, C_L = 100pF		1.3		MHz
THD	Total Harmonic Distortion f = 1kHz, A_V = 20dB, R_L = 2kΩ, V_O = $2V_{pp}$ C_L = 100pF, V_{CC} = 30V		0.015		%
e_n	Equivalent Input Noise Voltage f = 1kHz, R_s = 100Ω, V_{CC} = 30V		40		$\frac{nV}{\sqrt{Hz}}$
DV_{io}	Input Offset Voltage Drift		7	30	µV/°C
DI_{IO}	Input Offset Current Drift		10	200	pA/°C
V_O1/V_O2	Channel Separation (note 5) 1kHz ≤ f ≤ 20kHz		120		dB

Notes :
1. Short-circuits from the output to V_{CC} can cause excessive heating if V_{CC} > 15V. The maximum output current is approximately 40mA independent of the magnitude of V_{CC}. Destructive dissipation can result from simultaneous short-circuit on all amplifiers.
2. The direction of the input current is out of the IC. This current is essentially constant, independent of the state of the output so no loading change exists on the input lines.
3. V_o = 1.4V, R_s = 0Ω, 5V < V_{CC}^+ < 30V, 0 < V_{ic} < V_{CC}^+ - 1.5V
4. The input common-mode voltage of either input signal voltage should not be allowed to go negative by more than 0.3V. The upper end of the common-mode voltage range is V_{CC}^+ - 1.5V, but either or both inputs can go to +32V without damage.
5. Due to the proximity of external components insure that coupling is not originating via stray capacitance between these external parts. This typically can be detected as this type of capacitance increases at higher frequences.
6. This input current only exists when the voltage at any of the input leads is driven negative. It is due to the collector-base junction of the input PNP transistor becoming forward biased and thereby acting as input diodes clamps. In addition to this diode action, there is also NPN parasitic action on the IC chip. this transistor action can cause the output voltages of the Op-amps to go to the V_{CC} voltage level (or to ground for a large overdrive) for the time duration than an input is driven negative.
   This is not destructive and normal output will set up again for input voltage higher than -0.3V.

INPUT BIAS CURRENT
versus AMBIENT TEMPERATURE

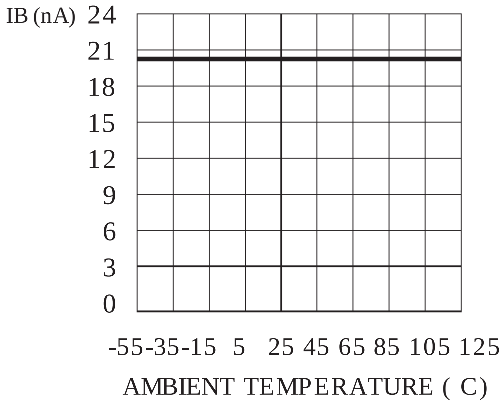

CURRENT LIMITING (Note 8)

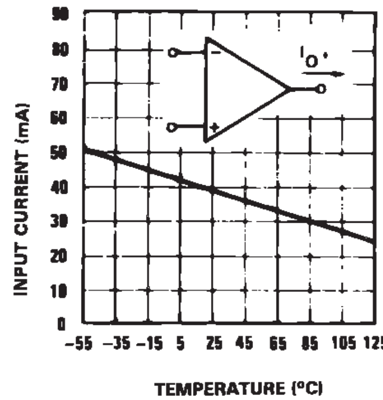

INPUT VOLTAGE RANGE

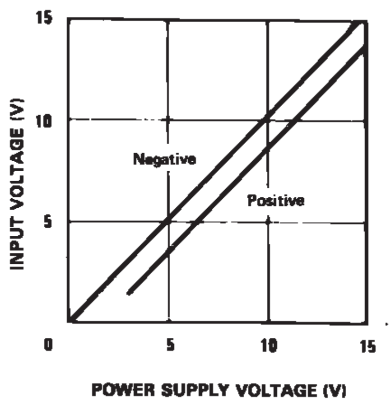

SUPPLY CURRENT

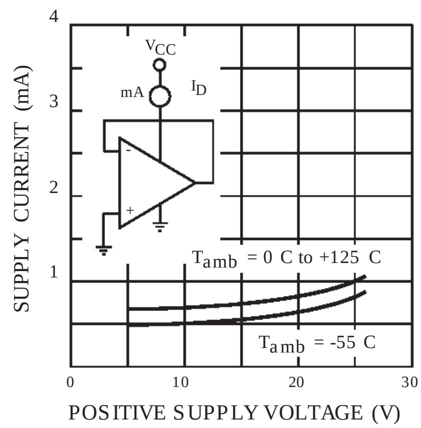

GAIN BANDWIDTH PRODUCT

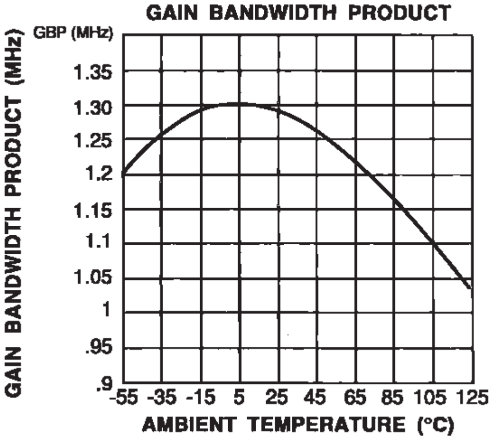

COMMON-MODE REJECTION RATIO

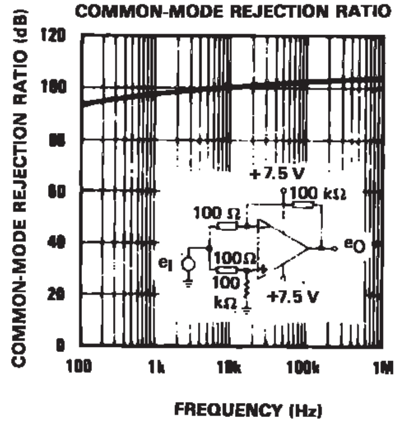

OPEN LOOP FREQUENCY RESPONSE

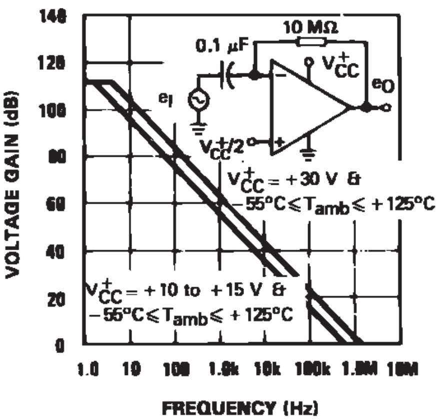

LARGE SIGNAL FREQUENCY RESPONSE

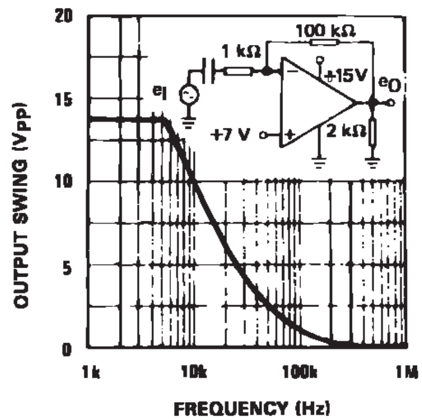

VOLTAGE FOLLOWER PULSE RESPONSE

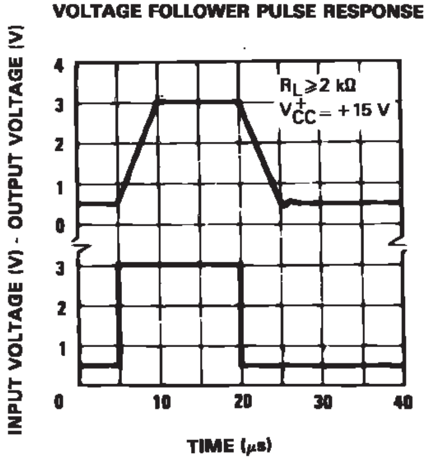

OUTPUT CHARACTERISTICS (CURRENT SINKING)

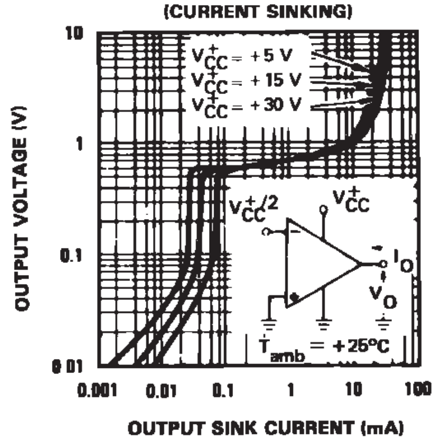

VOLTAGE FOLLOWER PULSE RESPONSE (SMALL SIGNAL)

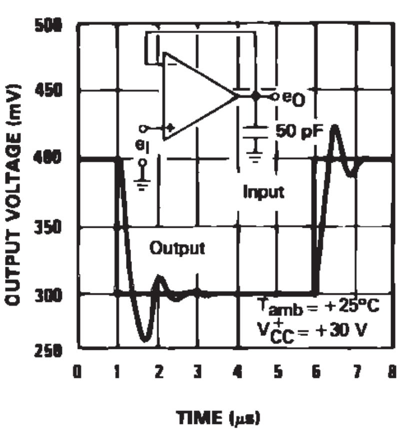

OUTPUT CHARACTERISTICS (CURRENT SOURCING)

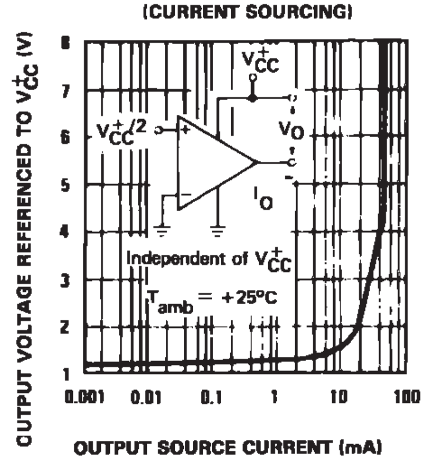

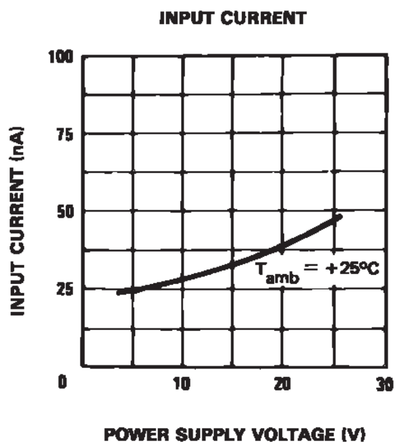

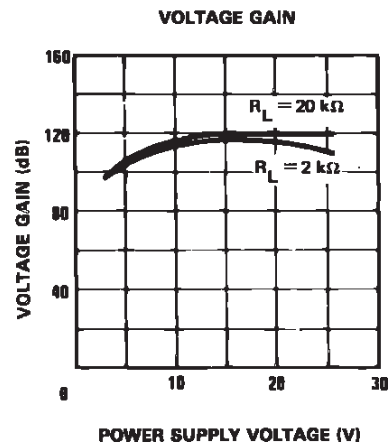

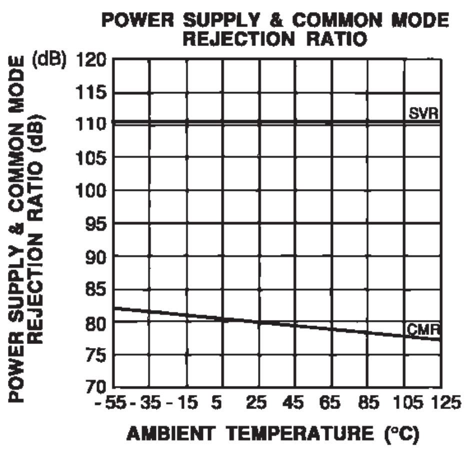

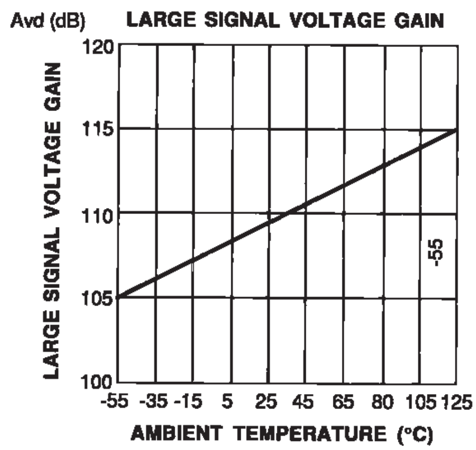

TYPICAL SINGLE - SUPPLY APPLICATIONS

AC COUPLED INVERTING AMPLIFIER

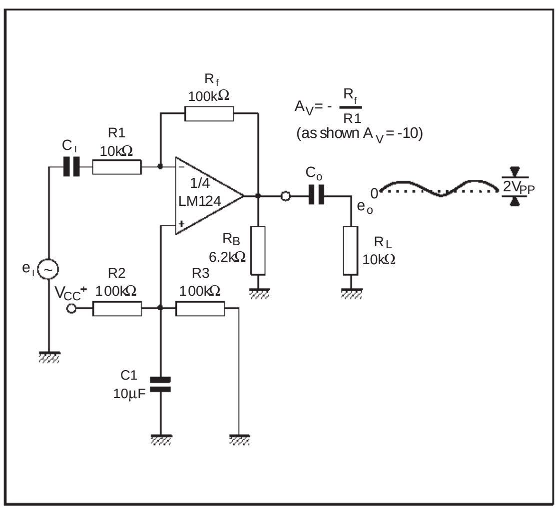

AC COUPLED NON-INVERTING AMPLIFIER

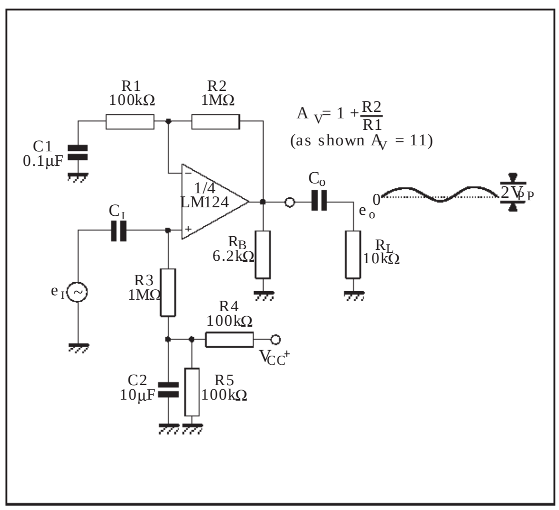

TYPICAL SINGLE - SUPPLY APPLICATIONS

NON-INVERTING DC GAIN

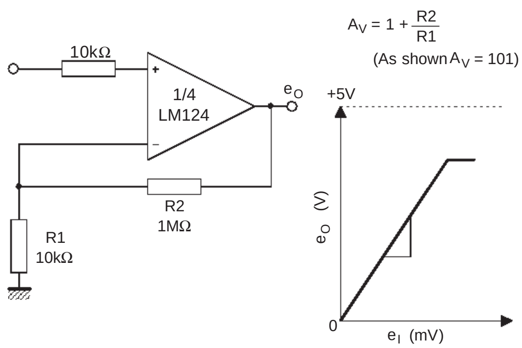

DC SUMMING AMPLIFIER

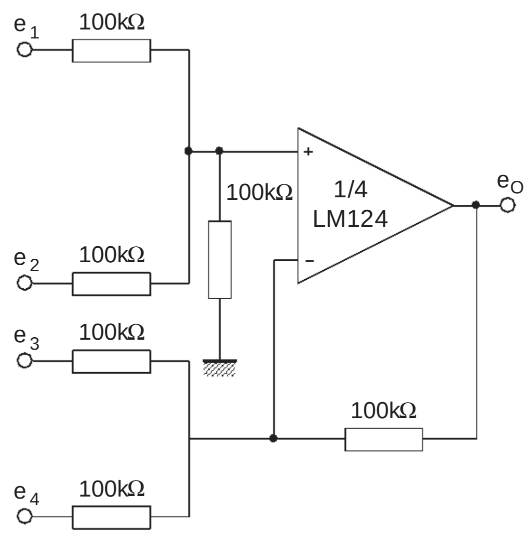

$e_o = e_1 + e_2 - e_3 - e_4$
where $(e_1 + e_2) \geq (e_3 + e_4)$
to keep $e_o \geq 0V$

HIGH INPUT Z ADJUSTABLE GAIN DC INSTRUMENTATION AMPLIFIER

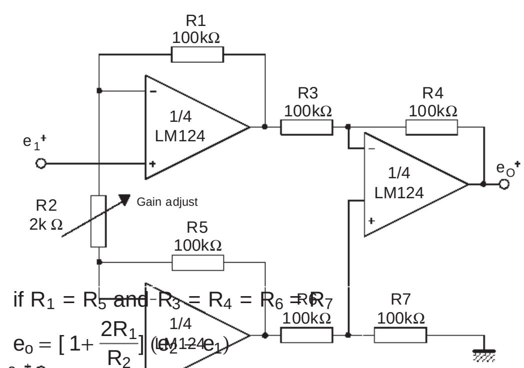

if $R_1 = R_5$ and $R_3 = R_4 = R_6 = R_7$

$e_o = [1 + \frac{2R_1}{R_2}] (e_2 - e_1)$

As shown $e_o = 101 (e_2 - e_1)$.

LOW DRIFT PEAK DETECTOR

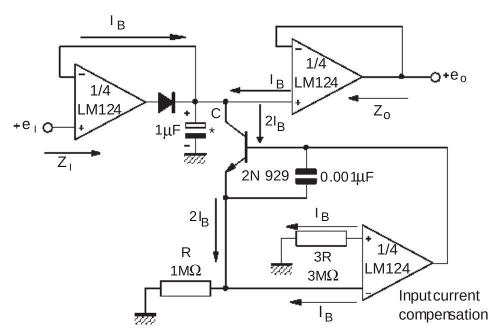

* Polycarbonate or polyethylene

USING SYMMETRICAL AMPLIFIERS TO REDUCE INPUT CURRENT (GENERAL CONCEPT)

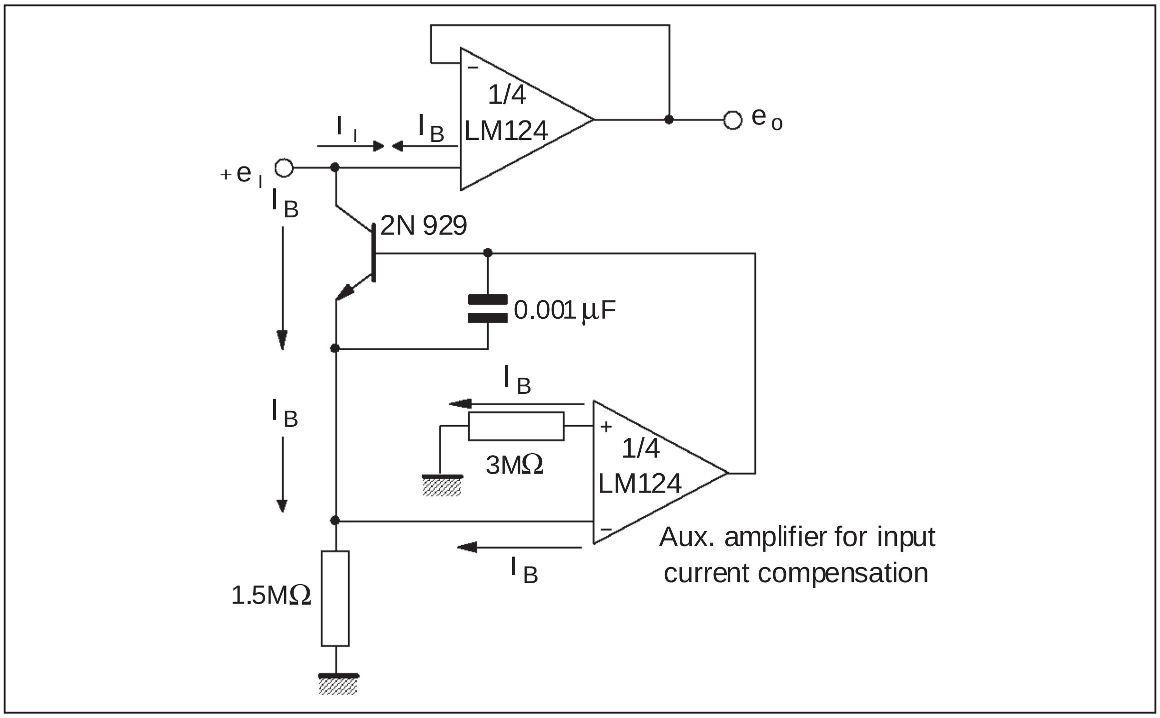

TYPICAL SINGLE - SUPPLY APPLICATIONS

ACTIVER BANDPASS FILTER

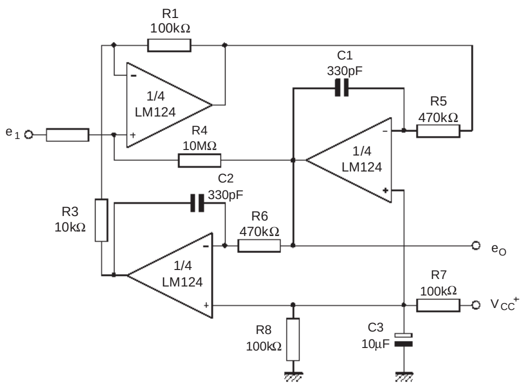

F_O = 1kHz

Q = 50

A_V = 100 (40dB)

HIGH INPUT Z, DC DIFFERENTIAL AMPLIFIER

For $\frac{R_1}{R_2} = \frac{R_4}{R_3}$

(CMRR depends on this resistor ratio match)

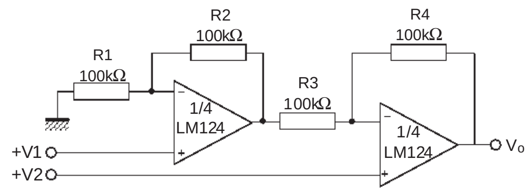

$e_o\ (1 + \frac{R_4}{R_3})\ (e_2 - e_1)$

As shown $e_o = (e_2 - e_1)$

VOLTAGE GAIN AND PHASE vs FREQUENCY

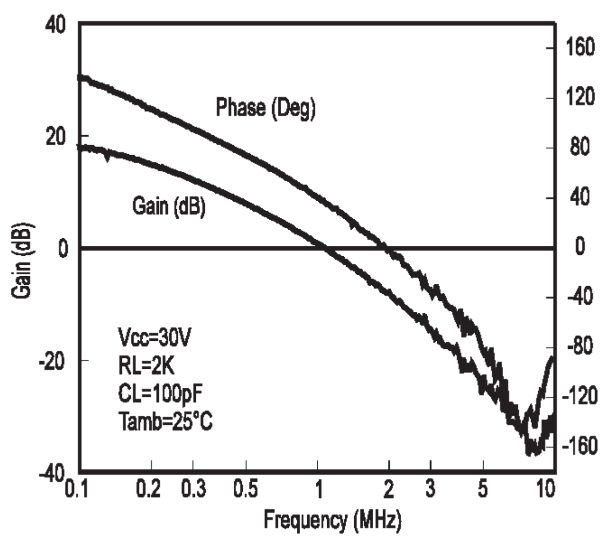

- LARGE VOLTAGE GAIN : 100dB
- VERY LOW SUPPLY CURRENT/AMPLI : 375µA
- LOW INPUT BIAS CURRENT : 20nA
- LOW INPUT OFFSET VOLTAGE : 2mV
- LOW INPUT OFFSET CURRENT : 2nA
- WIDE POWER SUPPLY RANGE :
  SINGLE SUPPLY : +3V to +30V
  DUAL SUPPLIES : ±1.5V to ±15V

Applies to : LM124-LM224-LM324

```
** Standard Linear Ics Macromodels, 1993.
** CONNECTIONS :
* 1 INVERTING INPUT
* 2 NON-INVERTING INPUT
* 3 OUTPUT
* 4 POSITIVE POWER SUPPLY
* 5 NEGATIVE POWER SUPPLY

.SUBCKT LM124 1 3 2 4 5 (analog)
**********************************************************
.MODEL MDTH D IS=1E-8 KF=3.104131E-15
CJO=10F
* INPUT STAGE
CIP 2 5 1.000000E-12
CIN 1 5 1.000000E-12
EIP 10 5 2 5 1
EIN 16 5 1 5 1
RIP 10 11 2.600000E+01
RIN 15 16 2.600000E+01
RIS 11 15 2.003862E+02
DIP 11 12 MDTH 400E-12
DIN 15 14 MDTH 400E-12
VOFP 12 13 DC 0
VOFN 13 14 DC 0
IPOL 13 5 1.000000E-05
CPS 11 15 3.783376E-09
DINN 17 13 MDTH 400E-12
VIN 17 5 0.000000e+00
DINR 15 18 MDTH 400E-12
VIP 4 18 2.000000E+00
FCP 4 5 VOFP 3.400000E+01
FCN 5 4 VOFN 3.400000E+01
FIBP 2 5 VOFN 2.000000E-03
FIBN 5 1 VOFP 2.000000E-03
* AMPLIFYING STAGE
FIP 5 19 VOFP 3.600000E+02
FIN 5 19 VOFN 3.600000E+02
RG1 19 5 3.652997E+06
RG2 19 4 3.652997E+06
CC 19 5 6.000000E-09
DOPM 19 22 MDTH 400E-12
DONM 21 19 MDTH 400E-12
HOPM 22 28 VOUT 7.500000E+03
VIPM 28 4 1.500000E+02
HONM 21 27 VOUT 7.500000E+03
VINM 5 27 1.500000E+02
EOUT 26 23 19 5 1
VOUT 23 5 0
ROUT 26 3 20
COUT 3 5 1.000000E-12
DOP 19 25 MDTH 400E-12
VOP 4 25 2.242230E+00
DON 24 19 MDTH 400E-12
VON 24 5 7.922301E-01
.ENDS
```

ELECTRICAL CHARACTERISTICS

$V_{CC}^+ = +5V$, $V_{CC}^- = 0V$, $T_{amb} = 25^oC$ (unless otherwise specified)

Symbol	Conditions	Value	Unit
V_{io}		0	mV
A_{vd}	$R_L = 2k\Omega$	100	V/mV
I_{CC}	No load, per operator	350	µA
V_{icm}		-15 to +13.5	V
V_{OH}	$R_L = 2k\Omega$ ($V_{CC}^+ = 15V$)	+13.5	V
V_{OL}	RL = 10kΩ	5	mV
I_{OS}	$V_O = +2V$, $V_{CC} = +15V$	+40	mA
GBP	$R_L = 2k\Omega$, $C_L = 100pF$	1.3	MHz
SR	$R_L = 2k\Omega$, $C_L = 100pF$	0.4	V/µs

PACKAGE MECHANICAL DATA

14 PINS - PLASTIC DIP

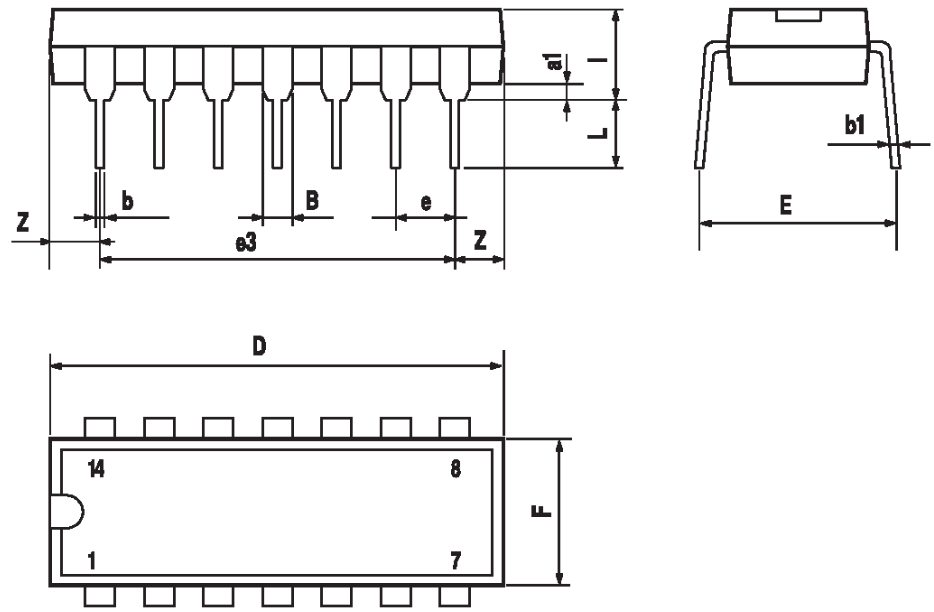

Dimensions	Millimeters			Inches		
	Min.	Typ.	Max.	Min.	Typ.	Max.
a1	0.51			0.020		
B	1.39		1.65	0.055		0.065
b		0.5			0.020	
b1		0.25			0.010	
D			20			0.787
E		8.5			0.335	
e		2.54			0.100	
e3		15.24			0.600	
F			7.1			0.280
i			5.1			0.201
L		3.3			0.130	
Z	1.27		2.54	0.050		0.100

DIP14.TBL

PACKAGE MECHANICAL DATA

14 PINS - PLASTIC MICROPACKAGE (SO)

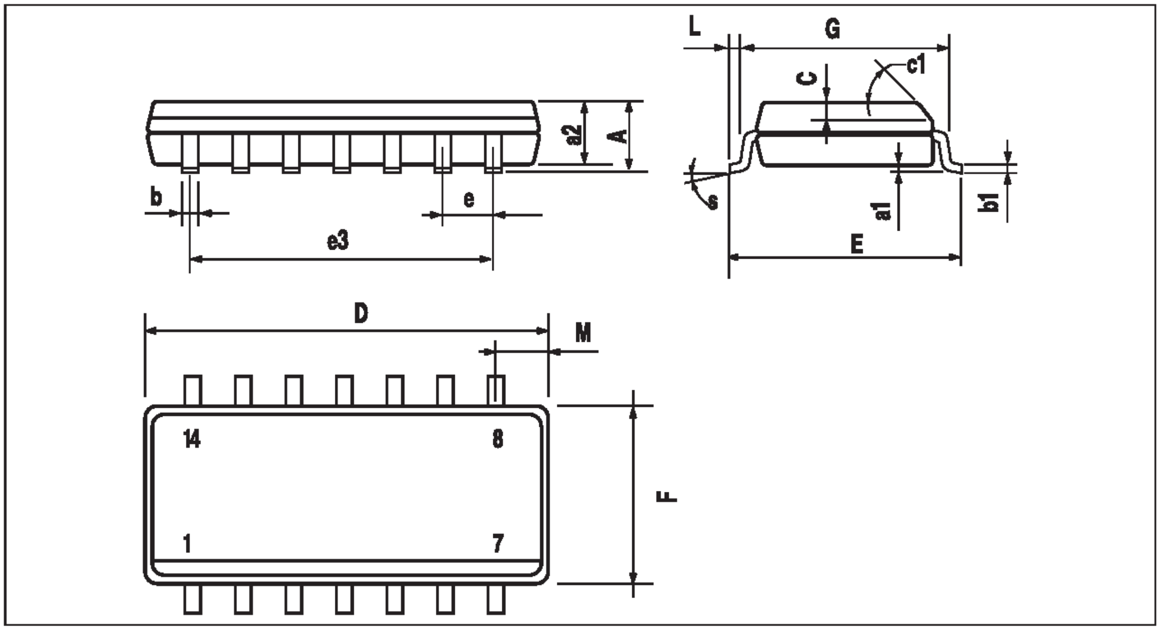

Dimensions	Millimeters			Inches		
	Min.	Typ.	Max.	Min.	Typ.	Max.
A			1.75			0.069
a1	0.1		0.2	0.004		0.008
a2			1.6			0.063
b	0.35		0.46	0.014		0.018
b1	0.19		0.25	0.007		0.010
C		0.5			0.020	
c1	45^o (typ.)					
D	8.55		8.75	0.336		0.334
E	5.8		6.2	0.228		0.244
e		1.27			0.050	
e3		7.62			0.300	
F	3.8		4.0	0.150		0.157
G	4.6		5.3	0.181		0.208
L	0.5		1.27	0.020		0.050
M			0.68			0.027
S	8^o (max.)					

SO14.TBL

PACKAGE MECHANICAL DATA
14 PINS - THIN SHRINK SMALL OUTLINE PACKAGE

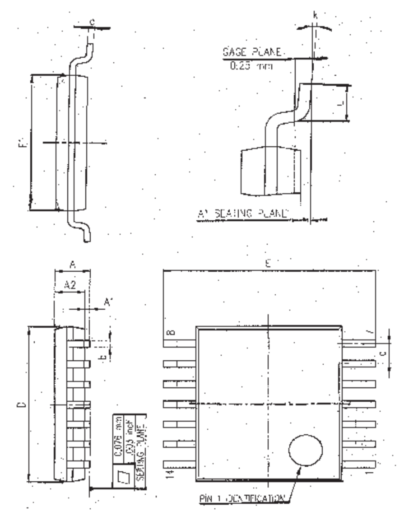

Dim.	Millimeters			Inches		
	Min.	Typ.	Max.	Min.	Typ.	Max.
A			1.20			0.05
A1	0.05		0.15	0.01		0.006
A2	0.80	1.00	1.05	0.031	0.039	0.041
b	0.19		0.30	0.007		0.15
c	0.09		0.20	0.003		0.012
D	4.90	5.00	5.10	0.192	0.196	0.20
E		6.40			0.252	
E1	4.30	4.40	4.50	0.169	0.173	0.177
e		0.65			0.025	
k	0^o		8^o	0^o		8^o
l	0.50	0.60	0.75	0.09	0.0236	0.030

BIBLIOGRAPHY

[1] K. K. Sen and M. L. Sen, *Introduction to FACTS Controllers: Theory, Modeling, and Applications (IEEE Press Series on Power Engineering)*, 1st ed. Wiley-IEEE Press, 9 2009. [Online]. Available: http://amazon.com/o/ASIN/0470478756/

[2] P. K. Steimer, "Enabled by high power electronics - energy efficiency, renewables and smart grids," in *Proc. Int. Power Electronics Conf. (IPEC)*, 2010, pp. 11–15.

[3] R.-J. Wai, C.-Y. Lin, R.-Y. Duan, and Y.-R. Chang, "High-efficiency power conversion system for kilowatt-level stand-alone generation unit with low input voltage," vol. 55, no. 10, pp. 3702–3714, 2008.

[4] R. Gonzalez, J. Lopez, P. Sanchis, and L. Marroyo, "Transformerless inverter for single-phase photovoltaic systems," vol. 22, no. 2, pp. 693–697, 2007.

[5] R.-J. Wai and R.-Y. Duan, "High-efficiency power conversion for low power fuel cell generation system," vol. 20, no. 4, pp. 847–856, 2005.

[6] R.-Y. Duan, C.-T. Chang, and T.-L. Su, "A novel current-source sine wave voltage inverter with soft-switching and low-switching stress," in *Proc. 37th IEEE Power Electronics Specialists Conf. PESC '06*, 2006, pp. 1–6.

[7] K. Ogura, T. Nishida, E. Hiraki, M. Nakaoka, and S. Nagai, "Time-sharing boost chopper cascaded dual mode single-phase sinewave inverter for solar photovoltaic power generation system," in *Proc. IEEE 35th Annual Power Electronics Specialists Conf. PESC 04*, vol. 6, 2004, pp. 4763–4767.

[8] J. Li, J. Li, and S. Ding, "Research on a novel method for improving inverter output waveforms," in *Proc. 5th IEEE Conf. Industrial Electronics and Applications (ICIEA)*, 2010, pp. 1194–1197.

[9] M. J. Meco-Gutierrez, F. Perez-Hidalgo, F. Vargas-Merino, and J. R. Heredia-Larrubia, "Pulse width modulation technique with harmonic injection and frequency modulated carrier: formulation and application to an induction motor," *IET Electric Power Applications*, vol. 1, no. 5, pp. 714–726, 2007.

[10] Q. Zheng, Q. Wang, R. Hao, and L. Chang, "A novel three-phase pulse width modulation (pwm) technique based on co-related references [invertor applications]," in *Proc. Third Int. Telecommunications Energy Special Conf. TELESCON 2000*, 2000, pp. 255–258.

[11] M. Nagao, Y. Fujisawa, and K. Harada, "Efficiency improvement by frequency modulation depending on load current for inductor commutation soft-switched pwm inverter," in *Proc. IEEE 35th Annual Power Electronics Specialists Conf. PESC 04*, vol. 5, 2004, pp. 3939–3945.

[12] M. J. Meco-Gutierrez, F. Perez-Hidalgo, F. Vargas-Merino, and J. R. Heredia-Larrubia, "A new pwm technique frequency regulated carrier for induction motors supply," vol. 53, no. 5, pp. 1750–1754, 2006.

[13] M. J. Meco-Gutierrez, A. Ruiz Gonzalez, F. Vargas-Merino, F. Perez Hidalgo, and J. R. Heredia-Larrubia, "Low heating losses by harmonic injection pwm with a frequency modulated triangular carrier," in *Proc. Int. Symp. Power Electronics, Electrical Drives, Automation and Motion SPEEDAM 2008*, 2008, pp. 1398–1401.

[14] A. Ruiz-Gonzalez, M. J. Meco-Gutierrez, F. Perez-Hidalgo, F. Vargas-Merino, and J. R. Heredia-Larrubia, "Reducing acoustic noise radiated by inverter-fed induction motors controlled by a new pwm strategy," vol. 57, no. 1, pp. 228–236, 2010.

[15] F. Vargas-Merino, M. J. Meco-Gutierrez, J. R. Heredia-Larrubia, and A. Ruiz-Gonzalez, "Slope modulation strategy for generated pwm," in *Proc. IEEE Int. Symp. Industrial Electronics ISIE 2008*, 2008, pp. 403–405.

[16] ——, "Low switching pwm strategy using a carrier wave regulated by the slope of a trapezoidal modulator wave," vol. 56, no. 6, pp. 2270–2274, 2009.

[17] A. Ruiz-Gonzalez, F. Vargas-Merino, F. Perez-Hidalgo, M. J. Meco-Gutierrez, and J. R. Heredia-Larrubia, "Low switching pwm strategy to reduce acoustic noise radiated by inverter-fed induction motors," in *Proc. IEEE Int Industrial Electronics (ISIE) Symp*, 2010, pp. 1353–1358.

[18] A. Ruiz-Gonzaa andlez, M. Meco-Gutierrez, F. Vargas-Merino, F. Perez-Hidalgo, and J. Ramoo andn Heredia Larrubia, "Shaping the hipwm-fmtc strategy to reduce acoustic noise radiated by inverter-fed induction motors," in *Electrical Machines (ICEM), 2010 XIX International Conference on*, sept. 2010, pp. 1 –6.

[19] D. Quek and S. Yuvarajan, "A novel pwm scheme for harmonic reduction in power converters," in *Proc. Int Power Electronics and Drive Systems Conf*, 1995, pp. 560–564.

[20] R. Nandhakumar and S. Jeevananthan, "Inverted sine carrier pulse width modulation for fundamental fortification in dc-ac converters," in *Proc. 7th Int. Conf. Power Electronics and Drive Systems PEDS '07*, 2007, pp. 1028–1034.

[21] P. V. S. Jeevananthan, S. Dananjayan, "A novel modified carrier pwm switching strategy for single-phase full-bridge inverter," *IRANIAN JOURNAL OF ELECTRICAL AND COMPUTER ENGINEERING*, vol. VOL 4; NUMB 2, pp. pages 101–108, 2005. [Online]. Available: http://www.sid.ir/en/VEWSSID/J_pdf/89020050202.pdf

[22] P. Palanivel and S. S. Dash, "A fpga based variable switching frequency multi-carrier pulse width modulation for three phase multilevel inverter," in *Proc. Int. Conf. Control, Automation, Communication and Energy Conservation INCACEC 2009*, 2009, pp. 1–4.

[23] ——, "Analysis of thd and output voltage performance for cascaded multilevel inverter using carrier pulse width modulation techniques," *IET Power Electronics*, vol. 4, no. 8, pp. 951–958, 2011.

[24] ——, "Multicarrier pulse width modulation methods based three phase cascaded multilevel inverter including over modulation and low modulation indices," in *Proc. TENCON 2009 - 2009 IEEE Region 10 Conf*, 2009, pp. 1–6.

[25] I. E. Agency, "World energy outlook 2011," Tech. Rep., 2011. [Online]. Available: http://www.iea.org/weo/docs/weo2011/key_graphs.pdf

[26] G. F. Reed, B. M. Grainger, H. Bassi, E. Taylor, Z.-H. Mao, and A. K. Jones, "Analysis of high capacity power electronic technologies for integration of green energy management," in *Proc. IEEE PES Transmission and Distribution Conf. and Exposition*, 2010, pp. 1–10.

[27] N. Mohan, "Teaching utility applications of power electronics in the first course on power systems," in *Proc. IEEE Power Engineering Society General Meeting*, vol. 1, 2003, pp. 130–132.

[28] J. Arai, K. Iba, T. Funabashi, Y. Nakanishi, K. Koyanagi, and R. Yokoyama, "Power electronics and its applications to renewable energy in japan," vol. 8, no. 3, pp. 52–66, 2008.

[29] E. Muljadi, C. P. Butterfield, J. Chacon, and H. Romanowitz, "Power quality aspects in a wind power plant," in *Proc. IEEE Power Engineering Society General Meeting*, 2006.

[30] S. K. Chaudhary, R. Teodorescu, and P. Rodriguez, "Wind farm grid integration using vsc based hvdc transmission - an overview," in *Proc. IEEE Energy 2030 Conf. ENERGY 2008*, 2008, pp. 1–7.

[31] M. Rashid, *Power Electronics Handbook: Devices, Circuits, and Applications*, ser. Academic Press. Elsevier, 2010. [Online]. Available: http://books.google.com/books?id=eS1z95mzi28C

[32] J. Morneau, C. Abbey, and G. Joos, "Effect of low voltage ride through technologies on wind farm," in *Proc. IEEE Canada Electrical Power Conf. EPC 2007*, 2007, pp. 56–61.

[33] B. K. Bose, “Energy, environment, and advances in power electronics,” vol. 15, no. 4, pp. 688–701, 2000.

[34] F. C. Lee, “The state-of-the-art power electronics technologies and future trends,” in *Proc. IEEE Power Engineering Society Summer Meeting*, vol. 2, 2000, pp. 1229–1232.

[35] V. K. Sood, *HVDC and FACTS controllers, application of static converters in power systems*. Boston : Kluwer Academic, 2004, 2004.

[36] E. P. R. I. Staff, *HVDC Handbook*. Electric Power Research Institute, 1994. [Online]. Available: http://books.google.com/books?id=CNrCAAAACAAJ

[37] W. Zhang and W. Chen, “Research on voltage-source pwm inverter based on state analysis method,” in *Proc. Int. Conf. Mechatronics and Automation ICMA 2009*, 2009, pp. 2183–2187.

[38] H. Zhou and G. Yang, “Control of dfig-based wind farms with hybrid hvdc connection,” in *Proc. IEEE 6th Int. Power Electronics and Motion Control Conf. IPEMC ’09*, 2009, pp. 1085–1091.

[39] J. Setreus and L. Bertling, “Introduction to hvdc technology for reliable electrical power systems,” in *Proc. 10th Int. Conf. Probabilistic Methods Applied to Power Systems PMAPS ’08*, 2008, pp. 1–8.

[40] B. Wu, *High-Power Converters And AC Drives*. Wiley, 2006. [Online]. Available: http://books.google.com/books?id=X1b1laKEtugC

[41] M. A. Boost and P. D. Ziogas, “State-of-the-art carrier pwm techniques: a critical evaluation,” vol. 24, no. 2, pp. 271–280, 1988.

[42] S. Rahmani, K. Al-Haddad, and H. Y. Kanaan, “Experimental design and simulation of a modified pwm with an indirect current control technique applied to a single-phase shunt active power filter,” in *Proc. IEEE Int. Symp. Industrial Electronics ISIE 2005*, vol. 2, 2005, pp. 519–524.

[43] M. F. N. Tajuddin, N. H. Ghazali, T. C. Siong, and N. Ghazali, “Modelling and simulation of modified unipolar pwm scheme on a single phase dc-ac converter using psim,” in *Proc. IEEE Student Conf. Research and Development (SCOReD)*, 2009, pp. 328–331.

[44] H. Rashid, *Power electronics: circuits, devices, and applications*. Pearson/Prentice Hall, 2004. [Online]. Available: http://books.google.com/books?id=YH0eAQAAIAAJ

[45] D. J. Tooth, N. McNeill, S. J. Finney, and B. W. Williams, “A new soft-switching technique using a modified pwm scheme requiring no extra hardware,” vol. 16, no. 5, pp. 686–693, 2001.

[46] G. Buja and G. Indri, "Improvement of pulse width modulation techniques," *Electrical Engineering (Archiv fur Elektrotechnik)*, vol. Volume 57, Number 5, pp. Pages 281–289, 1975.

[47] N. G. Hingorani and L. Gyugyi, *Understanding FACTS: Concepts and Technology of Flexible AC Transmission Systems*, 1st ed. Wiley-IEEE Press, 12 1999. [Online]. Available: http://amazon.com/o/ASIN/0780334558/

[48] G. Reed, J. Paserba, T. Croasdaile, M. Takeda, Y. Hamasaki, T. Aritsuka, N. Morishima, S. Jochi, I. Iyoda, M. Nambu *et al.*, "The velco statcom based transmission system project," in *Power Engineering Society Winter Meeting, 2001. IEEE*, vol. 3. IEEE, 2001, pp. 1109–1114.

[49] G. Reed, J. Paserba, T. Croasdaile, M. Takeda, N. Morishima, Y. Hamasaki, L. Thomas, and W. Allard, "Statcom application at velco essex substation," in *Transmission and Distribution Conference and Exposition, 2001 IEEE/PES*, vol. 2. IEEE, 2001, pp. 1133–1138.

[50] *IEEE Recommended Practices and Requirements for Harmonic Control in Electrical Power Systems*, IEEE Std.